博士論文

Analytical studies on reaction mechanisms of hard carbon electrode as a sodium-ion host

（ナトリウムイオンホストとしてのハードカーボン電極の反応機構解析）

森川 裕介 (Yusuke Morikawa)

Department of Chemical System Engineering

Graduate School of Engineering

The University of Tokyo

Table of contents

1 General introduction

1.1 Overview of rechargeable batteries

Since the Industrial Revolution, the energy consumed by mankind has been increasing, and now reaches 138 billion tons/year in terms of oil.[1] With the economic development of developing countries, the increase has accelerated, and energy consumption has doubled in the last 30 years.[1] About 90% of primary energy relies on energy resources such as coal, oil, and natural gas, all of which can be depleted in the next 50–100 years. Based on this situation, we must move away from dependence on fossil fuels as soon as possible to achieve a sustainable society.

An essential part of building a sustainable society is the efficient use of renewable energy and resources. However, renewable energy represented by sunlight and wind power has large output fluctuations due to environmental and weather effects. Therefore, to efficiently use natural energy, an energy storage system for leveling electric power is required. Secondary batteries such as lithium ion batteries (LIBs) are expected to play this role. In 2019, the Nobel Prize for Chemistry was awarded to John B. Goodenough, M. Stanley Whittingham, and Akira Yoshino for their contribution to the development of LIBs. As the Nobel Foundation states, LIBs "can also store significant amounts of energy from solar and wind power, making possible a fossil fuel-free society". So, the reasons for the award is that LIBs can be a solution to environmental problems.[2] However, since the current LIBs have problems of cost and resource, various energy storage materials are being studied intensively to solve these problems.[3–9]

1.2 Anode materials for lithium ion batteries

The first commercial LIB was released by Sony in 1991. The anode material was a carbon material called hard carbon and the cathode material was $LiCoO_2$.[10] A schematic illustration of an LIB is shown in **Figure 1.1**. Basically, the cathode material contains lithium in the initial state, and the

anode material is a substance that can store lithium. Lithium ions move from the cathode to the anode through the electrolyte during charging and move in the opposite way during discharging. During the first charge, solvents and salts of the electrolyte are reduced and decomposed to form a film called solid electrolyte interphase (SEI) on the anode surface.[11–13] By forming the SEI, further decomposition of the electrolyte is suppressed, and stable charging/discharging becomes possible.

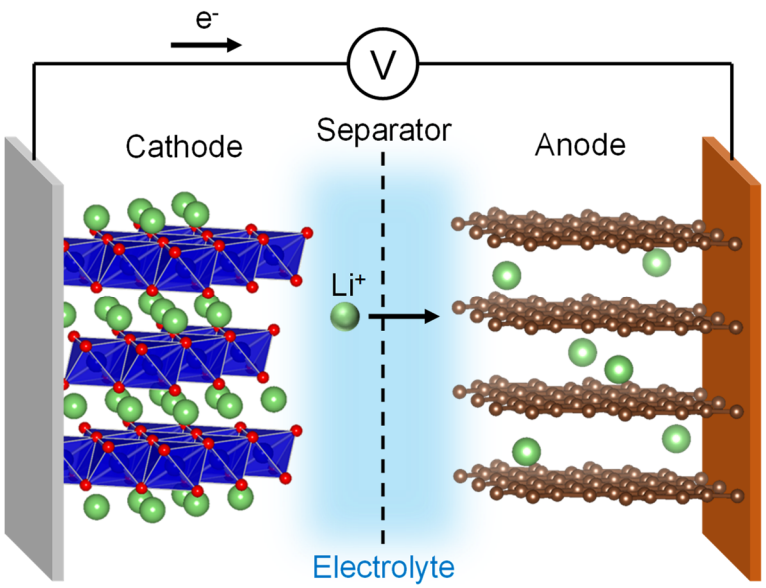

Figure 1.1 Schematic illustration of an LIB.

Figure 1.2 shows a comparison of reversible capacity and operating voltage ranges of the typical anode materials of LIBs. A material with a low redox potential and a large capacity can be said to be a good anode material that can achieve a high energy density. Although Lithium metal (shown in yellow) is considered to be an ideal material in terms of energy density, at present, rechargeable batteries using Li metal are not commercially available for the following two reasons:

(i) Lithium metal grows in a needle shape ("dendrite") when charging and discharging are repeated.

(ii) Coulombic efficiency and cycle performance are not good.

To perform stable charge and discharge, it is necessary to plate lithium metal uniformly on the

current collector surface. When deposition and dissolution occurs unevenly and the surface becomes rough, Li dendrite grows and breaks through the separator and accidents such as explosions can occur due to short circuit. It has been reported that the formation of SEI containing fluorine can suppress dendrite growth[14–16], but this has not yet reached a practical level of safety.

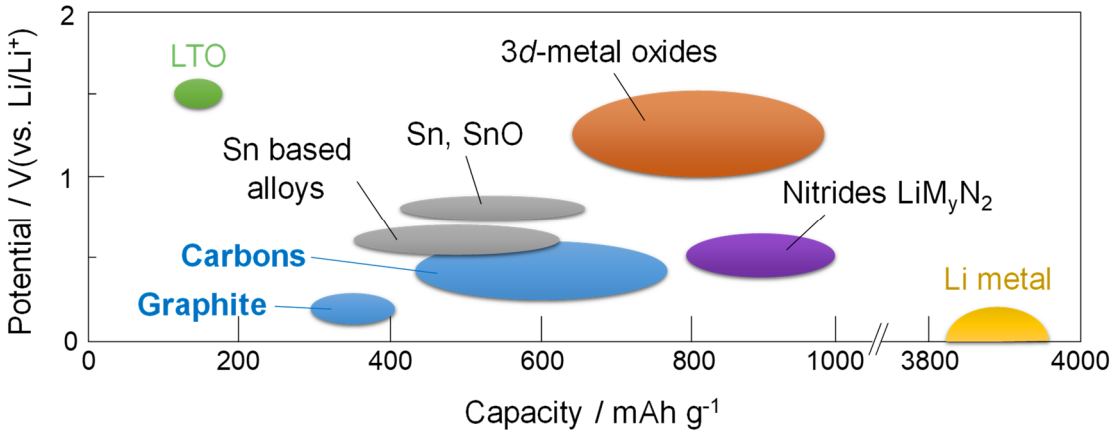

Figure 1.2 Average potential versus capacity for selected anode materials of LIBs.[3]

Sn and SnO (shown in gray) store Li by an alloying reaction. The electrochemical reaction can be described as follows:

$$M + xLi^+ + xe^- \leftrightarrows Li_xM \text{ (M: metal)}$$

These materials have a relatively large reversible capacity, but their volume changes greatly with the insertion and removal of lithium, so that their capacity rapidly decreases due to a loss of electrical contacts between particles.[17,18] Researches have been conducted to suppress degradation by making the active material nano-sized or coating it with a carbon material, but examples of practical use are still limited.

Carbon materials represented by graphite[19–21] have a relatively low reaction voltage and a capacity over 300 mAh g^{-1}. Since these are excellent in energy density and cycle stability, they are currently most widely used as negative electrode materials for LIBs. Carbon materials are roughly

classified into graphite, soft carbon, and hard carbon, depending on the microstructure. The classification and its Li storage mechanisms are described in section 1.3.

$Li_4Ti_5O_{12}$ (LTO) is a typical negative electrode material that has been put to practical use (*e.g.*, SiCB™, TOSHIBA). One of the causes of battery capacity fade is the change in volume of the active material during charge/discharge, but LTO has negligible change in volume (0.2%)[22] and has excellent cycle characteristics.[23,24]

1.3 Classification of carbon materials

Carbon materials have various structures such as amorphous carbon, graphite, diamond, vapor grown carbon fiber (VGCF)[25], carbon nanotubes (CNTs)[26,27], and graphene[28]. As described in section 1.2, graphite is used as the anode material for LIBs, but many other carbon materials can store lithium. For example, VGCF is a material used in the prototype of an LIB created by Yoshino *et al*.[29] In addition, a discharge capacity of 450–1000 mAh g^{-1} and 490–577 mAh g^{-1} has been reported for single-walled carbon nanotubes (SWNTs)[30] and multi-walled carbon nanotubes (MWNTs) [31–33], respectively. However, since nanocarbon has a high surface area and many reaction sites, it is difficult to avoid high reactivity with the electrolyte (basically the initial Coulomb efficiency is less than 50%). For practical application, it is necessary to reduce surface defects and devise surface modification. The following describes the hard carbon that is the subject material of this thesis and two similar carbon materials (graphite and soft carbon).

1.3.1 Graphite

Graphite is a layered material with graphene sheets stacked by van der Waals force as shown in **Figure 1.3** (space group: $P6_3/mmc$). As can be seen from Figure 1.3b and 1.3c, the graphene sheets are stacked and shifted from layer to layer, and the interlayer distance is 3.35 Å . Each layer is shifted

so that the atoms in layer A are above or below the center of the hexagon in layer B. If the stack is relatively complete, it is called graphite, otherwise it is called soft carbon or hard carbon depending on the degree of alignment.

Since lithium and potassium ions are inserted between the layers electrochemically, graphite can be used as an anode material for LIBs and potassium ion batteries (KIBs). On the other hand, it has been reported that sodium ion is hardly inserted between graphite layers (< 35 mAh g^{-1})[34,35], although it is an alkali metal. When lithium and potassium are maximally inserted into the graphite, they have the composition of LiC_6 and KC_8, respectively. Therefore, the theoretical capacity is 372 mAh g^{-1} for LIBs and 279 mAh g^{-1} for KIBs. Experimentally, a reversible capacity almost equal to the theoretical capacity has been confirmed in LIBs[36], and a reversible capacity of 87.5% of the theoretical capacity has been reported in KIBs.[37]

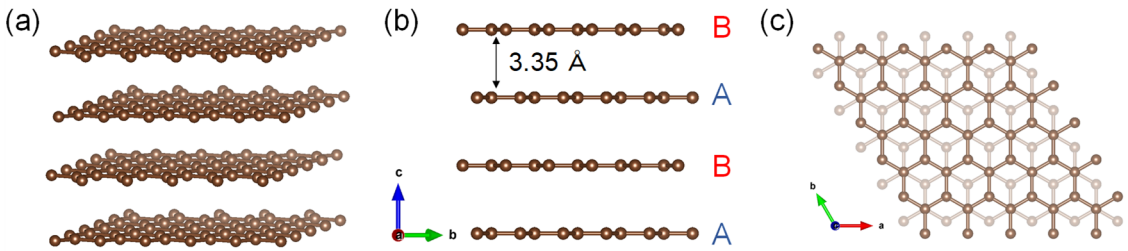

Figure 1.3 The structure of graphite. (b) and (c) are views seen from the a-axis and c-axis directions, respectively.

1.3.2 Soft carbon

The local structure of both soft carbon and hard carbon is the same as that of graphite. Although there is no specific definition that distinguishes the two, they are classified according to the degree of the turbostratic disorder as shown in **Figure 1.4**.

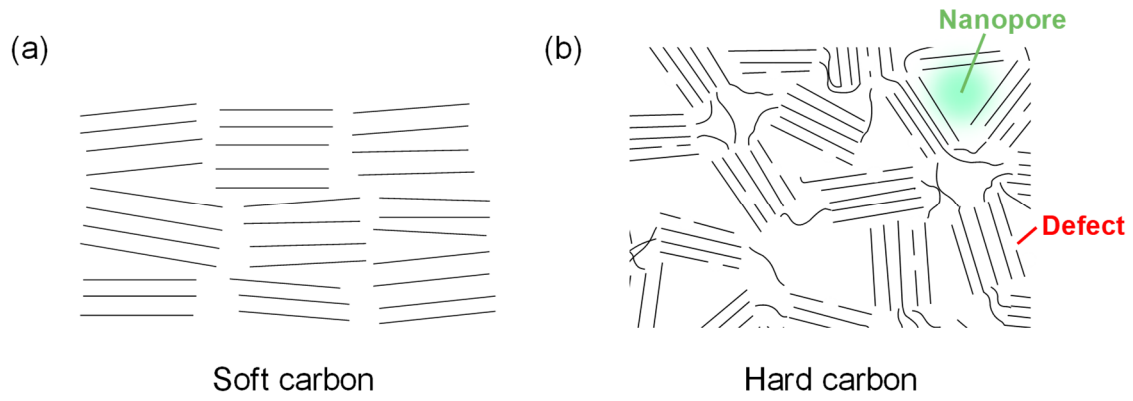

Figure 1.4 Schematic image of (a) soft carbon and (b) hard carbon.[38]

When graphite-like layers are lined up relatively in the same direction, it is called "soft carbon". When soft carbon is heat-treated at a high temperature, graphitization proceeds and it becomes graphite because it is possible to form a continuous layer with slight atomic movement.[38] Soft carbon can occlude lithium, sodium, and potassium ions. In the case of LIBs, the capacity is 150–1000 mAh g^{-1} but the irreversible capacity is large.[39–41]

1.3.3 Hard carbon

In hard carbon, graphite-like layers are randomly arranged and there are many defects and nanopores (Figure 1.4b). Generally, even when heat treatment is performed at high temperature (around 3000 °C), graphitization hardly proceeds and the amorphous structure is maintained.[38] The atomic structure of hard carbon is poorly characterized, but attempts have been made to elucidate it with pair distribution function (PDF) analysis[42] and combined calculation of density functional theory (DFT) and machine learning.[43] As shown in **Figure 1.5**, the graphene sheet includes a 5-membered ring and a 7-membered ring, and seems to be undulating.

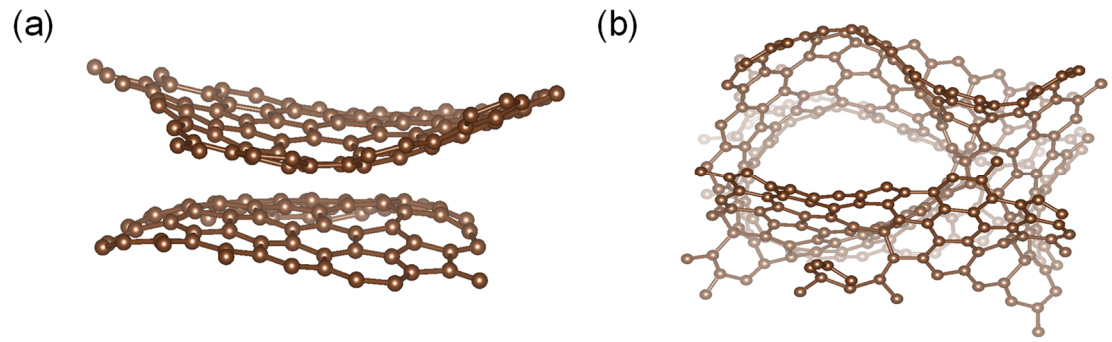

Figure 1.5 Atomic structures of hard carbon obtained by DFT calculation. (a) Layered structure and (b) nanopore structure.[42,43]

As the raw material, thermosetting resins such as phenol resin[44,45] and furan resin, saccharides such as sucrose[46–48] and glucose[49–51], and plant-derived substances such as cotton[39,52] and pollen[53,54] are used. Since hard carbon has good input/output characteristics and can easily monitor the remaining capacity from the voltage, it is partly used in current commercial LIBs.

1.4 Li storage mechanism in carbon materials

1.4.1 Graphite

Figure 1.6(a) shows the charge-discharge graph of the first cycle of graphite. The reaction proceeds at 0.05–0.2 V (vs. Li/Li^+). SEI is formed during the first charge, and this is observed as irreversible capacity Q_{irr}. As can be seen from Figure 1.6(b), three plateaus are observed near 0 V.

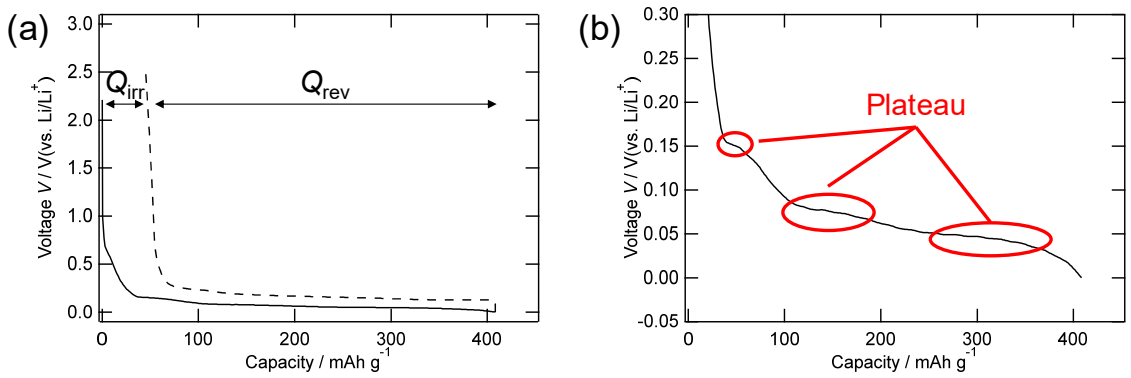

Figure 1.6 Typical charge-discharge profile of graphite|Li half-cell**.** (b) is an enlarged view around 0 V.

Lithium is intercalated between the graphene layers and Li-graphite has four types of stage structures depending on the amount of lithium inserted (**Figure 1.7**(a)). When the number of adjacent graphene layers is *n*, it is expressed as stage-*n*. Dahn *et al*. investigated the relationship between the intercalated amount of lithium and the stage structure (Figure 1.7(b)).[55] The stage-1' appears when the lithium insertion amount *x* is small. Stage-1' is a state in which lithium is randomly inserted into each layer, and since there is no adjacent graphene layer, it corresponds to stage-1 in terms of classification. In the stage 2L, the layer in which lithium is inserted is the same as in stage-2, but the arrangement of lithium atoms in the plane is not ordered. Except for stage 1' and stage 2L, the lithium ions are arranged in order in the plane. At room temperature, the structure changes in stages from stage 4 to stage 1 except when the lithium insertion amount *x* is small. Since the two-phase reaction proceeds except for at the boundary of each stage, the charge-discharge curve has three plateaus.

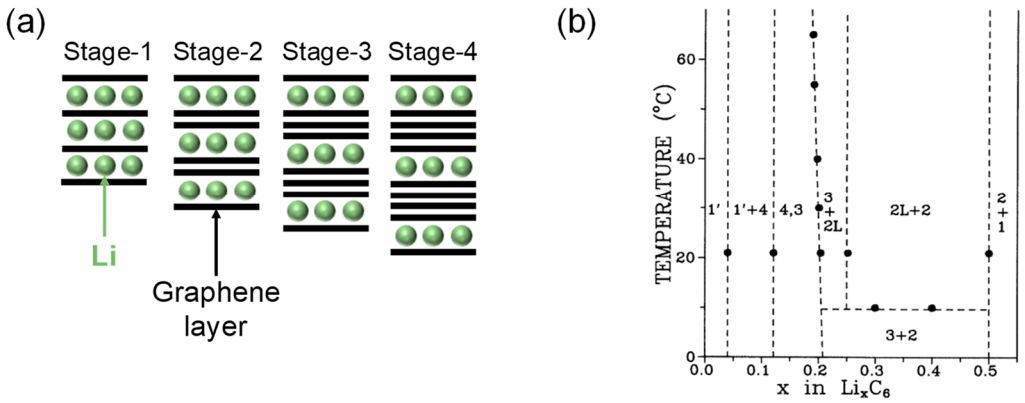

Figure 1.7 (a) Stage structure of Li-graphite and (b) the phase diagram of Li_xC_6 in the range 0 °C < T < 70 °C. Reproduced with permission.[55] Copyright 1991, American Physical Society.

Lithium is intercalated up to 1 atom per 6 carbon atoms and takes a superlattice structure called $\sqrt{3} \times \sqrt{3}$ structure in the plane (Figure 1.8). At this time, the structure of the carbon skeleton changes from AB stacking to AA stacking. Lithium is stored at the center of the hexagonal column composed of the six-membered rings of the upper and lower graphene layers, and is not inserted into the adjacent hexagonal column. When lithium is inserted between layers, the distance between layers increases, which can be confirmed from the X-ray diffraction (XRD) pattern.[56]

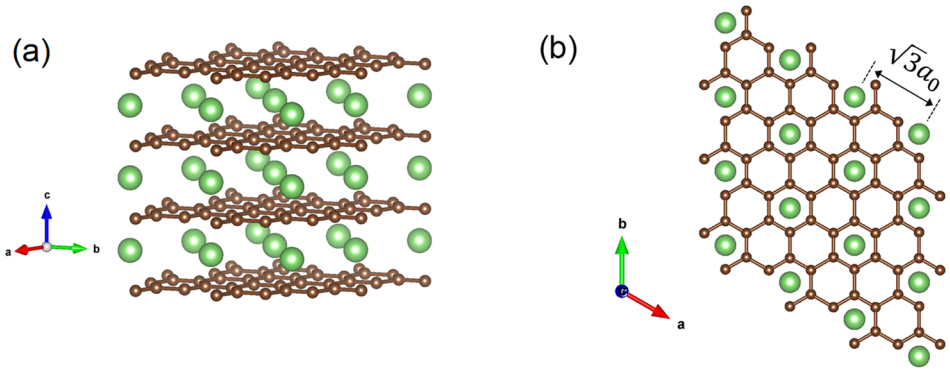

Figure 1.8 Crystal structure of LiC_6. Li atoms and C atoms are shown in green and brown, respectively.

1.4.2 Soft carbon and hard carbon

It has been reported by Dahn *et al*. that the characteristics of soft carbon and hard carbon change drastically depending on the annealing temperature.[39] Figure 1.9 shows the relationship between the heat treatment temperature and reversible capacity of various carbon samples.

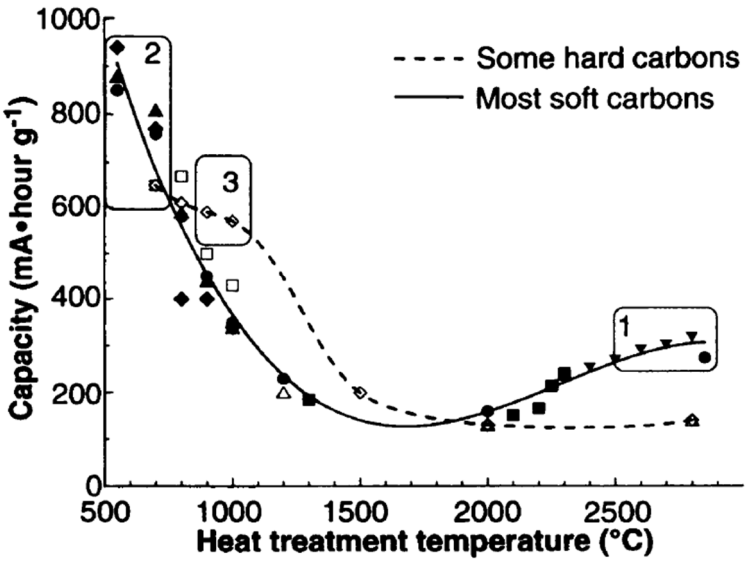

Figure 1.9 Plot of reversible capacity versus heat treatment temperature for various carbon samples. Reproduced with permission.[39] Copyright 1995, The American Association for the Advancement of Science.

In hard carbon, the reversible capacity decreases monotonically with increasing heat treatment temperature. On the other hand, with soft carbon, the capacity decreases monotonously up to 1500 °C, shows a minimum value near 1500–1700 °C, and then increases with heat treatment above 2000 °C. The reason is considered to be as follows. Soft carbon has graphitized sites, a turbulent structure sites, and unorganized sites, and the ratio between them changes depending on the heat treatment temperature. The turbulent layer structure is originally stacked in the order ABAB, and it is necessary to change to AAAA upon lithiation. However, stacking changes do not easily occur due to structural distortion, so the amount of lithium inserted in the turbulent structure is about 30% of that of the graphite part. Since unorganized carbon has multiple sites where lithium ions are

inserted, about 90% of lithium can be inserted compared with the graphite part. In addition, it is considered that unorganized carbon changes to a turbulent structure when annealed up to 2000 °C, and the turbulent structure shifts to a graphite structure when treated at 2000 °C or higher. Therefore, the capacity decreases with increasing heat treatment temperature, and then the capacity increases to near the theoretical capacity of graphite. It is not completely clear why carbon heat-treated below 1000 °C exhibits a very large reversible capacity. Various storage mechanisms (*e.g.*, LiC_2 model[57], cavity model[58]) have been proposed, but the issue is still controversial.

Similar to graphite, when lithium is intercalated between graphene–graphene layers, a peak corresponding to the interlayer distance shifts to a lower angle in XRD.[59–61] In addition, the insertion of lithium into the nanopore can be confirmed by the decrease of scattering intensity from nanopore by small angle X-ray scattering (SAXS) measurement.[61,62] Numerous studies have been conducted on the chemical state of lithium atoms stored in nanopores using ^{7}Li NMR, and it is concluded that lithium atoms exist in a cluster state.[63–68] Since Knight shift is observed, it is considered that this cluster has metallic properties.[69,70]

The lithium insertion of the three carbon materials is explained in Figure 1.10. Lithium is intercalated into the graphite interlayer until it reaches LiC_6. The amount of lithium intercalated between the layers decreases in the order of graphite > soft carbon > hard carbon.

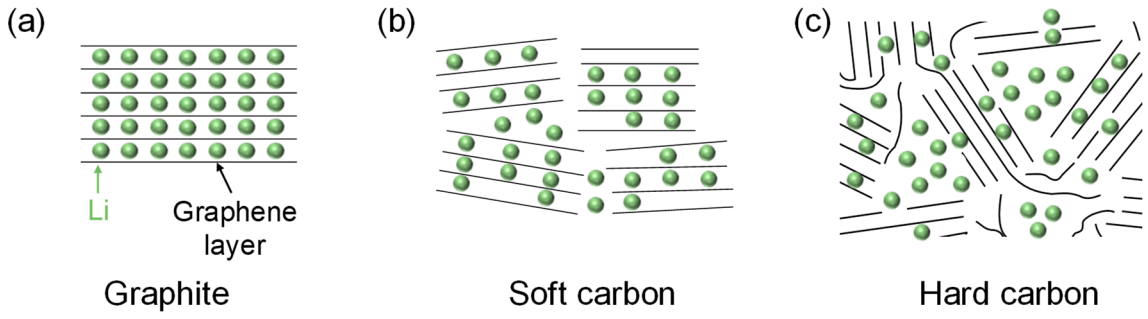

Figure 1.10 Schematic diagrams of the lithium storage mechanism in carbon materials. (a) Graphite, (b) soft carbon and (c) hard carbon.

1.5 Sodium ion batteries

1.5.1 Na^+ as a guest ion in battery system

With the increasing political and social demand for a sustainable society, there is a strong need to transit from fossil fuels to renewable energy sources and from gasoline vehicles to electric vehicles (EV). Since renewable energy sources (*e.g.*, solar, wind) do not produce electricity consistently, large-scale energy storage devices are required to store excess energy and stabilize power supply. Currently, LIBs are mainly used as a power source for portable devices (*e.g.*, mobile phones, laptop computers), but it is strongly needed to expand to aforementioned large-scale applications in the future.

The demand for LIBs is increasing year by year, and EV applications account for more than half. And the market size of in-vehicle LIB is expected to grow 3 times in the next 10 years (**Figure 1.11**).[71] As mentioned above, LIBs are produced using minor metals such as Li and Co. Due to the rapid increase in demand, it is predicted that the supply of these elements will not keep up by 2030.[72] Against this background, there is a need to develop batteries that do not use minor metals to replace LIBs. The sodium-ion battery (NIB), a classical analogue of LIBs, has attracted significant attention over the past decade as an alternative to LIBs because sodium is the second lightest alkali metal and its resources are widely available from the Earth's crust and the sea.[8,9,73]

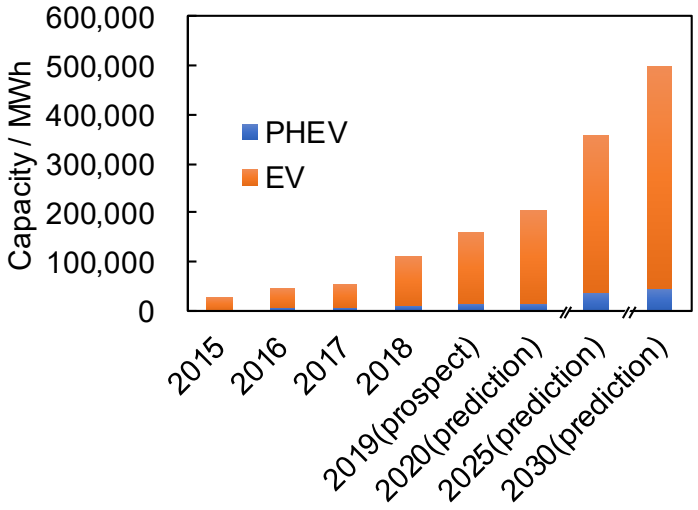

Figure 1.11 Forecast of market scale for automotive LIBs.[71]

1.5.2 Anode materials for sodium ion batteries

Figure 1.12 shows the performance comparison chart of anode materials for sodium ion batteries. Anode materials shown in blue are substances that charge and discharge by making an alloy with sodium. Although the capacity is large, it suddenly decreases due to a large volume change with alloying. As with Sn and Si in LIBs, a lot of attempts have been made to accommodate the large volume change and retain the high capacity by creating nanostructures, but not yet reached a practical level. Anode materials shown in green have low capacity and high reaction potential, resulting in low battery energy density (<200 Wh kg^{-1}). Graphite (gray) generally does not store much sodium, but in an electrolyte using an ether solvent, it exhibits a capacity over 100 mAh g^{-1} by the intercalation of solvated sodium ions ("co-intercalation"). [74,75] Since intercalation and deintercalation proceeds without desolvation, the battery exhibits a good high-rate capability, but cannot achieve high energy density. Considering all the factors (*e.g.*, capacity, reaction potential, cycle performance, cost), hard carbon is the most promising material.

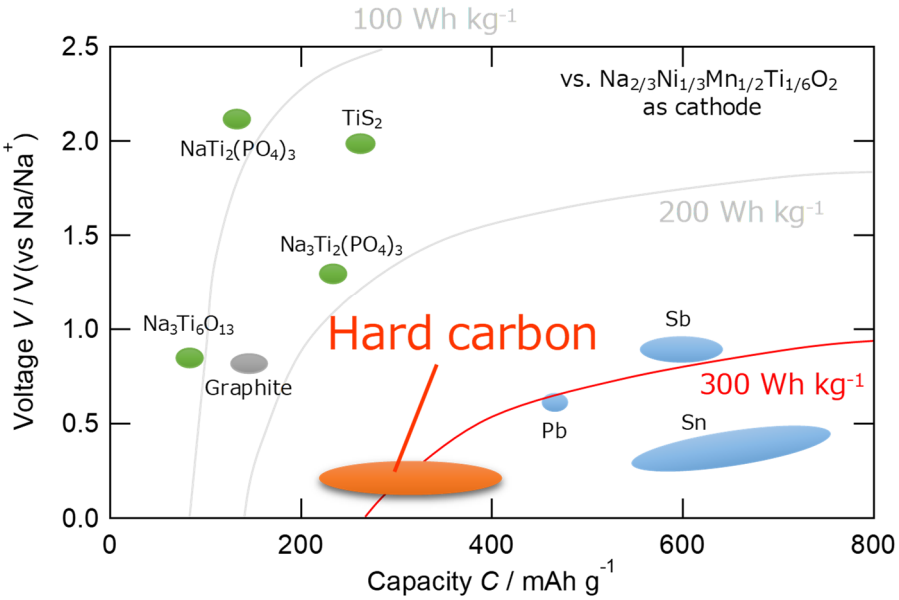

Figure 1.12 Average potential versus capacity for selected anode materials of NIBs.[9]

1.6 Purpose of this study

For the practical application of NIBs, it is essential to improve the performance of hard carbon anodes. However, the Na storage mechanism of hard carbon has not been fully elucidated due to its disordered atomic structure, difficulty of measurement due to extremely high reactivity, and diversity of raw materials. Therefore, at present, the structural optimization of hard carbon is carried out by trial and error without any specific design guidelines. In this paper, the author aims to improve the performance of hard carbon according to the procedure shown in **Figure 1.13**. First is to synthesize hard carbon whose microstructure changes continuously. Second is to clarify the correlation between the microstructure of the hard carbon and the electrode characteristics, and propose an optimal hard carbon structure. Third is to design an electrolyte that raises the performances of hard carbon to a practical level.

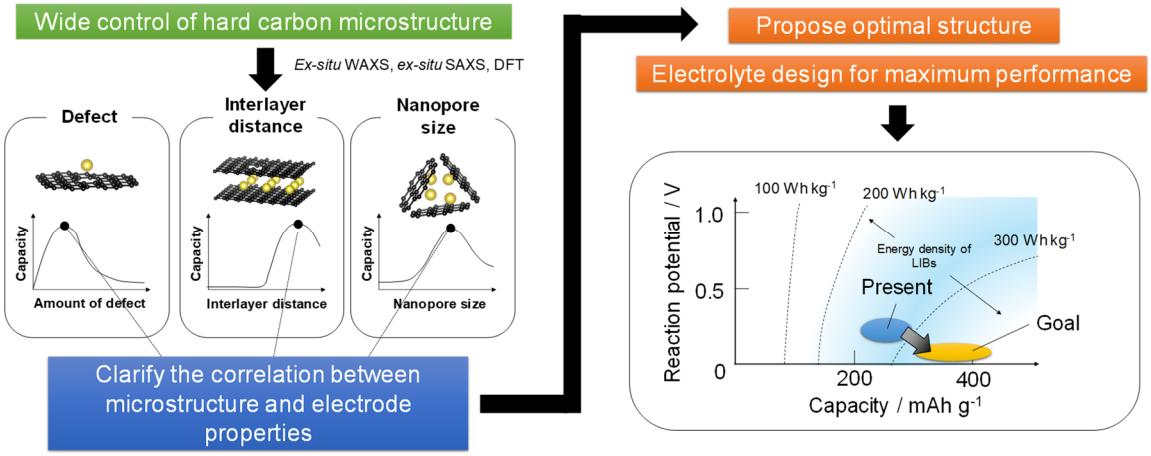

Figure 1.13 Analysis and synthesis approach to realize high performance hard carbon electrode.

References

1. Petroleum British. *Statistical Review of World Energy 2019*. (2019).
2. The Royal Swedish Academy of Sciences. Press release of the Nobel Prize in Chemistry 2019. https://s3.eu-de.cloud-object-storage.appdomain.cloud/kva-image-pdf/2019/10/press_ke_en_19.pdf (2019).
3. Tarascon, J. & Armand, M. Issues and challenges facing rechargeable lithium batteries. *Nature* **414**, 359–367 (2001).
4. Kim, S. W., Seo, D. H., Ma, X., Ceder, G. & Kang, K. Electrode materials for rechargeable sodium-ion batteries: Potential alternatives to current lithium-ion batteries. *Advanced Energy Materials* vol. 2 710–721 (2012).
5. Nayak, P. K., Yang, L., Brehm, W. & Adelhelm, P. From Lithium-Ion to Sodium-Ion Batteries: Advantages, Challenges, and Surprises. *Angew. Chemie Int. Ed.* **57**, 102–120 (2018).
6. Palacín, M. R. Recent advances in rechargeable battery materials: A chemist's perspective. *Chem. Soc. Rev.* **38**, 2565–2575 (2009).
7. Dahbi, M., Yabuuchi, N., Kubota, K., Tokiwa, K. & Komaba, S. Negative electrodes for Na-ion batteries. *Phys. Chem. Chem. Phys.* **16**, 15007 (2014).
8. Kubota, K. & Komaba, S. Review—Practical Issues and Future Perspective for Na-Ion Batteries. *J. Electrochem. Soc.* **162**, A2538–A2550 (2015).
9. Yabuuchi, N., Kubota, K., Dahbi, M. & Komaba, S. Research development on sodium-ion batteries. *Chem. Rev.* **114**, 11636–11682 (2014).
10. Mizushima, K., Jones, P. C., Wiseman, P. J. & Goodenough, J. B. LixCoO2 (0<x<1): A new cathode material for batteries of high energy density. *Mater. Res. Bull.* **15**, 783–789 (1980).
11. Peled, E. The Electrochemical Behavior of Alkali and Alkaline Earth Metals in Nonaqueous Battery Systems—The Solid Electrolyte Interphase Model. *J. Electrochem. Soc.* **126**, 2047–2051 (1979).
12. Peled, E., Golodnitsky, D. & Ardel, G. Advanced model for solid electrolyte interphase electrodes in liquid and polymer electrolytes. *J. Electrochem. Soc.* **144**, (1997).
13. Eshkenazi, V., Peled, E., Burstein, L. & Golodnitsky, D. XPS analysis of the SEI formed on carbonaceous materials. *Solid State Ionics* **170**, 83–91 (2004).
14. Kanamura, K., Shiraishi, S. & Takehara, Z. I. Electrochemical deposition of very smooth lithium using nonaqueous electrolytes containing HF. *J. Electrochem. Soc.* **143**, 2187–2197 (1996).
15. Fan, X. *et al.* Highly Fluorinated Interphases Enable High-Voltage Li-Metal Batteries. *Chem* **4**, 174–185 (2018).
16. Choudhury, S. & Archer, L. A. Lithium Fluoride Additives for Stable Cycling of Lithium Batteries at High Current Densities. *Adv. Electron. Mater.* **2**, (2016).

17. Datta, M. K. *et al.* Tin and graphite based nanocomposites: Potential anode for sodium ion batteries. *J. Power Sources* **225**, 316–322 (2013).
18. Suryawanshi, A. *et al.* Indanthrone derived disordered graphitic carbon as promising insertion anode for sodium ion battery with long cycle life. *Electrochim. Acta* **146**, 218–223 (2014).
19. Fong, R., von Sacken, U. & Dahn, J. R. Studies of Lithium Intercalation into Carbons Using Nonaqueous Electrochemical Cells. *J. Electrochem. Soc.* **137**, 2009–2013 (1990).
20. Ohzuku, T., Iwakoshi, Y. & Sawai, K. Formation of Lithium-Graphite Intercalation Compounds in Nonaqueous Electrolytes and Their Application as a Negative Electrode for a Lithium Ion (Shuttlecock) Cell. *J. Electrochem. Soc.* **140**, 2490–2498 (1993).
21. Mabuchi, A. A Survey on the Carbon Anode Materials for Rechargeable Lithium Batteries. *TANSO* **1994**, 298–306 (1994).
22. Scharner, S., Weppner, W. & Schmid-Beurmann, P. Evidence of two-phase formation upon lithium insertion into the Li1.33Ti1.67O4 spinel. *J. Electrochem. Soc.* **146**, 857–861 (1999).
23. Ohzuku, T. & Ueda, A. Why transition metal (di) oxides are the most attractive materials for batteries. *Solid State Ionics* **69**, 201–211 (1994).
24. Ohzuku, T., Ueda, A. & Yamamota, N. Zero-Strain Insertion Material of Li[Li1/3Ti5/3]O4 for Rechargeable Lithium Cells. *J. Electrochem. Soc.* **142**, 2–6 (1995).
25. Oberlin, A., Endo, M. & Koyama, T. Filamentous growth of carbon through benzene decomposition. *J. Cryst. Growth* **32**, 335–349 (1976).
26. Iijima, S. Helical microtubules of graphitic carbon. *Nature* **354**, 56–58 (1991).
27. Iijima, S. & Ichihashi, T. Single-shell carbon nanotubes of 1-nm diameter. *Nature* **363**, 603–605 (1993).
28. Novoselov, K. S. *et al.* Electric field in atomically thin carbon films. *Science (80-.).* **306**, 666–669 (2004).
29. Yoshino, A. The birth of the lithium-ion battery. *Angewandte Chemie - International Edition* vol. 51 5798–5800 (2012).
30. Gao, B. *et al.* Electrochemical intercalation of single-walled carbon nanotubes with lithium. *Chem. Phys. Lett.* **307**, 153–157 (1999).
31. Che, G., Lakshmi, B. B., Fisher, E. R. & Martin, C. R. Carbon nanotubule membranes for electrochemical energy storage and production. *Nature* **393**, 346–349 (1998).
32. Frackowiak, E., Gautier, S., Gaucher, H., Bonnamy, S. & Beguin, F. Electrochemical storage of lithium multiwalled carbon nanotubes. *Carbon N. Y.* **37**, 61–69 (1999).
33. Wang, X. X., Wang, J. N., Chang, H. & Zhang, Y. F. Preparation of short carbon nanotubes and application as an electrode material in Li-ion batteries. *Adv. Funct. Mater.* **17**, 3613–3618 (2007).
34. Mizutani, Y., Abe, T., Inaba, M. & Ogumi, Z. Creation of nanospaces by intercalation of

alkali metals into graphite in organic solutions. *Synth. Met.* **125**, 153–159 (2001).

35. Ge, P. & Fouletier, M. Electrochemical intercalation of sodium in graphite. *Solid State Ionics* **28**–**30**, 1172–1175 (1988).
36. Wang, J. *et al.* Fire-extinguishing organic electrolytes for safe batteries. *Nat. Energy* **3**, 22–29 (2018).
37. Komaba, S., Hasegawa, T., Dahbi, M. & Kubota, K. Potassium intercalation into graphite to realize high-voltage/high-power potassium-ion batteries and potassium-ion capacitors. *Electrochem. commun.* **60**, 172–175 (2015).
38. Franklin, R. E. Crystallite growth on graphitized and non-grphitized carbons. *Proc. R. Soc. A* **209**, 196–218 (1951).
39. Dahn, J. R., Zheng, T., Liu, Y. & Xue, J. S. Mechanisms for Lithium Insertion in Carbonaceous Materials. *Science (80-.).* **270**, 590–593 (1995).
40. Wilson, A. M., Xingb, W., Zank, G., Yatesd, B. & Dahn, J. R. Pyrolysed pitch-polysilane blends for use as anode materials in lithium ion batteries II: the effect of oxygen. *Solid State Ionics ~Moli k~ergy I.rd* **100**, 259–266 (1997).
41. Wang, D. *et al.* Uniformly expanded interlayer distance to enhance the rate performance of soft carbon for lithium-ion batteries. *Ionics (Kiel).* **25**, 1531–1539 (2019).
42. Forse, A. C. *et al.* New Insights into the Structure of Nanoporous Carbons from NMR, Raman, and Pair Distribution Function Analysis. *Chem. Mater.* **27**, 6848–6857 (2015).
43. Deringer, V. L. *et al.* Towards an atomistic understanding of disordered carbon electrode materials. *Chem. Commun.* **54**, 5988–5991 (2018).
44. Wang, H. L., Shi, Z. Q., Jin, J., Chong, C. Bin & Wang, C. Y. Properties and sodium insertion behavior of Phenolic Resin-based hard carbon microspheres obtained by a hydrothermal method. *J. Electroanal. Chem.* **755**, 87–91 (2015).
45. Zhou, Z. *et al.* Controlling the Structure and Electrochemical Properties of Anode Prepared from Phenolic Resin for Li-ion Batteries. *Int. J. Electrochem. Sci.* **14**, 6976–6985 (2019).
46. Buiel, E. & Dahn, J. R. Reduction of the Irreversible Capacity in Hard-Carbon Anode Materials Prepared from Sucrose for Li-Ion Batteries. *J. Electrochem. Soc.* **145**, 1977 (1998).
47. Zhang, H., Ming, H., Zhang, W., Cao, G. & Yang, Y. Coupled Carbonization Strategy toward Advanced Hard Carbon for High-Energy Sodium-Ion Battery. *ACS Appl. Mater. Interfaces* **9**, 23766–23774 (2017).
48. Yin, L. *et al.* Self-assembly of disordered hard carbon/graphene hybrid for sodium-ion batteries. *J. Power Sources* **305**, 156–160 (2016).
49. Väli, R., Jänes, A., Thomberg, T. & Lust, E. Synthesis and characterization of D-glucose derived nanospheric hard carbon negative electrodes for lithium- and sodium-ion batteries. *Electrochim. Acta* **253**, 536–544 (2017).
50. Zhao, L. *et al.* Voronoi-Tessellated Graphite Produced by Low-Temperature Catalytic

Graphitization from Renewable Resources. *ChemSusChem* **10**, 3409–3418 (2017).

51. Väli, R., Jänes, A., Thomberg, T. & Lust, E. D-Glucose Derived Nanospheric Hard Carbon Electrodes for Room-Temperature Sodium-Ion Batteries. *J. Electrochem. Soc.* **163**, A1619–A1626 (2016).
52. Li, Y., Hu, Y.-S., Titirici, M.-M., Chen, L. & Huang, X. Hard Carbon Microtubes Made from Renewable Cotton as High-Performance Anode Material for Sodium-Ion Batteries. *Adv. Energy Mater.* **6**, 1600659 (2016).
53. Tang, J., Etacheri, V. & Pol, V. G. From Allergens to Battery Anodes : Nature-Inspired , Pollen Derived Carbon Architectures for Room- and Elevated- Temperature Li-ion Storage. *Sci. Rep.* **6**, 1–8 (2016).
54. Zhang, Y. *et al.* Honeycomb-like Hard Carbon Derived from Pine Pollen as High-Performance Anode Material for Sodium-Ion Batteries. *ACS Appl. Mater. Interfaces* **10**, 42796–42803 (2018).
55. Dahn, J. R. Phase diagram of LixC6. *Phys. Rev. B* **44**, 9170–9177 (1991).
56. Whitehead, A. H., Edström, K., Rao, N. & Owen, J. R. In situ X-ray diffraction studies of a graphite-based Li-ion battery negative electrode. *J. Power Sources* **63**, 41–45 (1996).
57. Bindra, C., Nalimova, V. A., Sklovsky, D. E., Benes, Z. & Fischer, J. E. Super dense LiC2 as a high capacity Li intercalation anode. *J. Electrochem. Soc.* **145**, 2377–2380 (1998).
58. Mabuchi, A., Tokumitsu, K., Fujimoto, H. & Kasuh, T. Charge-Discharge Characteristics of the Mesocarbon Miocrobeads Heat-Treated at Different Temperatures. *J. Electrochem. Soc.* **142**, 1041–1046 (2000).
59. Buiel, E. & Dahn, J. R. Li-insertion in hard carbon anode materials for Li-ion batteries. *Electrochim. Acta* **45**, 121–130 (1999).
60. Yamazaki, S. *et al.* Study of the states of Li doped in carbons as an anode of LiB by 7Li NMR spectroscopy. *J. Mol. Struct.* **441**, 165–171 (1998).
61. Stevens, D. A. & Dahn, J. R. The Mechanisms of Lithium and Sodium Insertion in Carbon Materials. *J. Electrochem. Soc.* **148**, A803 (2001).
62. Nagao, M. *et al.* Structure Characterization and Lithiation Mechanism of Nongraphitized Carbon for Lithium Secondary Batteries. *J. Electrochem. Soc.* **153**, A914 (2006).
63. Gerald, R. E. *et al.* 7Li NMR study of intercalated lithium in curved carbon lattices. *J. Power Sources* **89**, 237–243 (2000).
64. Hayes, S. E., Guidotti, R. A., Even, W. R., Hughes, P. J. & Eckert, H. 7Li solid-state nuclear magnetic resonance as a probe of lithium species in microporous carbon anodes. *J. Phys. Chem. A* **107**, 3866–3876 (2003).
65. Tatsumi, K. *et al.* 7Li NMR studies on a lithiated non-graphitizable carbon fibre at low temperatures. *Chem. Commun.* 687–688 (1997) doi:10.1039/A700221A.
66. Letellier, M. *et al.* The first in situ 7Li nuclear magnetic resonance study of lithium insertion in hard-carbon anode materials for Li-ion batteries. *J. Chem. Phys.* **118**, 6038–

6045 (2003).
67. Jung, Y. *et al.* Electrochemical Insertion of Lithium into Polyacrylonitrile-Based Disordered Carbons. *J. Electrochem. Soc.* **144**, 4279 (1997).
68. Morita, R. *et al.* Combination of solid state NMR and DFT calculation to elucidate the state of sodium in hard carbon electrodes. *J. Mater. Chem. A* **4**, 13183–13193 (2016).
69. Dai, Y., Wang, Y., Eshkenazi, V., Peled, E. & Greenbaum, S. G. Lithium-7 Nuclear Magnetic Resonance Investigation of Lithium Insertion in Hard Carbon. *J. Electrochem. Soc.* **145**, 1179 (1998).
70. Gautier, S. *et al.* Influence of the pyrolysis conditions on the nature of lithium inserted in hard carbons. *J. Phys. Chem. A* **105**, 5794–5800 (2001).
71. *Yano Research Institute Ltd., Automotive Lithium-ion Batteries*. (2019).
72. Agency for Natural Resources and Energy. https://www.enecho.meti.go.jp/about/special/johoteikyo/cobalt.html (2019).
73. Kubota, K., Dahbi, M., Hosaka, T., Kumakura, S. & Komaba, S. Towards K-Ion and Na-Ion Batteries as "Beyond Li-Ion". *Chem. Rec.* **18**, 459–479 (2018).
74. Kim, H. *et al.* Sodium intercalation chemistry in graphite. *Energy Environ. Sci.* **8**, 2963–2969 (2015).
75. Jache, B. & Adelhelm, P. Use of graphite as a highly reversible electrode with superior cycle life for sodium-ion batteries by making use of co-intercalation phenomena. *Angew. Chemie - Int. Ed.* **53**, 10169–10173 (2014).

2 Synthesis and nanostructure control of hard carbon

2.1 Introduction

Hard carbons are synthesized by carbonizing raw materials containing carbon. **Table 2.1** summarizes the raw materials, synthesis methods and Na half-cell performance of hard carbons reported in 2016 and 2017. As for the annealing temperature, the temperature at which the capacity is the largest in the paper is described.

Table 2.1 Synthesis conditions and cell performance of various hard carbons.

Raw material	T^a	1C^b	1D^c	ICE^d	V^e	I^f
Alfalfa leaf[1]	700	1029	433	42.1%	0.01-2	100
Aniline[2]	700	653	336	51.5%	0.01-3	30
Apple-biowaste[3]	1100	400	245	61.3%	0.02-3	4
Argan shells[4]	1200	384	333	86.8%	0-2	25
Cellulose[5]	1300	509	323	63.5%	-	20
Cellulose[6]	1600	373	310	83.0%	0.01-3	37.2
Corn cob[7]	1300	347	298	86.0%	0-2	30
Corn stalks[8]	1200	612	322	52.6%	0.01-3	50
D-(+)-glucose[9]	1100	525	273	52.0%	0.005-1.5	25
Dandelion[10]	1200	626	372	59.4%	0.001-3	50
Holly leaf[11]	800	636	318	50.0%	0.01-3	20
Kelp[12]	1400	525	334	63.6%	0.01-2	20
Leonardite humic acid[13]	1500	473	345	73.0%	0.001-2.5	25
Ligin[14]	810	933	381	40.8%	0.01-3	50
Macadamia shell[15]	1400	329	301	91.4%	0-2.5	-
Mangosteen shel[16]	1500	398	330	83.0%	0-2	20
Orange peel[17]	800	500	210	42.0%	0.01-3	50
Peanut shell[18]	1100	438	298	68.0%	0.02-200	20
Pinecone Biomass[19]	1400	429	366	85.4%	0.001–2	20
Pitch and phenolic resin[20]	1400	323	284	88.0%	-0.01-2	30
Polyacrylonitrile[21]	1300	375	261	69.6%	0.01-2.7	20
Poly-Acrylonitrile[22]	2200	460	262	57.0%	0-2.25	50

Poly-Acrylonitrile[23]vv	1100	328	241	73.5%	0-3	50
Polyaniline[24]	1150	560	280	50.0%	0-2.5	25
Polyurethane[25]	700	600	230	38.3%	0.01-3	20
Polyvinylpyrrolidone[26]	1000	568	271	47.7%	0.01-2.5	30
Rape seed shuck[27]	700	408	245	60.0%	0.01-3	100
Sodium alginate[28]	800	554	217	39.1%	0.01-3	100
Starch powder from rice[29]	1100	430	275	64.0%	0.02-1	18
Sucrose[30]	1600	470	301	64.0%	0-2	25
Sucrose[31]	700	807	355	44.0%	0.01-3	50
Sucrose[32]	1100	419	315	75.2%	0.01-1.5	28
Sucrose and phenol formaldehyde resin[33]	1400	367	319	87.0%	0-2	30
Switchgrass[34]	2050	328	210	64.0%	0.01-2	50
Thiourea, resorcinol[35]	600	900	250	27.8%	0.01-3	100
Tire rubber[36]	1600	415	274	66.0%	0-3	20
Wool[37]	1100	480	303	63.1%	0-2	10
Zinc citrate[38]	800	1490	439	29.4%	0-3	30

a: Annealing temperature [°C]

b: Capacity of first charge [mAh g^{-1}]

c: Capacity of first discharge [mAh g^{-1}]

d: Initial Coulombic efficiency [%]

e: Voltage range of charge-discharge test [V]

f: Current density of charge-discharge test [mA g^{-1}]

Various materials such as resins, sugars, and plants are used as raw materials. In many cases, the reversible capacity is maximized when it is annealed at around 1200 °C. Since the mechanism of sodium insertion into hard carbon is still controversial, the correlation between the microstructure and battery characteristics is also unclear. Since there is no design guideline for the optimal hard carbon structure, the materials and synthesis conditions are optimized based on the experience of researchers and trial and error.

Because the measurement conditions (*e.g.*, voltage range, current density, tap density of electrode, electrolyte, measurement temperature) are different, it is not possible to make a general comparison, but the cell performances listed in **Table 2.1** are summarized in **Figure 2.1**. There are

many reports that the capacity is around 300 mAh g^{-1} and the initial Coulomb efficiency (ICE) is around 70%. There are hard carbons containing elements other than carbon (*e.g.*, P, S, Zn), and it is considered that some have a value larger than that of pure hard carbon. From the perspective of practical application, battery performance is not satisfied only by having a large capacity, but by achieving a high ICE. Therefore, in the present thesis, I aimed for a capacity of 300 mAh g^{-1} or more and ICE > 90% (the orange region in Figure 2.1).

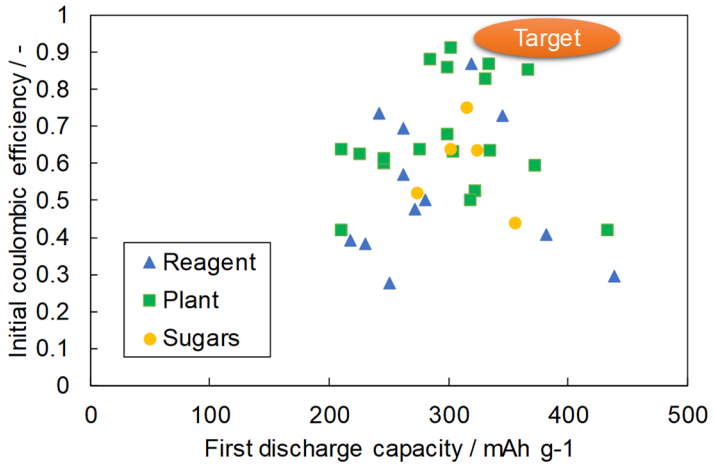

Figure 2.1 Performance comparison chart of various hard carbons and target area in this thesis.

2.2 Synthesis and characterization of hard carbons

In this chapter, high-performance hard carbon was synthesized for use in the analysis of the sodium storage mechanism. From the viewpoint of reproducibility and yield, saccharides were used as raw materials. As a synthesis method, a hydrothermal treatment was used because this method can reduce the active surface area of hard carbon and achieve high ICE.

2.2.1 Material synthesis

Hard carbon was prepared by a hydrothermal method.[39] Saccharides (glucose, fructose, xylose,

sucrose) were used as raw materials. Aqueous sugar solution was prepared by dissolving 0.05 mol (0.025 mol in the case of sucrose) of saccharides in 10 mL of deionized water. For hydrothermal reactions, solution was put into a polytetrafluoroethylene-lined stainless-steel autoclave. After 5 h hydrothermal treatment at 200 °C, the obtained black carbon powder was further carbonized at 1000 °C for 5 h in an Ar atmosphere.

2.2.2 Electrochemical tests

For electrode preparation, hard carbon samples were mixed with CMC at a weight ratio of 9:1. The electrochemical measurements were conducted by using 2032-type coin-cells. The electrolyte was 1 mol dm^{-3} $NaPF_6$ in ethyl carbonate (EC)/diethyl carbonate (DEC) (1:1 by volume, Kishida Chemical), the separator was glass filter (GC-50, Advantec), and the counter electrode was Na metal. Galvanostatic cycling tests were carried out between 0.01 and 2.5 V at a current density of 20 mA g^{-1} using charge-discharge units (HJ1001SD8, Hokuto Denko Corporation).

2.3 Effect of raw materials on sodium storage behavior

Figure 2.2 shows galvanostatic charge-discharge curves of hard carbon electrodes with three kinds of monosaccharide (glucose, fructose, xylose (**Figure 2.3**)).

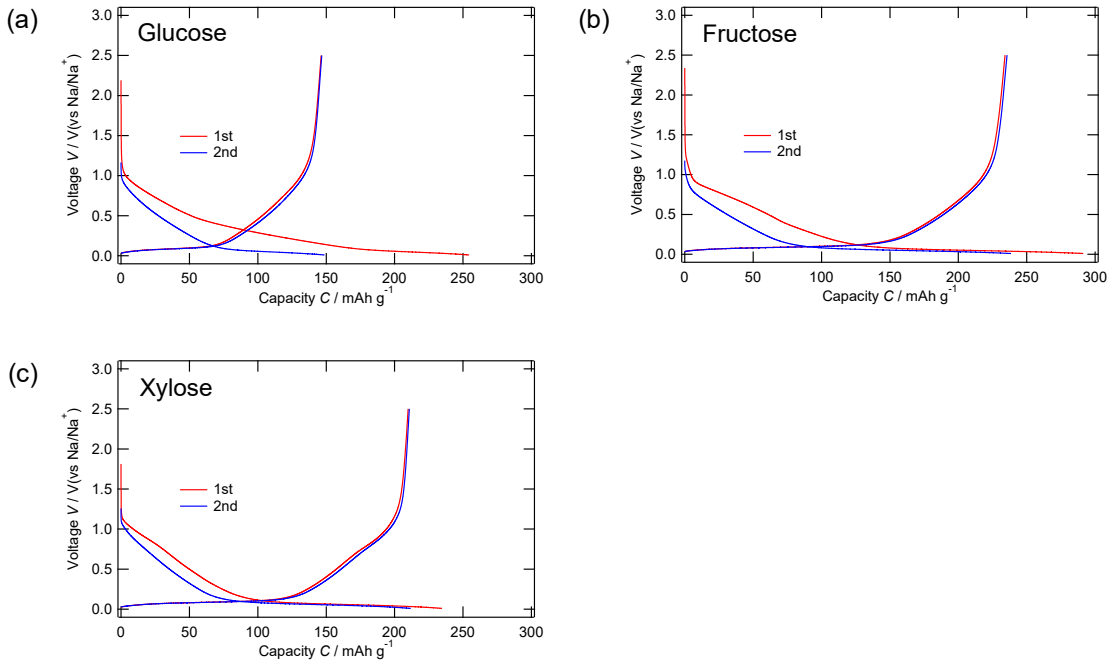

Figure 2.2 Galvanostatic charge/discharge curves of hard carbon electrodes.

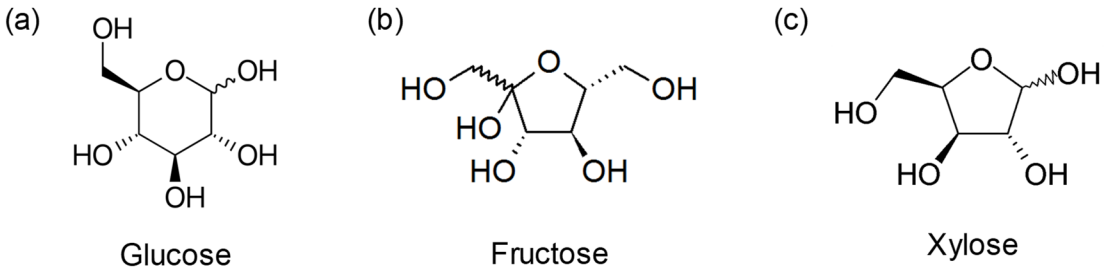

Figure 2.3 Structure of three monosaccharides

It can be confirmed that Na storage characteristics change depending on the raw materials. For example, the hard carbon synthesized from glucose has a small flat part capacity and showed small ICE. On the other hand, the capacity was maximized when the raw material was fructose, and ICE was maximized when xylose was used. The difference in cell performance is considered to reflect the microstructure of hard carbon samples. The synthesis route of hard carbon precursors by hydrothermal treatment of saccharide is explained in **Figure 2.4**.[40] It is known that the conversion rate, selectivity, and reaction temperature that change to furfurals vary greatly depending on the

type of saccharide and pH of the solution.[40,41] **Figure 2.5** shows SEM images of synthesized hard carbon samples. It is confirmed that the shape and size vary greatly depending on the type of saccharide. Based on the mechanism shown in Figure 2.4, the same product should be synthesized from glucose and fructose, but particle size and battery characteristics are different. This is because the isomerization of glucose to fructose proceeds slowly, so that the concentration of HMF and pH of the solution vary depending on whether the raw material is glucose or fructose. It can be seen that slight differences have a significant effect on the product.

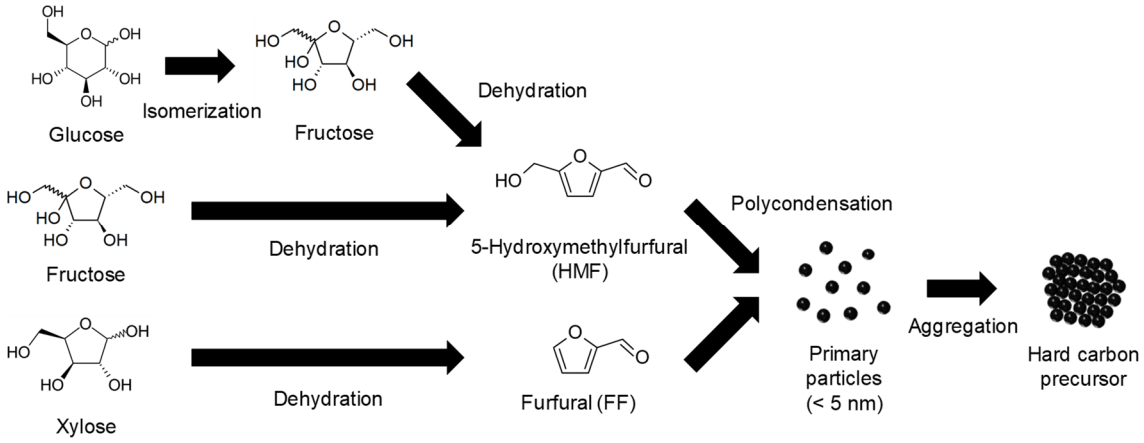

Figure 2.4 Mechanism of formation and growth of hard carbon precursors.[40]

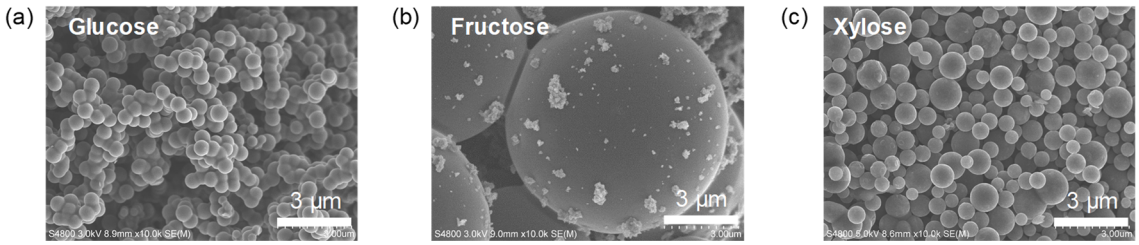

Figure 2.5 SEM images of synthesized hard carbon samples.

Figure 2.6 shows the X-ray measurement results of the hard carbon precursor (without annealing) and the sample annealed at various temperatures under Ar atmosphere. In the precursor, no peak derived from the in-plane graphene structure (around 44°) was observed in XRD, and no

nanopore-derived peak was observed in SAXS. Even when heat treatment was performed at 300 °C, the structure hardly changed and remained amorphous. It is confirmed that graphitization and formation of nanopores occur above 600 °C. The precursor does not contain nanopores, but since the degree of cross-linkage in the precursor has a great influence on the structure of the nanopores as reported previously,[42,43] it is assumed that the type of raw material changes how nanopores are developed.

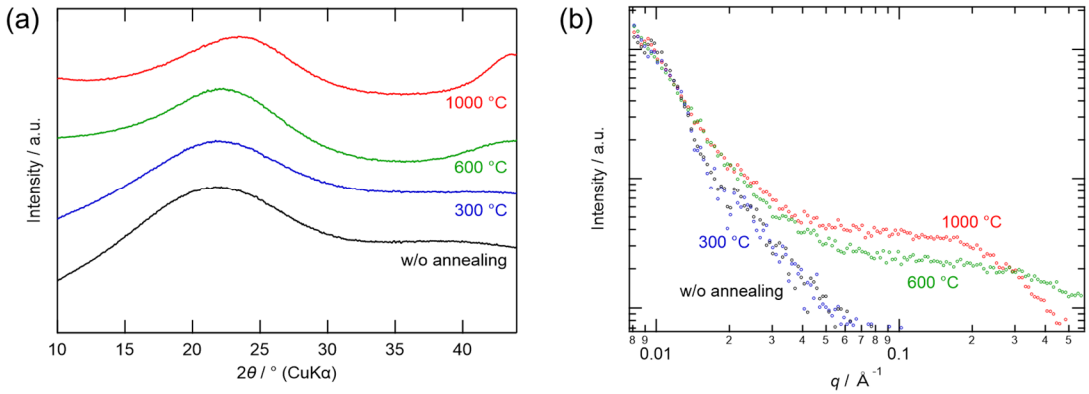

Figure 2.6 (a) XRD pattern and (b) SAXS profiles of hard carbon samples heat treated at various temperatures.

In order to further improve the battery characteristics of hard carbon, carbon samples were synthesized by mixing two or three sugars in various ratios. The results of the charge-discharge test are shown in **Figure 2.7**.

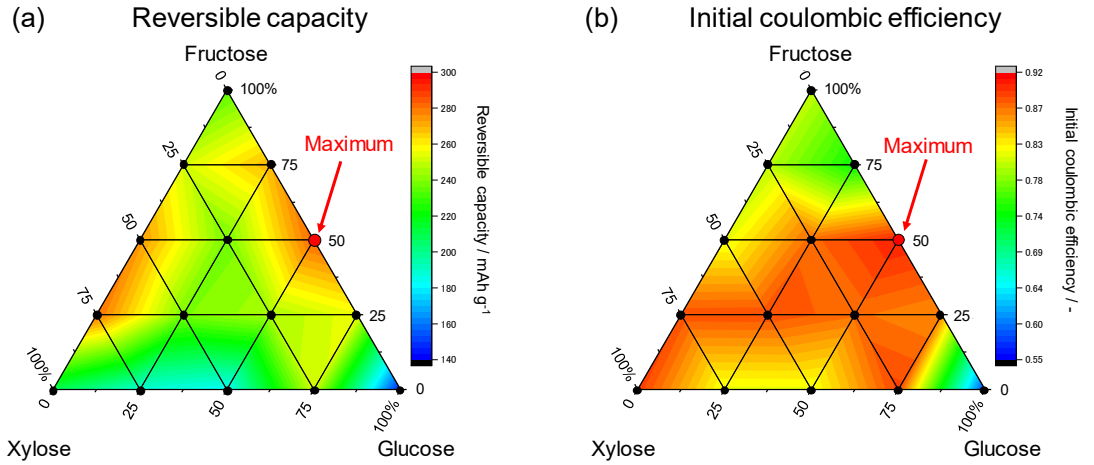

Figure 2.7 (a) Reversible capacity and (b) initial coulomb efficiency of hard carbon samples synthesized from two or three kinds of saccharide.

By mixing several kinds of sugars, the reversible capacity and ICE increased compared with when synthesized from one kind of saccharide. Hard carbon synthesized from a mixed aqueous solution of glucose:fructose = 1:1 in molar ratio showed the maximum reversible capacity (283 mAh g^{-1}) and ICE (90.5%). Characterizations of the synthesized hard carbons are shown in **Figure 2.8**. XRD patterns and Raman spectra were slightly different depending on the raw material, but there was no significant difference. On the other hand, in SAXS profiles, the scattering intensity derived from nanopores increased drastically. Assuming that the nanopore is spherical, the scattering intensity $I(q)$ can be described as follows:

$$I(q) = N\left|4\pi\Delta\rho\int_0^r \frac{\sin(qr)}{qr} r^2\, dr\right|^2 \qquad (2.1)$$

where N is the number of nanopores, $\Delta\rho$ is the difference of electron density between the nanopores and the carbon matrix. From the position of the shoulder of the SAXS pattern, it is assumed that the size of the nanopore is almost the same in all samples, so the value of the integral part is considered to be almost equal. Form equation (2.1), when the proportion of material is glucose:fructose = 1:1, it is suggested that N is large or $\Delta\rho$ is large. Since there is no significant change in the XRD and Raman results, it is considered that the electron density of the carbon matrix is almost the same.

Therefore, it seems that the number of nanopores was greatly increased by using a mixed aqueous solution of several saccharides as the raw material.

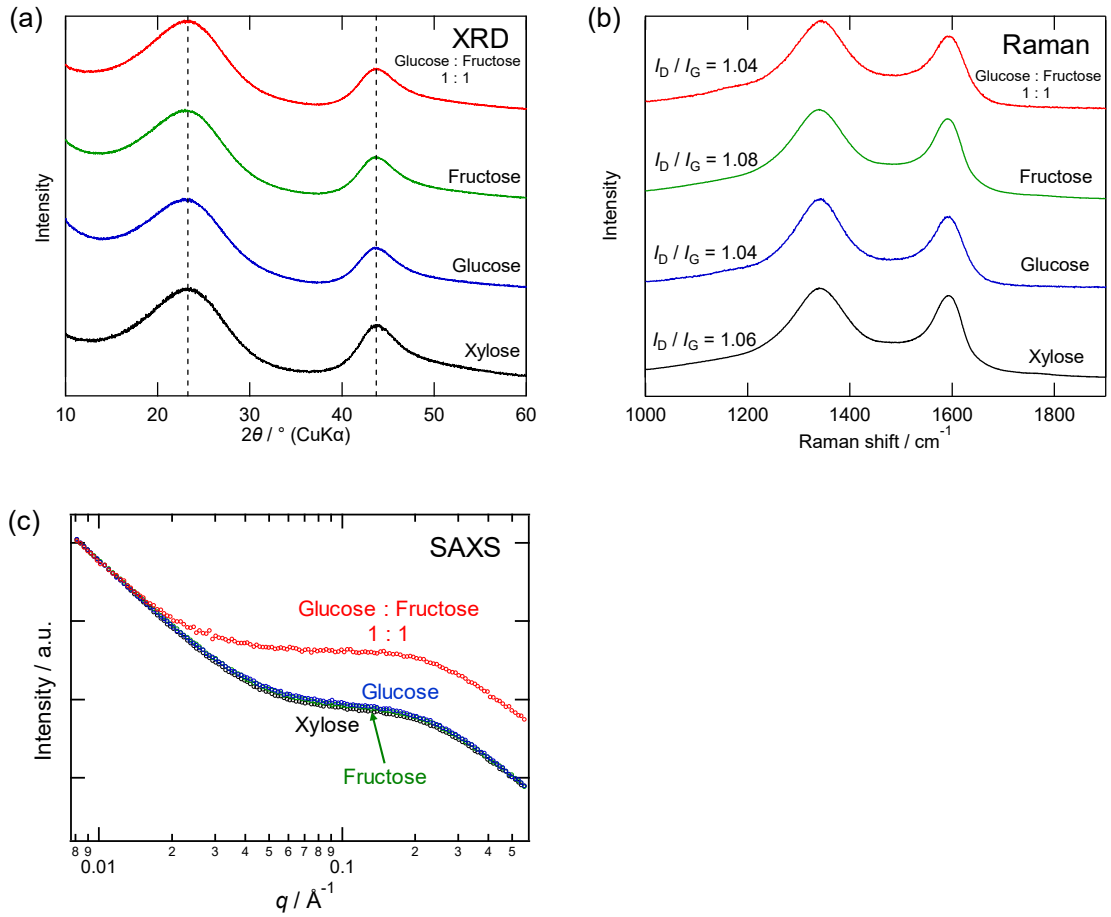

Figure 2.8 Characterizations of the synthesized hard carbons. (a) XRD patterns and (b) Raman spectra and (c) SAXS profiles.

2.4 Effect of annealing temperature on sodium storage behavior

A sucrose molecule is formed by an α-1,2-glycoside bond between one glucose molecule and one fructose molecule. Since sucrose is separated into fructose:glucose = 1:1 by hydrolysis, almost the same hard carbon can be synthesized even if sucrose is used as a raw material. Thereafter, hard carbon samples were synthesized from sucrose.

It is known that microstructure and Na storage behavior of hard carbon change drastically

depending on the heat treatment temperature. Hard carbon samples synthesized from sucrose were annealed at temperatures (*T*) from 1000 to 2000 °C. The prepared products are denoted HC-*T*. In the following, the description will focus on charge-discharge characteristics. The microstructure of hard carbon will be discussed in Chapter 3.

Figure 2.9 shows the galvanostatic charge–discharge curves measured at 20 mA g^{-1}. The results are summarized in **Table 2.2**. Among all the samples, HC-1400 showed the highest discharge capacity (348 mAh g^{-1}) and the best Coulombic efficiency (95.2%) at the first cycle.

Table 2.2 Charge/discharge capacities at the first cycle of the galvanostatic measurements for the hard carbon electrodes at a current density of 20 mA g^{-1}.

Sample	First charge Capacity / mAh g^{-1}	First discharge Capacity / mAh g^{-1}	Coulombic efficiency for the 1st cycle / %
HC-1000	326	284	87.2
HC-1200	376	344	91.5
HC-1400	365	348	95.2
HC-1600	299	273	91.3
HC-1800	254	223	88.0
HC-1900	176	147	83.3

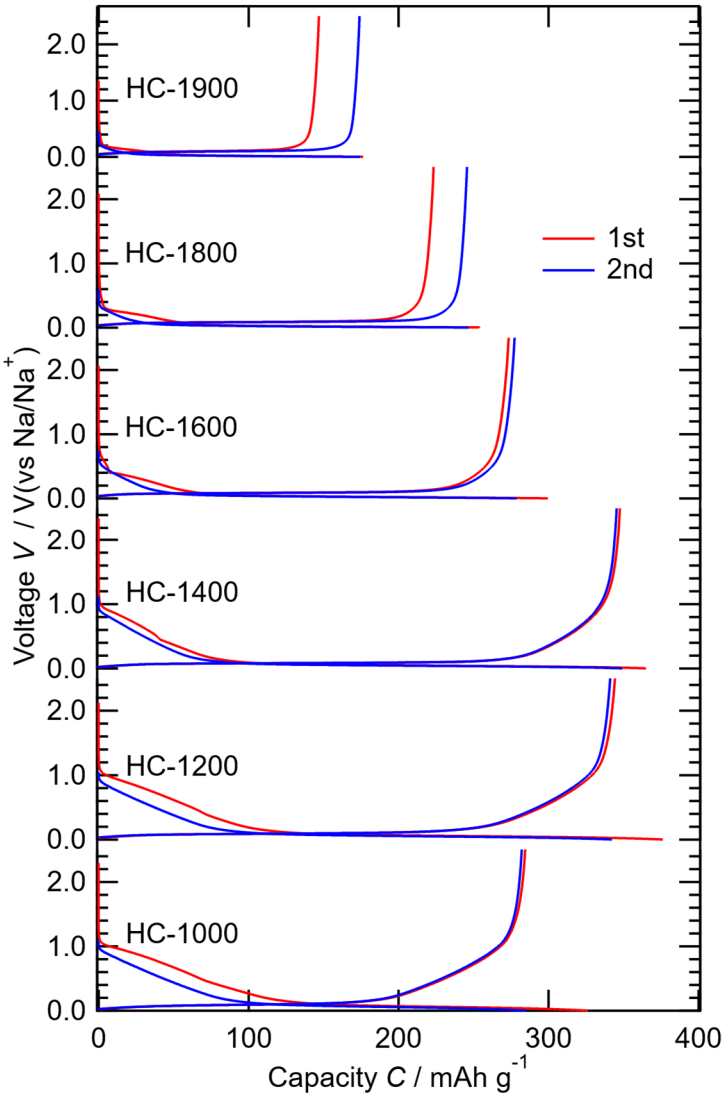

Figure 2.9 Galvanostatic charge-discharge curves of the hard carbons with various carbonization temperatures at a current density of 20 mA g^{-1}.

2.5 Conclusion

By optimizing the raw material and synthesis conditions of hard carbon, high reversible capacity (348 mAh g^{-1}) and extremely high initial Coulombic efficiency (95.2%) were achieved, as shown in **Figure 2.10**. This is the first report that the performance of hard carbon can be improved by mixing multiple types of sugars. Since there are many types of saccharides other than the three types used in this chapter, the number of potential combinations is enormous. Therefore, it is desirable to investigate raw material combinations that enable even higher performance.

A high ICE makes it possible to observe only changes related to the storage of sodium, and a large capacity indicates that the storage site is being used efficiently. Using the hard carbon synthesized in this chapter, the author investigated the sodium storage mechanism, and this is presented in Chapter 3.

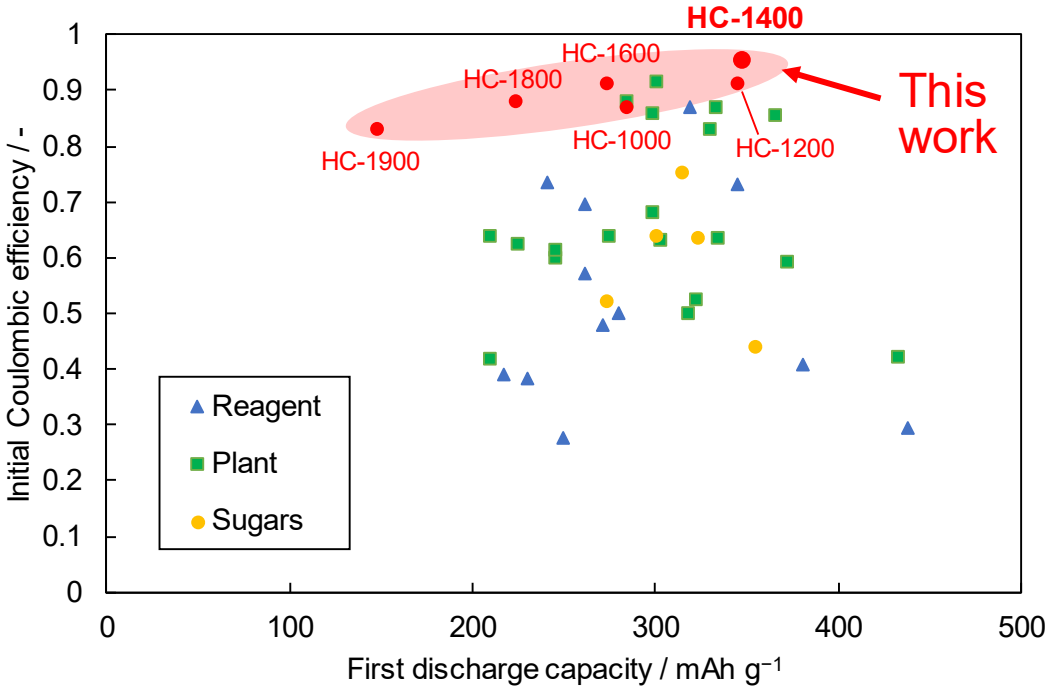

Figure 2.10 Cell performance of hard carbons reported in the past and synthesized in this study.

References

1. Zhang, Y., Meng, Y., Chen, L., Guo, Y. & Xiao, D. High lithium and sodium anodic performance of nitrogen-rich ordered mesoporous carbon derived from alfalfa leaves by a ball-milling assisted template method. *J. Mater. Chem. A* **4**, 17491–17502 (2016).
2. Liu, H. *et al.* Nitrogen-doped carbon/graphene hybrid anode material for sodium-ion batteries with excellent rate capability. *J. Power Sources* **319**, 195–201 (2016).
3. Wu, L., Buchholz, D., Vaalma, C., Giffin, G. A. & Passerini, S. Apple-Biowaste-Derived Hard Carbon as a Powerful Anode Material for Na-Ion Batteries. *ChemElectroChem* **3**, 292–298 (2016).
4. Dahbi, M. *et al.* Synthesis of hard carbon from argan shells for Na-ion batteries. *J. Mater. Chem. A* **5**, 9917–9928 (2017).
5. Qiu, S. *et al.* Manipulating Adsorption-Insertion Mechanisms in Nanostructured Carbon Materials for High-Efficiency Sodium Ion Storage. *Adv. Energy Mater.* **7**, 1700403 (2017).
6. Simone, V. *et al.* Hard carbon derived from cellulose as anode for sodium ion batteries: Dependence of electrochemical properties on structure. *J. Energy Chem.* **25**, 761–768 (2016).
7. Liu, P. *et al.* A waste biomass derived hard carbon as a high-performance anode material for sodium-ion batteries. *J. Mater. Chem. A* **4**, 13046–13052 (2016).
8. Qin, D. *et al.* Analogous graphite carbon sheets derived from corn stalks as high performance sodium-ion battery anodes. *RSC Adv.* **6**, 106218–106224 (2016).
9. Väli, R., Jänes, A., Thomberg, T. & Lust, E. D-Glucose Derived Nanospheric Hard Carbon Electrodes for Room-Temperature Sodium-Ion Batteries. *J. Electrochem. Soc.* **163**, A1619–A1626 (2016).
10. Wang, C. *et al.* Controlling pseudographtic domain dimension of dandelion derived biomass carbon for excellent sodium-ion storage. *J. Power Sources* **358**, 85–92 (2017).
11. Zheng, P. *et al.* Enhanced Performance by Enlarged Nano-pores of Holly Leaf-derived Lamellar Carbon for Sodium-ion Battery Anode. *Sci. Rep.* **6**, 26246 (2016).
12. Wang, P. *et al.* Kelp-derived hard carbons as advanced anode materials for sodium-ion batteries. *J. Mater. Chem. A* **5**, 5761–5769 (2017).
13. Zhu, Y., Chen, M., Li, Q., Yuan, C. & Wang, C. High-yield humic acid-based hard carbons as promising anode materials for sodium-ion batteries. *Carbon N. Y.* **123**, 727–734 (2017).
14. Chen, Y. *et al.* Self-assembly of 3D neat porous carbon aerogels with NaCl as template and flux for sodium-ion batteries. *J. Power Sources* **359**, 529–538 (2017).
15. Zheng, Y., Wang, Y., Lu, Y., Hu, Y.-S. & Li, J. A high-performance sodium-ion battery enhanced by macadamia shell derived hard carbon anode. *Nano Energy* **39**, 489–498 (2017).
16. Wang, K. *et al.* Low-Cost and High-Performance Hard Carbon Anode Materials for

Sodium-Ion Batteries. *ACS Omega* **2**, 1687–1695 (2017).

17. Xiang, J., Lv, W., Mu, C., Zhao, J. & Wang, B. Activated hard carbon from orange peel for lithium/sodium ion battery anode with long cycle life. *J. Alloys Compd.* **701**, 870–874 (2017).
18. Dou, X. *et al.* Pectin, Hemicellulose, or Lignin? Impact of the Biowaste Source on the Performance of Hard Carbons for Sodium-Ion Batteries. *ChemSusChem* **10**, 2668–2676 (2017).
19. Zhang, T. *et al.* Pinecone biomass-derived hard carbon anodes for high-performance sodium-ion batteries. *RSC Adv.* **7**, 41504–41511 (2017).
20. Li, Y. *et al.* Pitch-derived amorphous carbon as high performance anode for sodium-ion batteries. *Energy Storage Mater.* **2**, 139–145 (2016).
21. Zhao, P.-Y. *et al.* High-Performance Anode of Sodium Ion Battery from Polyacrylonitrile/Humic Acid Composite Electrospun Carbon Fibers. *Electrochim. Acta* **232**, 348–356 (2017).
22. Zhang, B. *et al.* Laser Synthesis of Hard Carbon for Anodes in Na-Ion Battery. *Adv. Mater. Technol.* **2**, 1600227 (2017).
23. Zhang, B., Ghimbeu, C. M., Laberty, C., Vix-Guterl, C. & Tarascon, J.-M. Correlation Between Microstructure and Na Storage Behavior in Hard Carbon. *Adv. Energy Mater.* **6**, 1501588 (2016).
24. Xiao, L. *et al.* Hard carbon nanoparticles as high-capacity, high-stability anodic materials for Na-ion batteries. *Nano Energy* **19**, 279–288 (2016).
25. Hu, M. *et al.* Enhanced sodium-ion storage of nitrogen-rich hard carbon by NaCl intercalation. *Carbon N. Y.* **122**, 680–686 (2017).
26. Bai, Y. *et al.* Mille-feuille shaped hard carbons derived from polyvinylpyrrolidone via environmentally friendly electrostatic spinning for sodium ion battery anodes. *RSC Adv.* **7**, 5519–5527 (2017).
27. Cao, L. *et al.* Rape seed shuck derived-lamellar hard carbon as anodes for sodium-ion batteries. *J. Alloys Compd.* **695**, 632–637 (2017).
28. Hu, H. *et al.* Carbon nanosheet frameworks derived from sodium alginate as anode materials for sodium-ion batteries. *Mater. Lett.* **185**, 530–533 (2016).
29. Keller, M., Vaalma, C., Buchholz, D. & Passerini, S. Development and Characterization of High-Performance Sodium-Ion Cells based on Layered Oxide and Hard Carbon. *ChemElectroChem* **3**, 1030 (2016).
30. Morita, R. *et al.* Combination of solid state NMR and DFT calculation to elucidate the state of sodium in hard carbon electrodes. *J. Mater. Chem. A* **4**, 13183–13193 (2016).
31. Yin, L. *et al.* Self-assembly of disordered hard carbon/graphene hybrid for sodium-ion batteries. *J. Power Sources* **305**, 156–160 (2016).
32. Jian, Z., Xing, Z., Bommier, C., Li, Z. & Ji, X. Hard Carbon Microspheres: Potassium-Ion

Anode Versus Sodium-Ion Anode. *Adv. Energy Mater.* **6**, 1501874 (2016).

33. Zhang, H., Ming, H., Zhang, W., Cao, G. & Yang, Y. Coupled Carbonization Strategy toward Advanced Hard Carbon for High-Energy Sodium-Ion Battery. *ACS Appl. Mater. Interfaces* **9**, 23766–23774 (2017).
34. Zhang, F. *et al.* High Temperature Carbonized Grass as a High Performance Sodium Ion Battery Anode. *ACS Appl. Mater. Interfaces* **9**, 391–397 (2017).
35. Ye, J., Zang, J., Tian, Z., Zheng, M. & Dong, Q. Sulfur and nitrogen co-doped hollow carbon spheres for sodium-ion batteries with superior cyclic and rate performance. *J. Mater. Chem. A* **4**, 13223–13227 (2016).
36. Li, Y. *et al.* Tire-derived carbon composite anodes for sodium-ion batteries. *J. Power Sources* **316**, 232–238 (2016).
37. Zhu, X. *et al.* Hard Carbon Fibers Pyrolyzed from Wool as High-Performance Anode for Sodium-Ion Batteries. *JOM* **68**, 2579–2584 (2016).
38. Liu, H. *et al.* A floral variant of mesoporous carbon as an anode material for high performance sodium and lithium ion batteries. *RSC Adv.* **6**, 78235–78240 (2016).
39. Wang, Q., Li, H., Chen, L. & Huang, X. Monodispersed hard carbon spherules with uniform nanopores. *Carbon N. Y.* **39**, 2211–2214 (2001).
40. Qi, Y., Zhang, M., Qi, L. & Qi, Y. Mechanism for the formation and growth of carbonaceous spheres from sucrose by hydrothermal carbonization. *RSC Adv.* **6**, 20814–20823 (2016).
41. Zha, G. & Yu, L. Influence of sucrose solution's pH on hydrothermally synthesized carbon microspheres. *Fullerenes, Nanotub. Carbon Nanostructures* **24**, 139–143 (2016).
42. Yamamoto, H. *et al.* Synthesizing higher-capacity hard-carbons from cellulose for Na- and K-ion batteries. *J. Mater. Chem. A* **6**, 16844–16848 (2018).
43. Tokumitsu, K. Structural characterization and electrochemical properties of non-graphitizable carbons for a lithium ion battery. *J. Power Sources* **90**, 206–213 (2000).

3 Mechanism of sodium storage in hard carbon

3.1 Introduction

Hard carbon is a disordered carbonaceous compound and a standard anode material for NIBs because of its large reversible capacity at low operating voltages, as well as its good cycling stability.[1–5] Although many researchers have attempted to analyze the mechanism of sodium storage in hard carbons, it remains a matter of controversy, primarily because of the diversity in the carbon microstructure, absence of crystallinity, and extreme reactivity of the sodiated hard carbon. Therefore, to obtain a comprehensive understanding of the sodiation process in hard carbons, careful experimental approaches are necessary to clarify the local environment while avoiding side reactions under atmospheric conditions.

A typical charge–discharge curve of hard carbon can be divided into a sloping region at high potentials (ca. 0.1–2.5 V versus Na/Na^+) and a plateau at low potentials (ca. 0–0.1 V versus Na/Na^+). Stevens and Dahn first assigned the high-potential region to the intercalation of sodium into the graphene interlayers and the low-potential region to sodium insertion in the nanopores.[6] In addition, previous computational studies have suggested that the edge and defect sites on the carbon surface allow sodium to be adsorbed in the high-potential region.[7–11] The present generally accepted view is that hard carbon involves three types of storage sites: 1) the defects and edges on the graphene, 2) graphene–graphene interlayers, and 3) nanopores. However, the assignment of the aforementioned three storage mechanisms to the charge–discharge voltage profile is still controversial. For example, Liu *et al.* and Cao *et al.* attributed the plateau region to sodium intercalation into the graphene–graphene interlayers,[12,13] whereas Tarascon *et al.* observed a constant interlayer distance upon sodiation at the plateau, suggesting no intercalation in the graphitic domains.[14,15] Concerning the analysis of sodium insertion into nanopores, most research groups have tried to use the pore size distribution, as measured by gas absorption techniques, of the pristine hard carbon. However, such gas sorption experiments cannot be applied to the sodium

inserted electrodes, and the technique is not sensitive to the closed pores (the pores inaccessible to any adsorbent including helium),[16,17] which play a crucial role, as discussed by Kano *et al.* and Zhang *et al*.. They reported that the capacity of the plateau region is correlated with the closed pore volume rather than the open pore volume.[18–20]

To gain an overall understanding that describes both interlayer and nanopore storage, I have conducted a complementary *ex situ* small and wide-angle X-ray scattering (SAXS and WAXS, respectively) study on carefully prepared (transferred under a strictly inert atmosphere) hard carbons having various microstructures and various extent of sodium intercalations. In this chapter, I demonstrate not only the rational relationship between the nanostructures and Na^+ insertion voltage profile but also a new characteristic scattering peak in the WAXS profile that represent the atomic correlation of Na in the nanopores.

3.2 Experimental and computational methods

3.2.1 Material synthesis

The whole process of the synthesis is shown in **Figure 3.1**. A hard carbon precursor was prepared by the hydrothermal treatment of sucrose.[21] Sucrose (Wako Chemical) was used without further purification. Sucrose (42.8 g, 0.125 mol) was dissolved in deionized water (50 mL) and transferred into a polytetrafluoroethylene-lined stainless-steel autoclave. The hydrothermal treatment was carried out at 200 °C for 5 h. The resultant powder was washed several times with deionized water and dried overnight in an oven at 60 °C. The dried powder was carbonized at 1000 °C for 5 h under Ar flow. The heating rates were 1 °C min^{-1} below 500 °C and 5 °C min^{-1} above 500 °C. The obtained hard carbon was pulverized by planetary ball-milling (Pulverisette 6, Fritsch) for 2 h at 200 rpm. The milled hard carbon was divided into seven portions, and they were treated at high temperature (T = 1000, 1200, 1400, 1600, 1800, 1900, and 2000 °C) in a high-frequency induction heating furnace (MU-αIII, SK Medical Electronics Co., Ltd.) for 1 h under Ar flow.

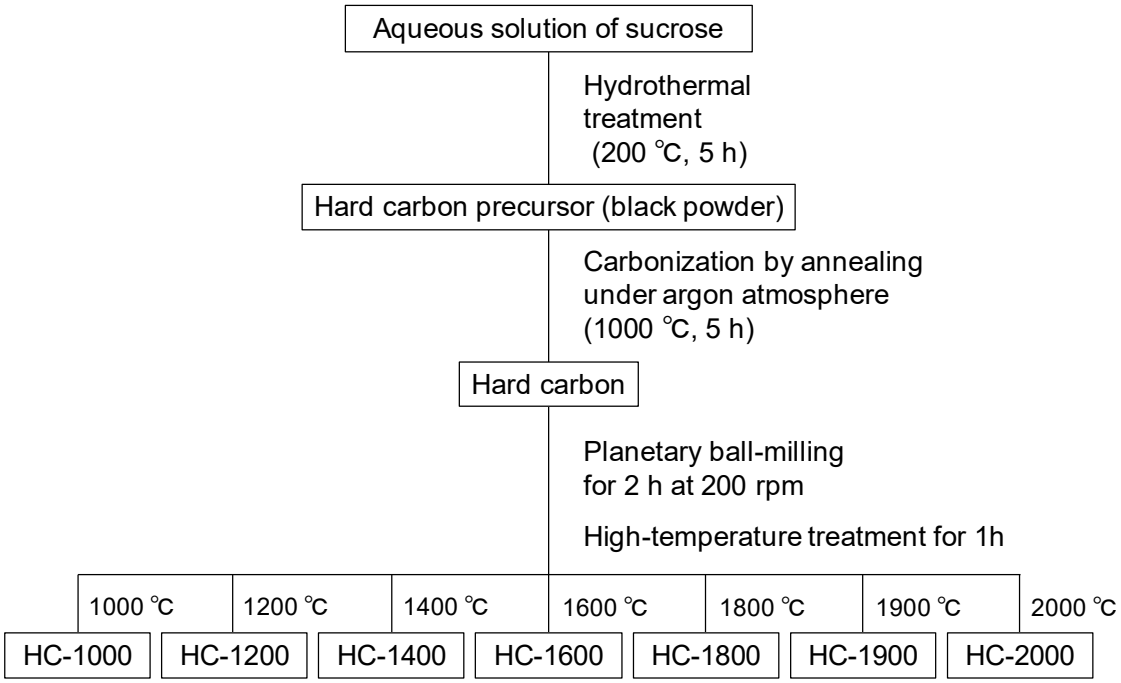

Figure 3.1 Process of the synthesis for hard carbon samples.

3.2.2 Electrochemical tests

A slurry was prepared by mixing the synthesized hard carbon samples and carboxymethyl cellulose (CMC2200, Daicel) in a weight ratio of 9:1 in deionized water. The obtained slurry was coated on Cu foil. The electrodes were punched into disks with a diameter of 12 mm. The loading mass of the electrodes was approximately 1.5–1.7 mg cm^{-2}. The electrochemical measurements were conducted using 2032-type coin cells. The electrolyte was 1 mol dm^{-3} $NaPF_6$ in ethyl carbonate (EC)/diethyl carbonate (DEC) (1:1 by volume, Kishida Chemical), the separator was a glass fiber filter (GB-50, Advantec), and the counter electrode was Na metal. These cells were assembled inside an Ar-filled glove box (Miwa Inc., Japan). Galvanostatic charge–discharge tests were carried out in the voltage range of 0–2.5 V vs. Na/Na^+ at a current density of 20 mA g^{-1} using charge–discharge units (TOSCAT 3100, Toyo System Co.). For galvanostatic intermittent titration technique (GITT), the cells were charged/discharged at 10 mA g^{-1} of current pulses with 2 h intervals using charge-

discharge units (HJ1001SD8, Hokuto Denko Corporation). GITT tests were performed after one cycle of charging/discharging, and the pulse duration was 30, 30, and 24 minutes with HC-1000, HC-1400, and HC-1900, respectively. Electrochemical impedance spectroscopy (EIS) measurements were performed in three-electrode cells with Na metal as counter/reference electrode. The EIS tests were conducted using Solartron (1470E, Solartron Analytical) in the frequency range of 1 MHz to 10 mHz with AC amplitude of 10 mV.

3.2.3 *Ex situ* analysis

The cells were charged to the desired voltage points at a current density of 10 mA g^{-1} after 1 cycle. The cells that had reached the desired cutoff voltage were disassembled in an Ar-filled glove box. The electrodes were washed with dimethyl carbonate (DMC, Kishida) and samples were loaded into borosilicate glass capillaries. DMC was used after removing moisture by molecular sieve 4 Å (Wako Chemical). The capillary was completely sealed with epoxy adhesive to avoid air exposure of the sample during measurement. The SAXS profiles were recorded in the range of 0.0043 $Å^{-1} \leq q \leq 0.57$ $Å^{-1}$ using a SmartLab (Rigaku) with Cu *Kα* radiation. WAXS measurements were carried out using Macro7HFM-AXISVII (Rigaku) and scattering data were collected with a two-dimensional detector. For semi-quantitative analysis, the obtained WAXS patterns were fitted using the pseudo-Voigt function. Details of the fitting procedures are provided in Appendix A.

Throughout these analyses, care was taken to prevent sample degradation. The borosilicate glass capillaries sealed with epoxy glue worked well to maintain the sample in an inert environment in most cases. However, when the sample atmosphere in the container was not strictly sealed, decomposition products, mainly sodium carbonates, were detected in the WAXS patterns.

3.2.4 DFT calculations

DFT-MD calculations were performed with the Vienna ab initio simulation package (VASP, ver.

5.4.1).[22] The projector augmented wave (PAW) method as implemented in VASP was employed.[23,24] The temperature was set at 300 K using the Nosé–Hoover thermostat.[25,26] An energy cutoff of 300 eV was used for the plane-wave basis, and a 1 × 1 × 1 Monkhorst–Pack k-point mesh was applied. A sufficient vacuum separation of 12 Å was used for all calculations. For the initial structure, a series of previously reported stable sodium cluster structures were used.[27] The MD simulations were performed for 5 ps using a time step of 1 fs after equilibration for 1.1 ps. The scattering intensity profile was obtained by summing the time series of the scattering intensity calculated for the real-space structures using the Debye scattering equation.[28,29]

3.3 Structural characterization of synthesized hard carbons

In our systematic analysis of the Na storage mechanism, I prepared a series of hard carbon samples via the hydrothermal treatment of sucrose and subsequent high-temperature carbonization at temperatures (*T*) from 1000 to 2000 °C as described in Chapter 2.4. The prepared products are denoted HC-*T*. To eliminate microstructural differences between batches and investigate only the changes due to heat treatment, hydrothermally treated precursors of the same batch was divided and carbonized at different temperatures. All the products have an identical spherical morphology having diameters of 2–10 μm, as shown in the secondary electron micrographs in **Figure 3.2**. Thus, the range of experimental results obtained can be attributed to the differences in the microstructures and atomistic structures of the particles.

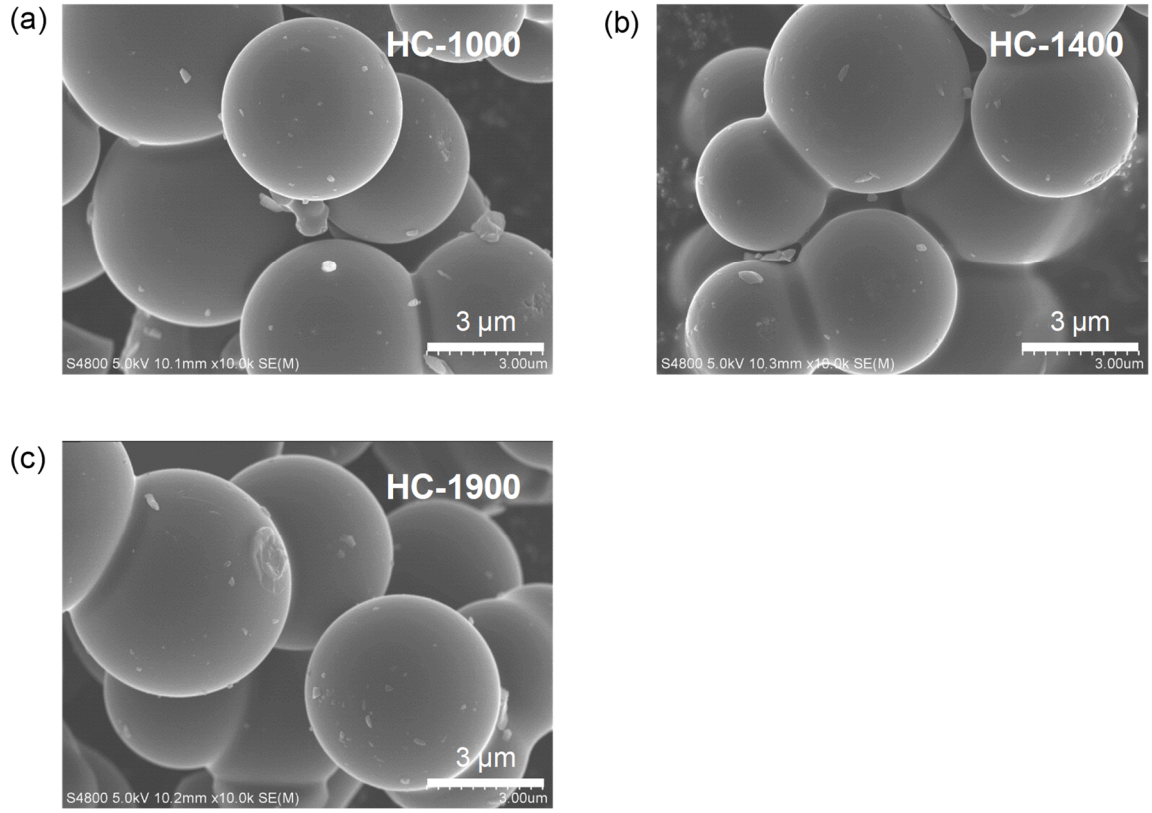

Figure 3.2 Secondary electron micrographs of (a) HC-1000, (b) HC-1400, and (c) HC-1900 collected with a field-emission scanning electron microscope.

The WAXS profiles of the as-prepared hard carbons (**Figure 3.3**) show characteristic broad peaks located around 2θ = 23–25° and 43.3–43.7°. The structure of hard carbon is generally described as an aggregate of disordered graphitic domains with many interconnections.[30–34] Thus, the former peak (23–25°) corresponds to the interlayer and the latter (43.3–43.7°) to the in-plane atomic correlations of the graphene sheets in the graphitic domain. As the carbonization temperature increased, the former peak (23–25°) shifted to higher angles and the peaks became sharper. The latter peaks (43.3–43.7°) also sharpened but their positions shifted to lower angles. The graphene–graphene interlayer distances (d) are summarized in **Table 3.1** and **Figure 3.4**, where the higher-temperature treatment causes a monotonic decrease of the interlayer distance. Although the sharpening of the broad peaks indicates an increase in crystallinity, the samples remained amorphous. Exceptionally, HC-2000 contains a crystallized graphite phase as a minor constituent,

as shown by the sharp Bragg reflection at $2\theta \approx 25.9°$. Overall, the progressive structural transformations from an amorphous glass-like state to crystalline graphite is slow below 2000 °C.

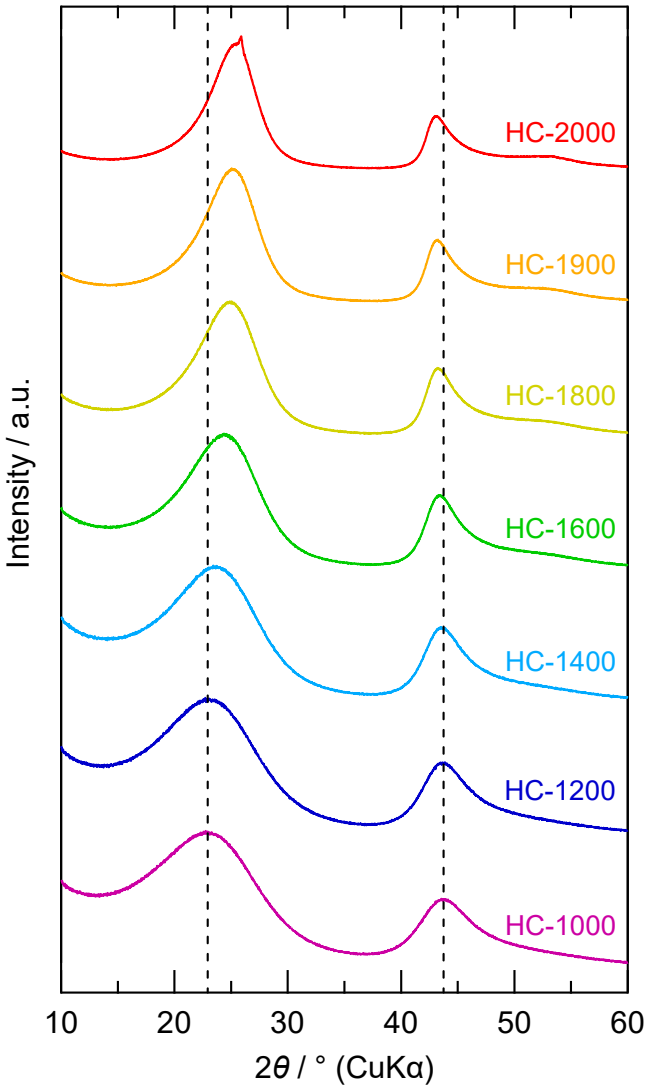

Figure 3.3 WAXS patterns of synthesized hard carbons.

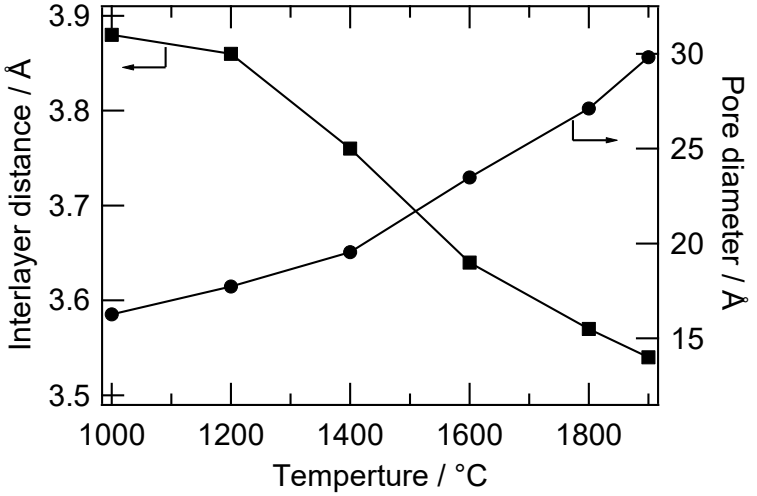

Figure 3.4 Plots of derived interlayer distance and pore diameters versus the final thermal treatment temperature.

Figure 3.5 shows the SAXS profiles of pristine hard carbons synthesized at various temperatures. The horizontal axis is the scattering vector (q), which is defined as

$$q = \frac{4\pi \sin\theta}{\lambda}, \tag{3.1}$$

where θ is half the scattering angle and λ is the wavelength of the incident X-ray (Cu Kα, λ = 1.5418 Å). All the SAXS profiles contained shoulder-shaped scattering peaks at ca. 0.1–0.3 $Å^{-1}$ in addition to the monotonic decay with increasing q. The peak around $q \approx 0.2$ $Å^{-1}$ corresponds to nanometer-sized structures and can be attributed to the nanopores in the hard carbon matrix.[2,6] The peaks at low q values originate from larger-scale microstructures such as meso/macropores and particles. With increasing heat treatment temperature, the nanopore scattering became more intense and the reflections shifted to the low-q region.

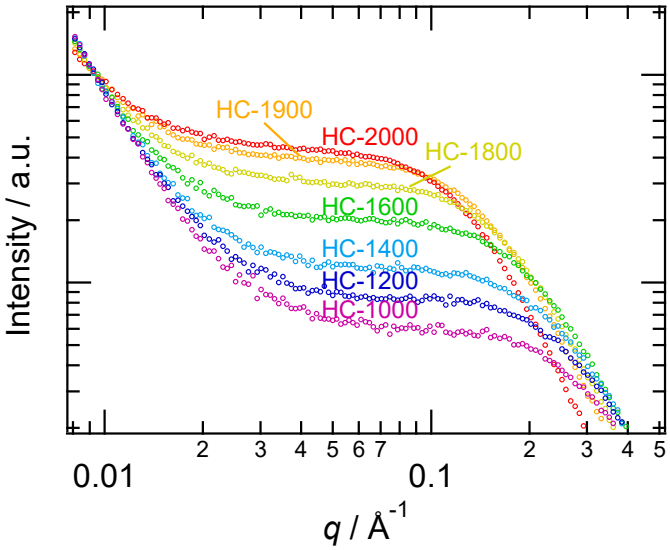

Figure 3.5 SAXS profiles of synthesized hard carbons.

On the basis of the Guinier plot and its analysis (**Figure 3.6**),[35–37] the average pore diameter continuously increased as a function of the heat-treatment temperature (Figure 3.4), which is consistent with the results of previous reports.[38–41]

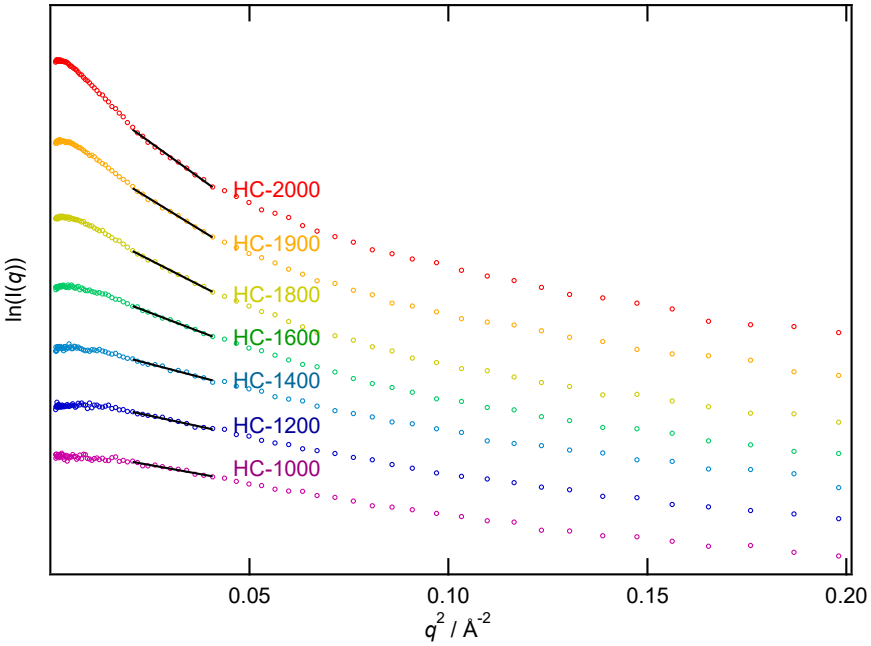

Figure 3.6 Guinier plots generated from SAXS profiles of hard carbons treated at various temperatures. The contribution of larger-scale microstructures is subtracted as a background, and linear regression analysis was applied in the range of q^2 = 0.021–0.041 Å^{-2}.

Raman spectra of synthesized hard carbons are shown in **Figure 3.7**. All the spectra have two characteristic peaks around 1340 and 1590 cm^{-1}, corresponding to D-band (disorder- and defect-related mode) and G-band (the crystalline graphite mode), respectively.[42–44] The D-band indicates that defects and disordered structures are existing in all the hard carbons. As listed in Table 3.1, the integrated intensity ratio of the D-band to the G-band (A_D/A_G) decreases with the preparation temperature, suggesting that the reduction of defect concentration with the progress of graphitization as reported previously. [39–41,45]

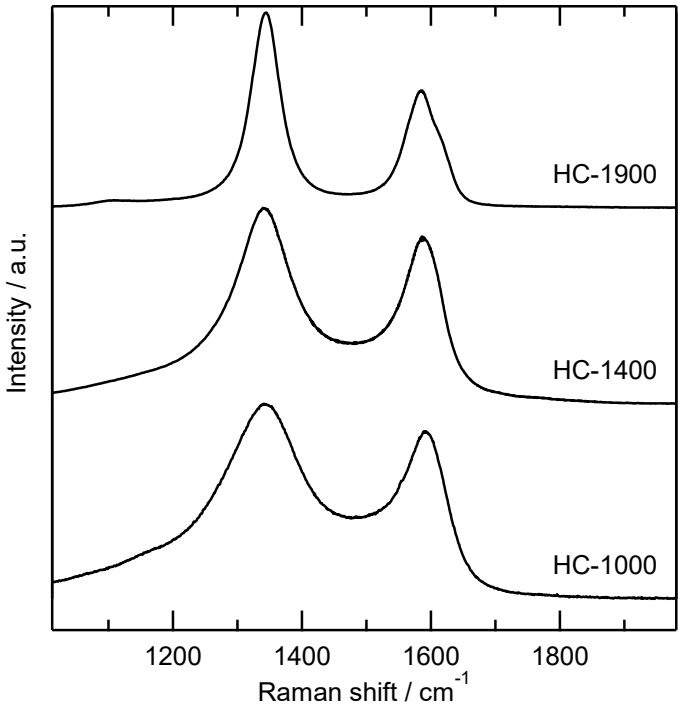

Figure 3.7 Raman spectra of synthesized hard carbons.

Brunauer–Emmett–Teller (BET) surface area were measured for three types of hard carbons (HC-1000, HC-1400, and HC-1900) by N_2 adsorption-desorption measurements (**Figure 3.8**). X-ray photoelectron spectroscopy (XPS) spectra were also measured for the same samples (**Figure 3.9**), and the results are summarized in **Table 3.1**. The decreasing BET surface area and increasing carbon content with heating are also consistent with previous reports.[39–41,45]

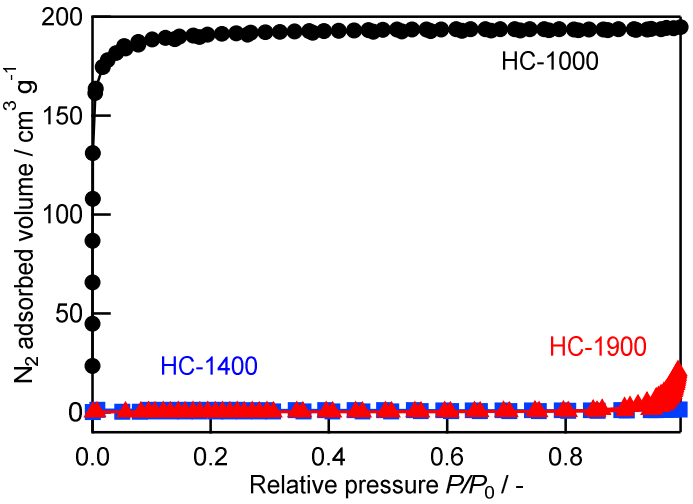

Figure 3.8 N_2 adsorption-desorption isothermal curves of hard carbons.

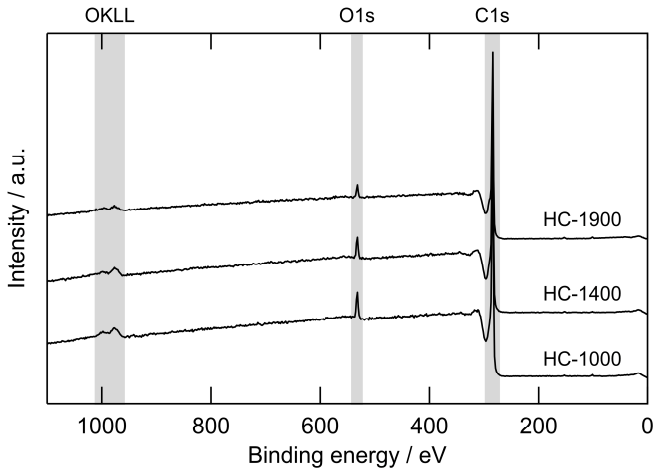

Figure 3.9 Wide-scan XPS spectra of synthesized hard carbons.

Table 3.1 Physical parameters of hard carbon samples.

Sample	Interlayer distance d / Å	Pore diameter / Å	A_D/A_G	Surface area / $m^2\ g^{-1}$	Surface atomic ratio / %	
					C	O
HC-1000	3.88	16.3	4.55	297.7	95.2	4.8
HC-1200	3.86	17.7	-	-	-	-
HC-1400	3.76	19.5	2.13	2.2	96.3	3.7
HC-1600	3.64	23.5	-	-	-	-
HC-1800	3.57	27.1	-	-	-	-
HC-1900	3.54	29.8	1.62	0.8	97.7	2.3
HC-2000	-	32.3	-	-	-	-

3.4 Electrochemical properties of hard carbons

The electrochemical measurements were conducted using half-cells to evaluate the Na storage properties. **Figure 3.10**(a) shows the galvanostatic charge–discharge curves measured at 20 mA g^{-1} and the corresponding differential capacity dQ/dV profiles versus the cell voltage, V. Here I divide the storage capacity into a sloping region (> 0.1 V, Q_{slope}) and a plateau region (≤ 0.1 V, $Q_{plateau}$). As the carbonization temperature was increased, Q_{slope} decreased and $Q_{plateau}$ became dominant (**Figure 3.11**). As mentioned in section 2.4, HC-1400 showed the highest discharge capacity (348 mAh g^{-1}) and the best Coulombic efficiency (95.2%) at the first cycle among all the samples. On the basis of the peak separations of the dQ/dV profiles (Figure 3.10(b)), the cell polarizations were larger for the higher preparation temperatures. The Nyquist plots of the alternative current (AC) impedance for the hard carbon electrodes also showed higher resistance for the higher-T-treated electrodes (Figure 3.10(c)). Based on these electrochemical properties, I selected three hard carbons, HC-1000, HC-1400, and HC-1900, for analysis to understand the overall Na storage mechanism in detail.

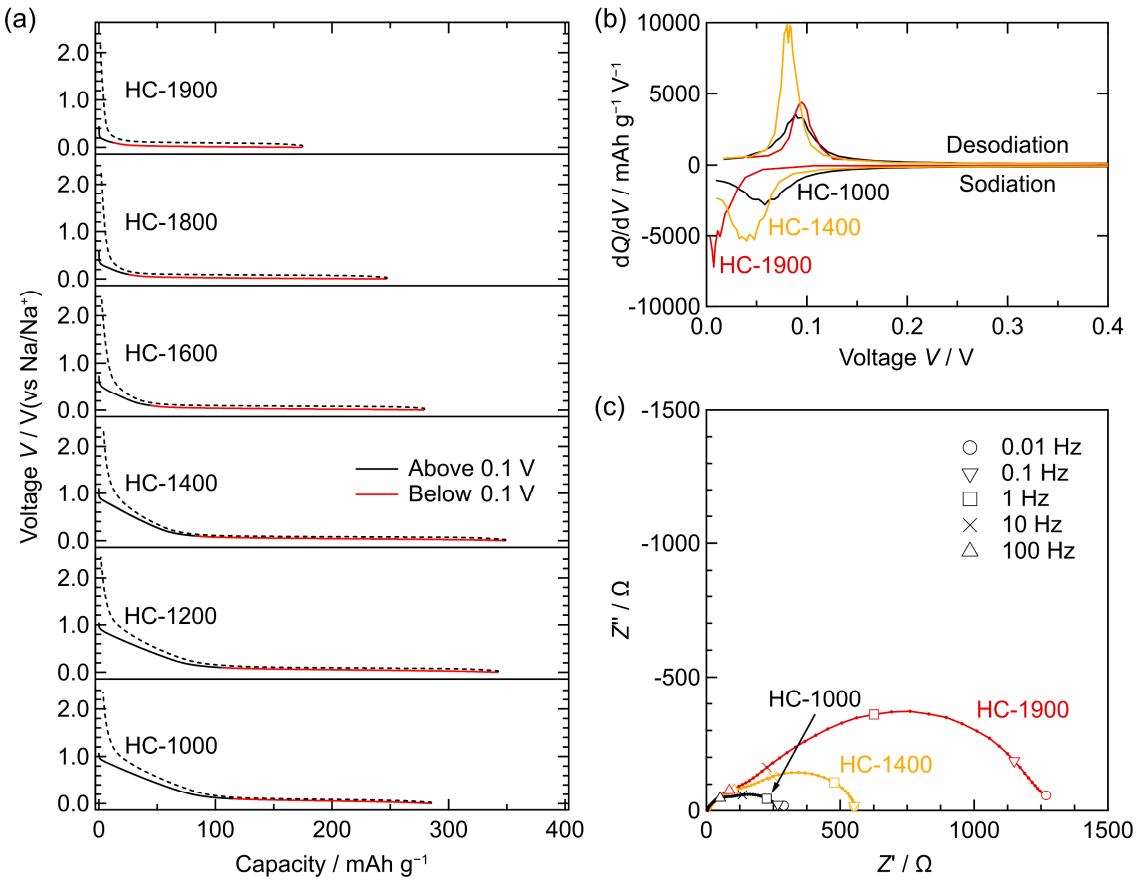

Figure 3.10 (a) Galvanostatic charge–discharge curves of the hard carbons with varied carbonization temperatures at a current density of 20 mA g^{-1} and (b) corresponding differential galvanostatic profile dQ/dV. (c) Nyquist plots of the AC impedance for the hard carbon electrodes at 0.01 V versus Na/Na^+. The small semicircles in the high frequency region can be assigned to the SEI, and the other one represents the charge transfer resistance at the active material/electrolyte interface.[46,47]

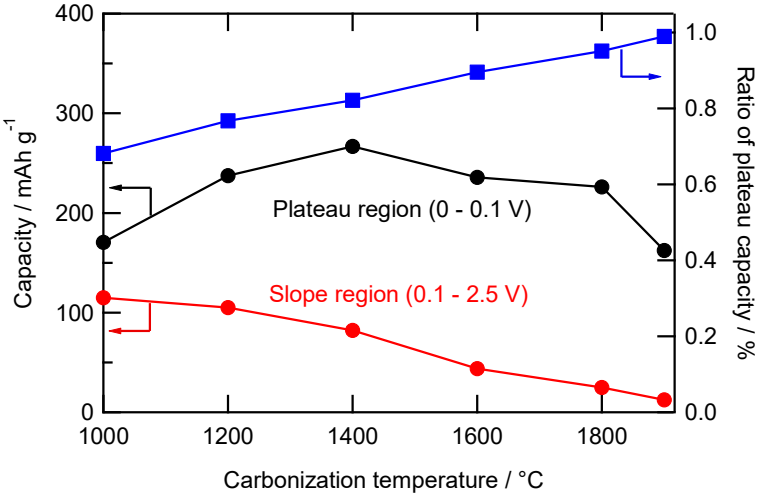

Figure 3.11 Capacity of each region and ratio of plateau capacity as a function of carbonization temperature. The charge-discharge curve was divided into the sloping region (> 0.1 V) and the plateau region (< 0.1 V). The ratio of plateau capacity was defined as Q_{plateau} / [overall capacity].

3.5 *Ex situ* analyses of Na-inserted samples

For structural analysis of the sodiated hard carbons, *ex situ* SAXS and WAXS measurements were conducted. To minimize the influence of resistance, charging and discharging was performed at a small current density of 10 mA g^{-1} when preparing samples for the analyses. Note that the electrodes are “extremely” sensitive to moisture, CO_2, and O_2, especially in the highly sodiated state. Such atmospheric sensitivity might be a critical reason for the contradictory findings of previous works on the hard carbon electrodes. Therefore, I prepared the sodiated electrodes for *ex situ* SAXS/WAXS with great care to ensure no sample degradation.

The different degrees of sodiation chosen for analysis are shown in **Figure 3.12**, along with the voltage profiles upon galvanostatic sodiation at 10 mA g^{-1}, and the results are listed in **Table 3.2**. For the sake of comparison, I define the "Na insertion percentage" as f_{Na}, where the starting point of sodiation is 0% and the point where the cell voltage reached 0 V is 100%. To distinguish between inserted and electrodeposited sodium, I collected data for a few additional points beyond 100%. As hard carbon sodiated to below 0 V (vs. Na/Na^+), it is known that the charge-discharge curve shows a "V" shape corresponding to the nucleation of sodium metal.[15,48,49] The insets in Figure 3.12 shows

the voltage profiles in the vicinity of the starting point of sodium electrodeposition.

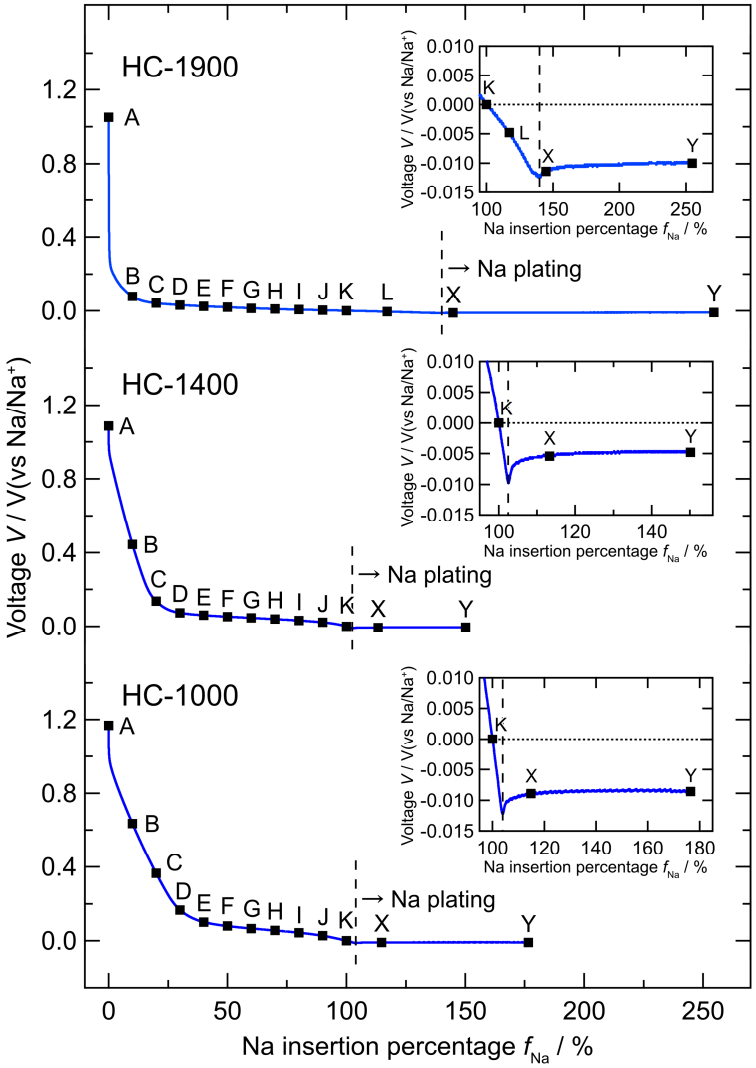

Figure 3.12 Charge curves at the 2nd cycle of the three hard carbon samples. The state of charge of each sample used for *ex situ* measurement is plotted on the curve. The inset is an enlarged view around 0 V.

Table 3.2 The states of charge for *ex-situ* samples.

	SOC / %	Voltage / V		
		HC-1000	HC-1400	HC-1900
A	0	1.165	1.114	1.007
B	10	0.620	0.437	0.073
C	20	0.343	0.135	0.038
D	30	0.156	0.072	0.028
E	40	0.100	0.059	0.022
F	50	0.081	0.051	0.017
G	60	0.070	0.043	0.012
H	70	0.060	0.037	0.009
I	80	0.048	0.029	0.006
J	90	0.030	0.020	0.003
K	100	0	0	0
L	117	-	-	-0.005
X	*	-0.009	-0.005	-0.011
Y	*	-0.009	-0.005	-0.010

* Depends on the sample

Figure 3.13(a)–(c) show a series of *ex situ* WAXS patterns after sodiation. Here, I first focus on the broad peak at $q \approx 1.6$–1.8 Å^{-1}, which corresponds to the atomic correlation relating to the graphene–graphene interlayer distance. In HC-1000, the broad peaks shifted toward lower q as the sodiation proceeded and returned to their initial positions when the samples were desodiated. Therefore, the shifts can be attributed to reversible sodium insertions to the interlayer space in the graphitic domains.[2,50]

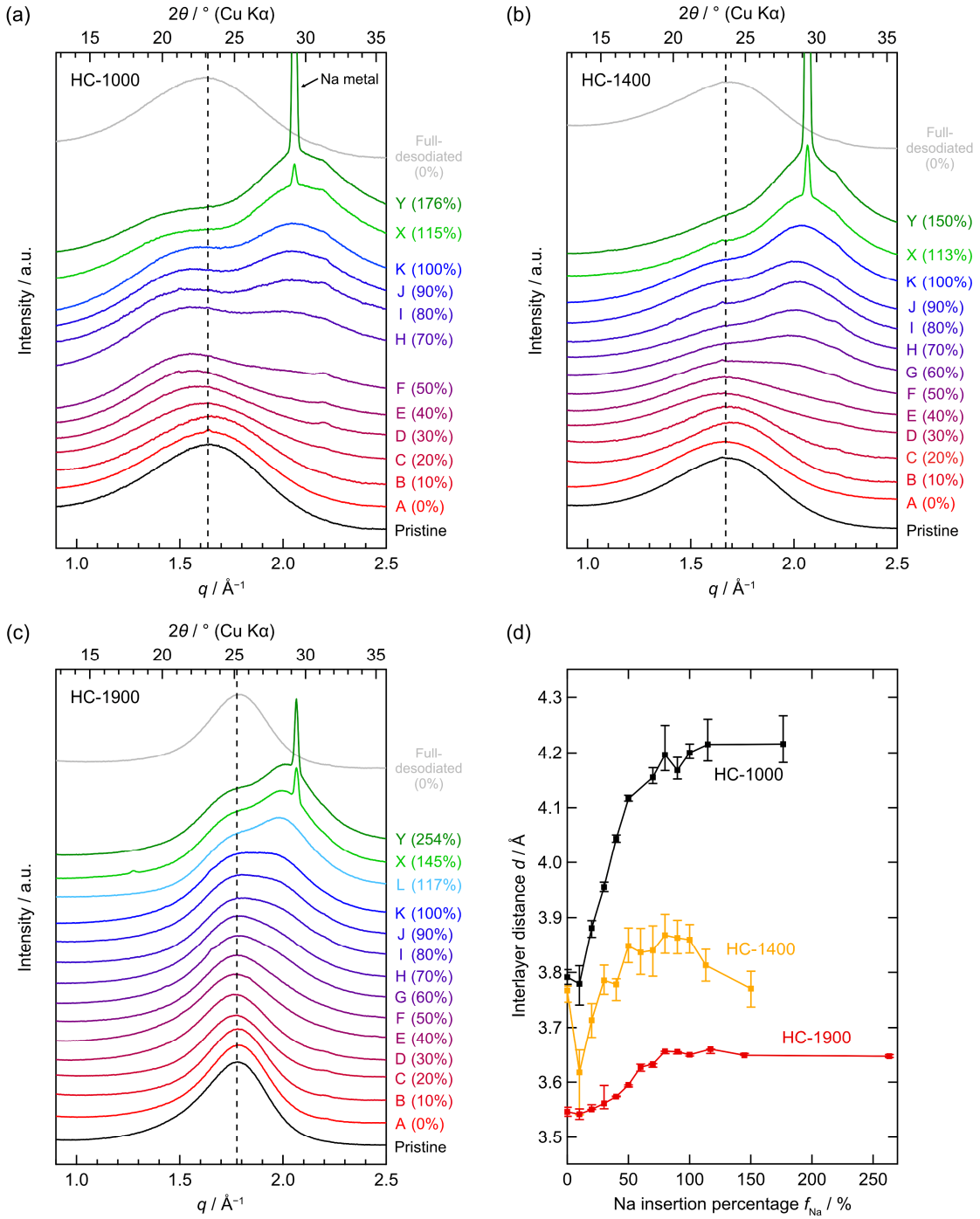

Figure 3.13 *Ex situ* WAXS patterns of hard carbon electrodes: (a) HC-1000, (b) HC-1400, and (c) HC-1900. (d) Average interlayer distance upon sodiation derived from deconvolution analyses of the WAXS patterns. Numbers in parentheses mean sodium insertion percentage f_{Na}.

Notably, a new broad peak appeared at $q \approx 2.0$–2.1 Å^{-1} in all the hard carbon samples when f_{Na} exceeded 50–60%, and this peak became more pronounced upon further sodiation. The appearance

of the broad peak at $q \approx 2.0$–2.1 Å^{-1} is not specific to the hard carbons used in this study, but was also observed in a commercial hard carbon (**Figure 3.14**(a)). Emphasis is also given to the fact that the signal disappeared if the sodiated sample became damaged by exposure to trace amounts of H_2O, O_2, or CO_2 (Figure 3.14(b)). This has hindered observation and identification in previous work. The origin of this new broad peak will be discussed later.

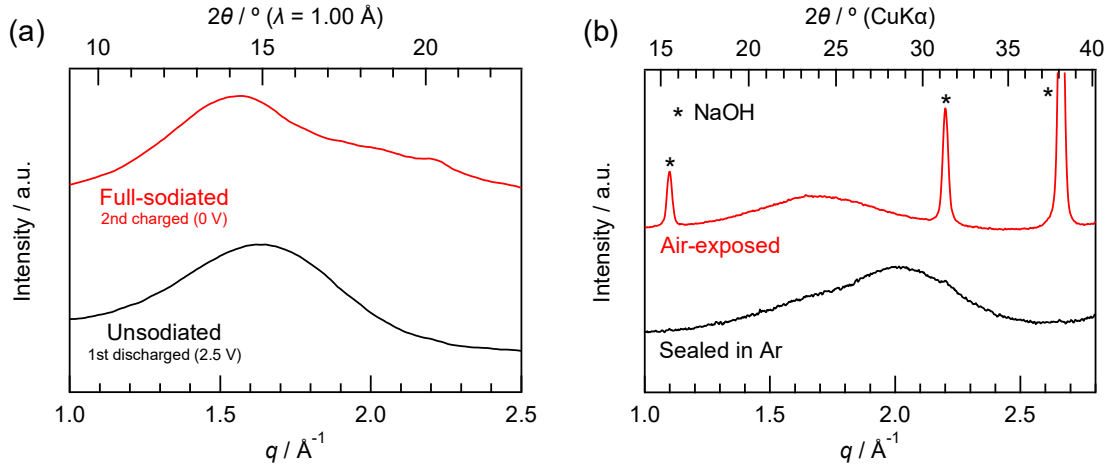

Figure 3.14 (a) *Ex situ* WAXS patterns of electrodes prepared using a commercial hard carbon (CarbotronP(J), Kureha Corporation). The data were obtained at the BL-8B beamline of Photon Factory, High Energy Accelerator Research Organization (KEK), Tsukuba, Japan. Structural Broad peak of scattering intensity at $q \approx 2.0$ Å^{-1} was observed in the full-sodiated sample as discussed in the main text. (b) *Ex situ* WAXS patterns of sodiated hard carbon electrode with/without exposure to air (HC-1400, point I). The air exposure eliminated the broad signal at $q \approx 2.0$ Å^{-1} and resulted NaOH formation alternatively.

After sodium metal nucleation (points X and Y in Figure 3.12), a sharp Bragg reflection from bulk sodium metal became detectable at $q = 2.07$ Å^{-1}, indicating that the deposition/dissolution reactions of bulk sodium metal do not occur at voltages above 0 V. In the overcharged samples, the deposition of sodium metal on the electrode surface was observed (**Figure 3.15**). In addition, it was noticed that the electrodeposition of bulk sodium metal does not occur before metal nucleation even below 0 V (Figure 3.12, point L), as reported previously.[48,49]

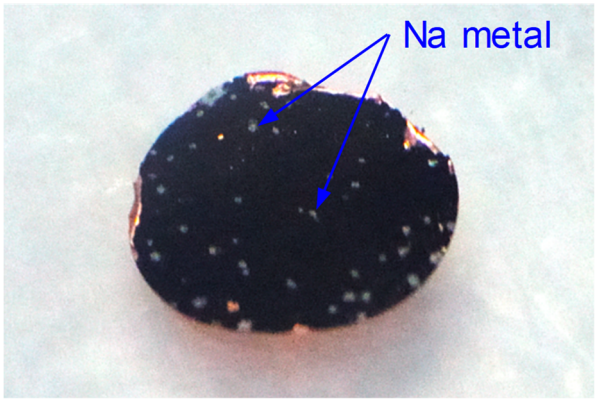

Figure 3.15 Picture of overcharged electrode (HC-1900, point Y in Figure 3.12). Deposited sodium metal was scattered on the electrode surface.

For a more quantitative analysis, we assumed three major components that constitute the whole WAXS pattern: (1) the interlayer correlation, (2) the new broad peak, and (3) the bulk sodium metal, as pseudo-Voigt functions. The peak areas and the widths were refined by a non-linear least-square regression method as implemented in lmfit.[51] Details of the fitting procedures are provided in Appendix A. As shown in Figure 3.13(d), at the beginning of sodiation (f_{Na} < 10%), the interlayer distance slightly decreased in all the samples. Although the mechanism of this phenomenon is not well understood, sodium adsorption on the graphene defects and edges could occur, as claimed previously.[7,14,52–55] Adsorption of sodium on defects will be discussed in detail in sention 3.6. Subsequently, upon further sodiation up to f_{Na} ≈ 50–80%, the interlayer continuously expanded, and the expansion amplitude tends to be significantly smaller as the preparation temperature increases. HC-1900 showed a small change in interlayer distance compared to the other two samples, implying that the sodium atoms were not intercalated into most of the interlayers, and there might be a threshold for the interlayer spacing (> 3.6 Å) to allow the sodium intercalation. The existence of a threshold interlayer distance around d = 3.6 Å is consistent with the results of density functional theory (DFT) calculations by Cao *et al.*,[56] as well as with many experimental results indicating that hard carbons with d < 3.6 Å show no interlayer expansion even after full sodiation.[15,57–60] However,

since the amount of expansion of the interlayer distance from the initial state (f_{Na} = 0%) is the smallest in HC-1400, I cannot deny the possibility that the amount of defects determines whether or not sodium can intercalate into interlayer. It is necessary to investigate the reason why the interlayer distance decreases by the sodium adsorption on the graphene defects/edges, or to clarify the relationship between the amount of defects and the possibility of intercalation.

Figure 3.16(a) shows the *ex situ* SAXS patterns of electrochemically sodiated hard carbon electrodes at various depths of charge. In all samples, the deeply sodiated electrodes yielded weaker scattering intensities from the nanopores. However, the nanopore scattering signals recovered to their initial intensities when the electrodes were desodiated, as shown in the insets of Figure 3.16(a). This reversible change in the scattering intensity reflects the change in the contrast between the electron density in the nanopores and the carbon matrix, demonstrating that the nanopores act as reversible sodium storage sites.[2,6]

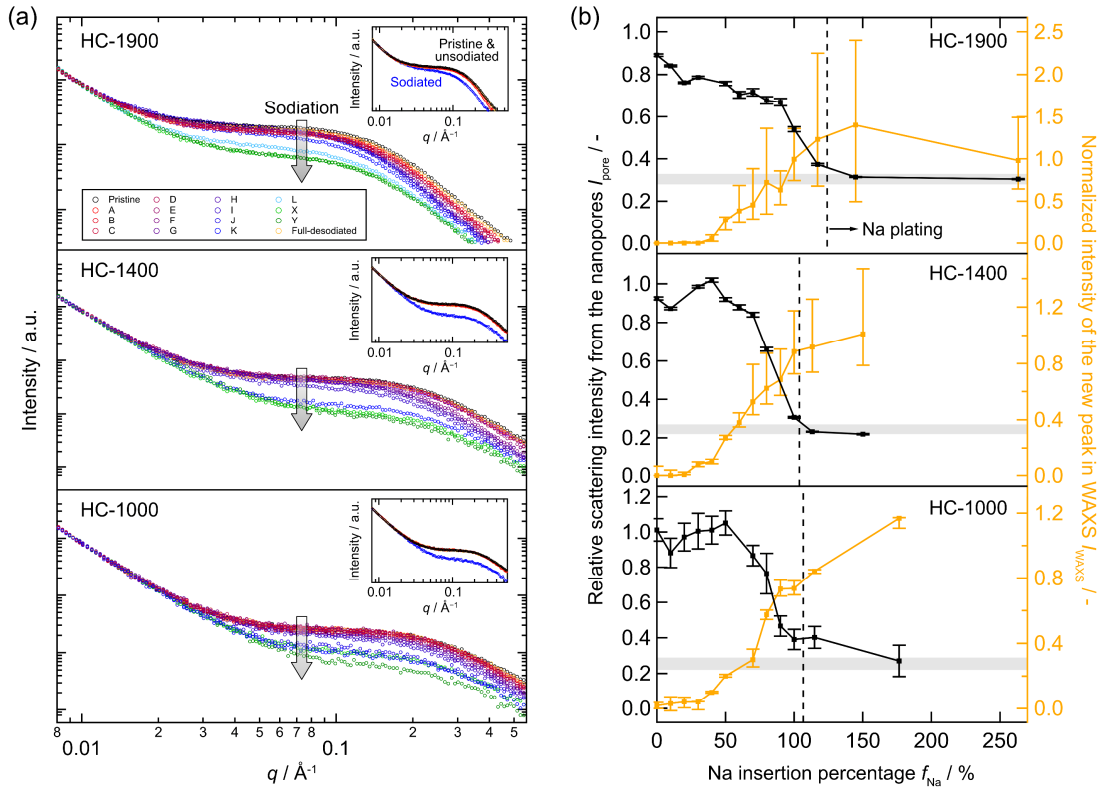

Figure 3.16 (a) *Ex situ* SAXS profiles of hard carbon electrodes at various stage of sodiation. In the inset, the SAXS patterns of the fully sodiated and desodiated electrodes are extracted. The arrows indicate the direction of sodiation. (b) Relative scattering intensity from the nanopores and the normalized intensity of the new broad peak at $q \approx 2.0$–2.1 Å^{-1} observed in the WAXS pattern as a function of sodium insertion percentage. The horizontal gray line shows the scattering intensity assuming that bulk bcc sodium was plated in the nanopores of each hard carbon sample.

The variations in the scattering intensity of the nanopores were quantitatively analyzed and are summarized in Figure 3.16(b). The ratio of the scattering intensity from the nanopores of each *ex situ* sample to that of the pristine state is denoted the "relative scattering intensity from the nanopore" (I_{pore}). I_{pore} is 1 when the nanopores are empty and decreases with increasing sodium insertion. In HC-1000 and HC-1400, insertion into the nanopores (decrease in I_{pore}) progresses at $f_{\mathrm{Na}} > 40$—50%, whereas, in HC-1900, it progresses throughout the sodiation process. These observed behaviors suggest that the filling of the nanopores with Na proceeds in the low-voltage region ($V < 0.06$—0.08 V) and acts as a major mechanism of charge storage, which is consistent with previous

reports.[2,6] I also confirmed that the nanopore filling proceeds even below 0 V (f_{Na} > 100%) in all samples, suggesting that the nanopores are still not fully utilized at 0 V.

The number density of sodium atoms confined in the nanopores was analyzed using the Guinier approximation. The estimated number densities in the nanopores at V = 0 V (point K in Figure 3.12) are 20, 25, and 16 atoms nm^{-3} for HC-1000, HC-1400, and HC-1900, respectively. The highest value of 25 atoms nm^{-3} for HC-1400 is comparable to that of bulk body-centered cubic (bcc) sodium (26 atoms nm^{-3}), and this packing allowed the maximum utilization of the nanopores, which had a suitable size and accessibility.

The nanopore filling process observed by SAXS (decrease in I_{pore}) is accompanied by a simultaneous emergence of another signal in the WAXS profile, as discussed above. Figure 3.16(b) shows the nanopore scattering intensities (I_{pore}) in the SAXS pattern and the normalized intensity of the new peak in the WAXS pattern (I_{WAXS}). I_{WAXS} is defined as the relative intensity with respect to the peak intensity of the interlayer correlation from the graphitic domain of the carbon matrix ($q \approx$ 1.6–1.8 Å^{-1}), and, therefore, can serve as the indicator of formation of a dense Na assembly as described below. From the simultaneous changes in these two parameters (decrease in I_{pore} and increase in I_{WAXS}) at different observation scales obtained from SAXS and WAXS measurements, I postulated that the origin of the new signal in the WAXS profile is the atomic correlation of sodium in the nanopores. To validate this postulation, I performed WAXS simulations utilizing hypothetical atomic structures derived by DFT-based molecular dynamics (DFT-MD) simulations for various sizes of the Na assembly (Figure 3.17).

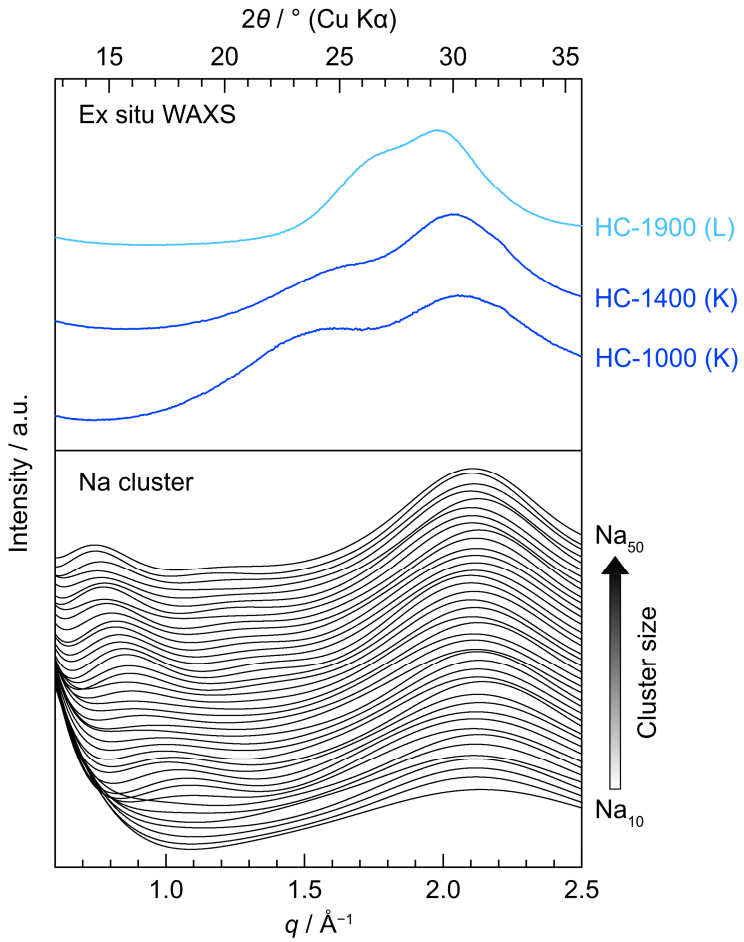

Figure 3.17 *Ex situ* WAXS pattern of hard carbon electrodes sodiated just before the bulk Na deposition (upper) and scattering patterns of sodium cluster obtained from DFT-MD simulation.(lower)

Regardless of the diversity of sizes and structures, the scattering patterns have a characteristic broad peak at $q \approx 2.1$ Å^{-1}, which is assigned to the nearest neighbor Na–Na correlation (*ca*. 3.7 Å, **Figure 3.18**). Therefore, the new broad peak in the experimental WAXS profile at $q \approx 2.0$–2.1 Å^{-1} can be attributed to the dense Na assemblies in the nanopores. Such a short Na—Na distance is not possible in the ionic state because of the electrostatic repulsion; however, for a pseudo-metallic case, the Na—Na separation can be shorter. The existence of such pseudo-metallic sodium in the nanopores is supported by *operando* ^{23}Na nuclear magnetic resonance (NMR) spectroscopy, X-ray total scattering, and DFT calculations.[61–64] In addition, the pseudo-metallic state is maintained even in an overcharged state. This is presumed from the fact that the broad peak due to Na clusters

continue to exist even after metal deposition (points X and Y in Figure 3.12).

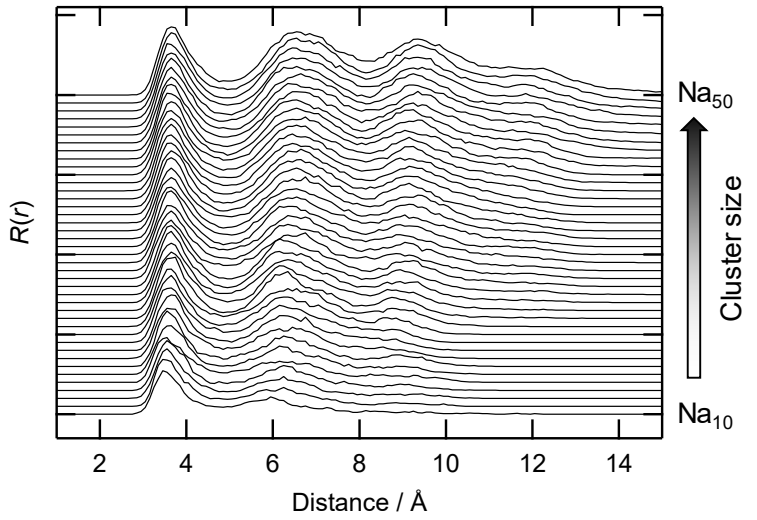

Figure 3.18 Radial distribution function (RDF) ($R(r)$) of sodium clusters at T = 300 K obtained from DFT-MD calculations. RDFs are calculated from Na_{10} to Na_{50} and the calculation results are arranged in ascending order of cluster from the bottom to the top. The RDF is defined as

$$R(r) = \sum_i \sum_j \delta(|r - r_{ij}|)$$

,where r_{ij} is distance between atom i and j, and the $\delta(|r - r_{ij}|) = 1$ when $|r - r_{ij}| < 0.05$.

Furthermore, galvanostatic intermittent titration technique (GITT) was carried out to investigate the sodium storage mechanism through the evaluation of kinetic properties (**Figure 3.19**). The diffusion coefficient variation is similar during sodiation and desodiation, suggesting the process of chare and discharge almost reversible.[65–67] In all the samples, the diffusivity is higher at the initial stage of the sodiation (V > 0.2 V) than those of the subsequent regions. High diffusivity suggests that sodium ion adsorbs to hard carbon surface (in particular, graphene defects and edges) in this region.[14,65,67] After these adsorption sites are occupied, it is assumed that intercalation between the graphene–graphene interlayer proceeds. It can be explained that the diffusion coefficient decreases in the subsequent region because sodium ions need to overcome an energy barrier form graphite sheets to diffuse between the layers.[14,65,67] Subsequent changes in the diffusion coefficient can be

described as follows. As the diffusion distance to the storage site continues lengthening, the diffusion coefficient gradually decreases, but the diffusion coefficient is recovered by expanding the interlayer space with sodium intercalaion.[14,65,67] Thus, GITT results are in good agreement with the reaction mechanism obtained from SAXS and WAXS.

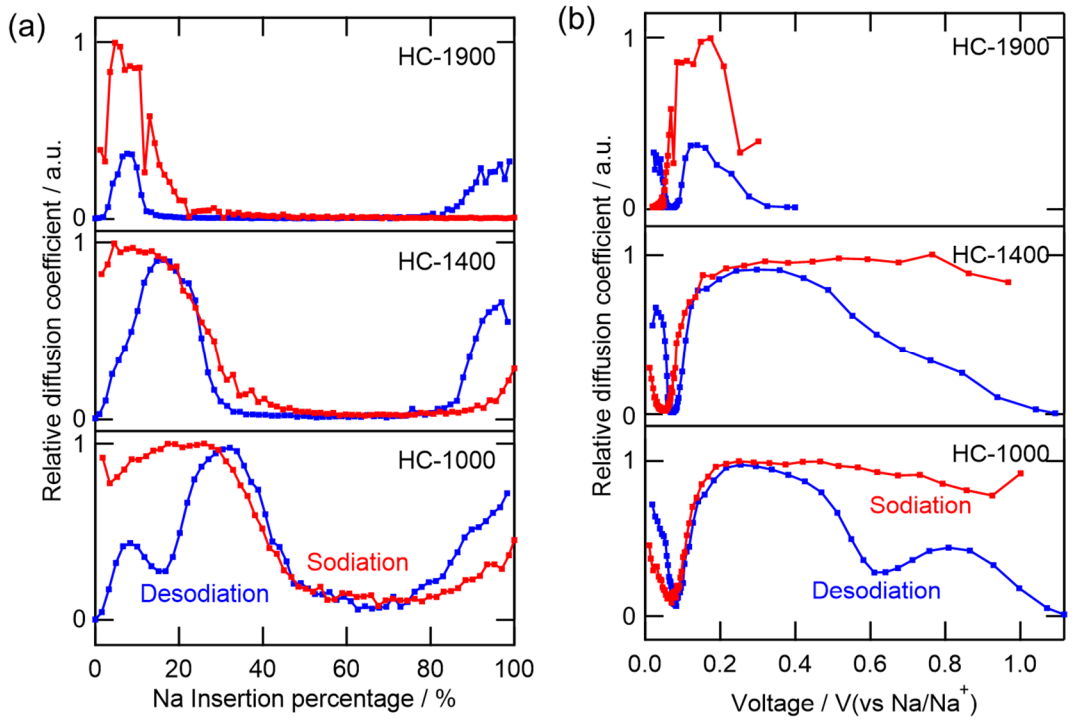

Figure 3.19 Change in relative diffusion coefficient of all hard carbon electrodes evaluated by GITT (a) as function of sodium insertion percentage, (b) as function of voltage. The diffusion coefficients were estimated by using the equation based on simplified Fick's second law:[68]

$$D \approx \frac{4}{\pi\tau}\left(\frac{m_b V_M}{M_B S}\right)^2 \left(\frac{\Delta E_s}{\Delta E_\tau}\right)^2$$

where D is the diffusion coefficient of sodium ions, τ is the pulse duration, m_b and M_B are mass and molar mass of sample, V_M is molar volume of sample, and S is the active surface area of the electrodes. ΔE_S and ΔE_τ the potential difference and potential change obtained from the GITT curves. Since I do not have density values (M_B/V_M [g cm^{-3}]) for each hard carbon, absolute values of diffusion coefficients cannot be determined and comparison between samples cannot be done. However, it is worth to conducting GITT measurements because the changes in diffusion coefficient

within each sample can be examined. For each hard carbon, the relative diffusion coefficient at various states of charge was calculated, where the value at the time of the highest diffusivity was set to 1.

3.6 Sodium adsorption on graphene defects

Referring to the calculation model of Tsai *et al.*,[7] the potential at which sodium adsorption reaction occurs was calculated using VASP. As a simplified model of hard carbon, three types of defect (mono-vacancy (MV), di-vacancy (DV), and Stone–Wales (SW)) were introduced into graphene sheet. The main differences between this calculation and a previous calculation are as follows:

Previous (Tsai *et al.*)[7]	**This work**
➢ Adsorption potential was calculated only for some adsorption sites	➢ Adsorption potential was calculated for all adsorption sites
➢ The structure was optimized by changing only the distance between sodium and graphene sheet (the coordinates of carbon atoms in graphene were fixed)	➢ The structure was optimized by changing the coordinates of all carbon and sodium atoms (closer to the real system)
➢ Flat-type SW graphene was used	➢ Sine-like SW graphene (the most stable structure,[69,70] **Figure 3.20**) was used

Considering the symmetry of each graphene, adsorption sites O*i* with different distances from the introduced defects were defined as shown in **Figure 3.21**. The sites shown in blue are the sites that have already been calculated by Tsai *et al.*, and the sites shown in red are the newly calculated sites.

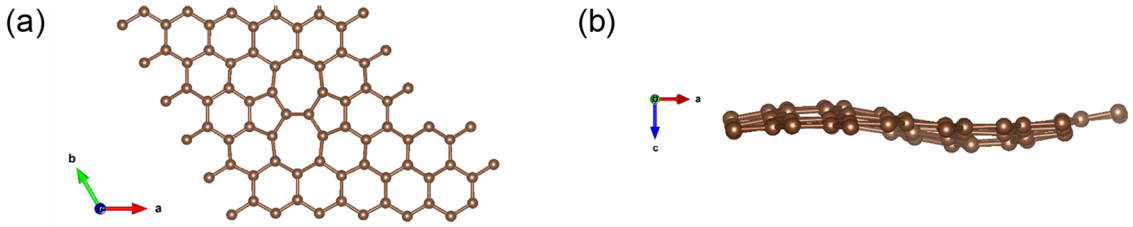

Figure 3.20 (a) Top and (b) side views of the sine-like SW defect.[69,70]

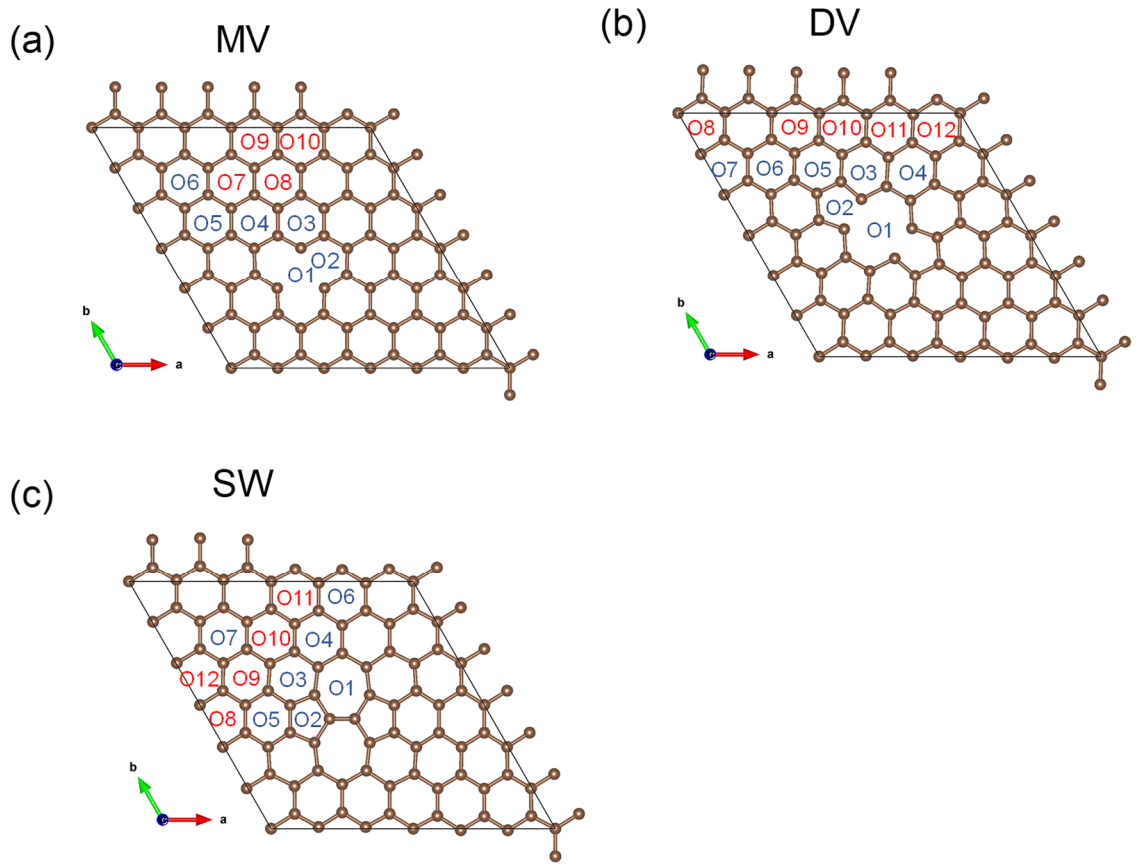

Figure 3.21 Inequivalent hollow sites O_i in MV, DV and SW.

The adsorption potential of sodium at each site was calculated based on formula (3.2).

$$V = -(E_{\text{Sodium-surf}} - E_{\text{Surf}} - E_{\text{Sodium}}) \tag{3.2}$$

Here, $E_{\text{Sodium-surf}}$ is the total energy when sodium is adsorbed on defective graphene, E_{Surf} is the

total energy of defective graphene, and E_{Sodium} is the total energy of sodium. The adsorption potentials of sodium on defect-free graphene were calculated to be −0.25 V (vs. Na/Na^+). Therefore, the metal plating reaction of sodium occurs before the adsorption reaction.

Figure 3.22 shows the calculation result of adsorption potential. Overall, higher potential results were obtained than in previous studies by Tsai *et al*. In MV and DV graphene, it was confirmed that adsorption reaction occurred above 0 V at all sites. O_1 and O_2 show a high potential over 0.5 V. In MV graphene, the adsorption potential at O_1, O_2, and O_3 sites are the same. This is because the sodium atoms arranged on O_2 and O_3 move to O_1 during the process of structural relaxation. In SW graphene, there are some sites where adsorption reaction occurs above 0 V. However, the adsorption potential is generally lower than that of MV and DV graphene.

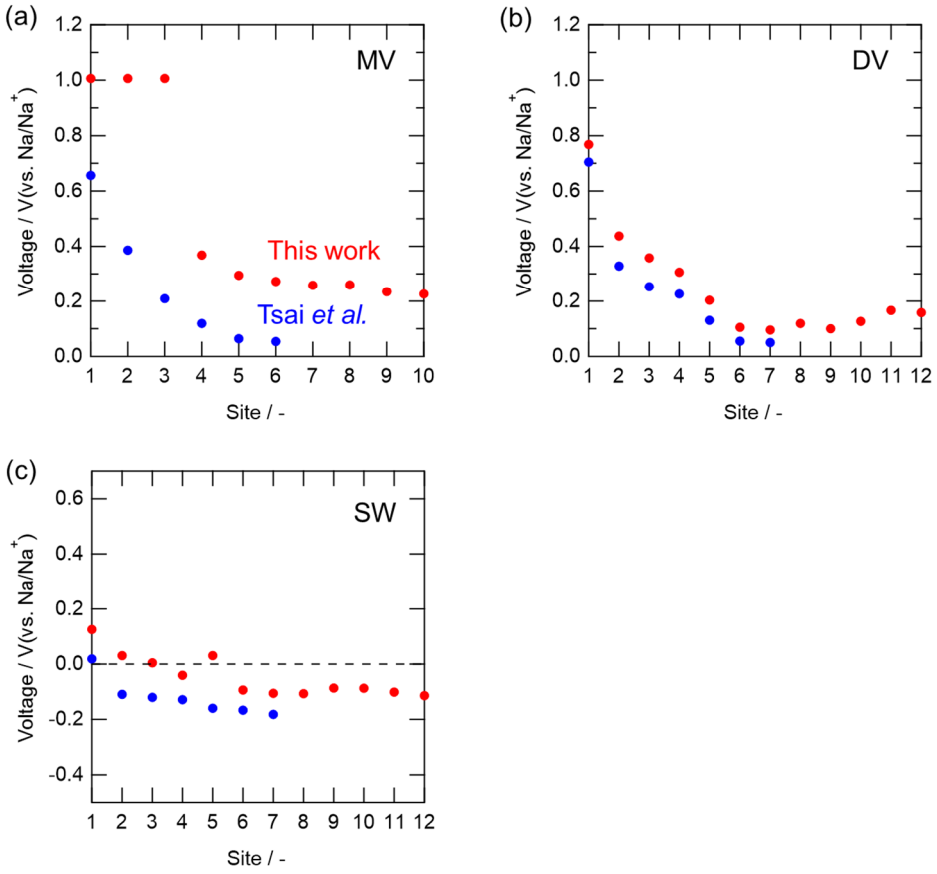

Figure 3.22 The adsorption potential of (a) MV, (b) DV, and (c) SW graphene.

It was found that defect adsorption at a high potential is most likely to occur in MV graphene and can also occur in SW graphene by a modified calculation that is more realistic than in the previous report.

3.7 Sample-dependent sodium storage mechanism into hard carbon

By combining the results of the analyses reported above, I reconsidered a sample-dependent sodium storage mechanism into hard carbon, which is summarized in **Figure 3.23**. I believe that the overall explanation is possible by assuming three sodium storage sites: 1) the graphene defects and edges, 2) graphene–graphene interlayers, and 3) the nanopores. To maximize the sodium storage capacity, contributions from three mechanisms should be controlled and optimized by changing the precursors or the heat treatment conditions.

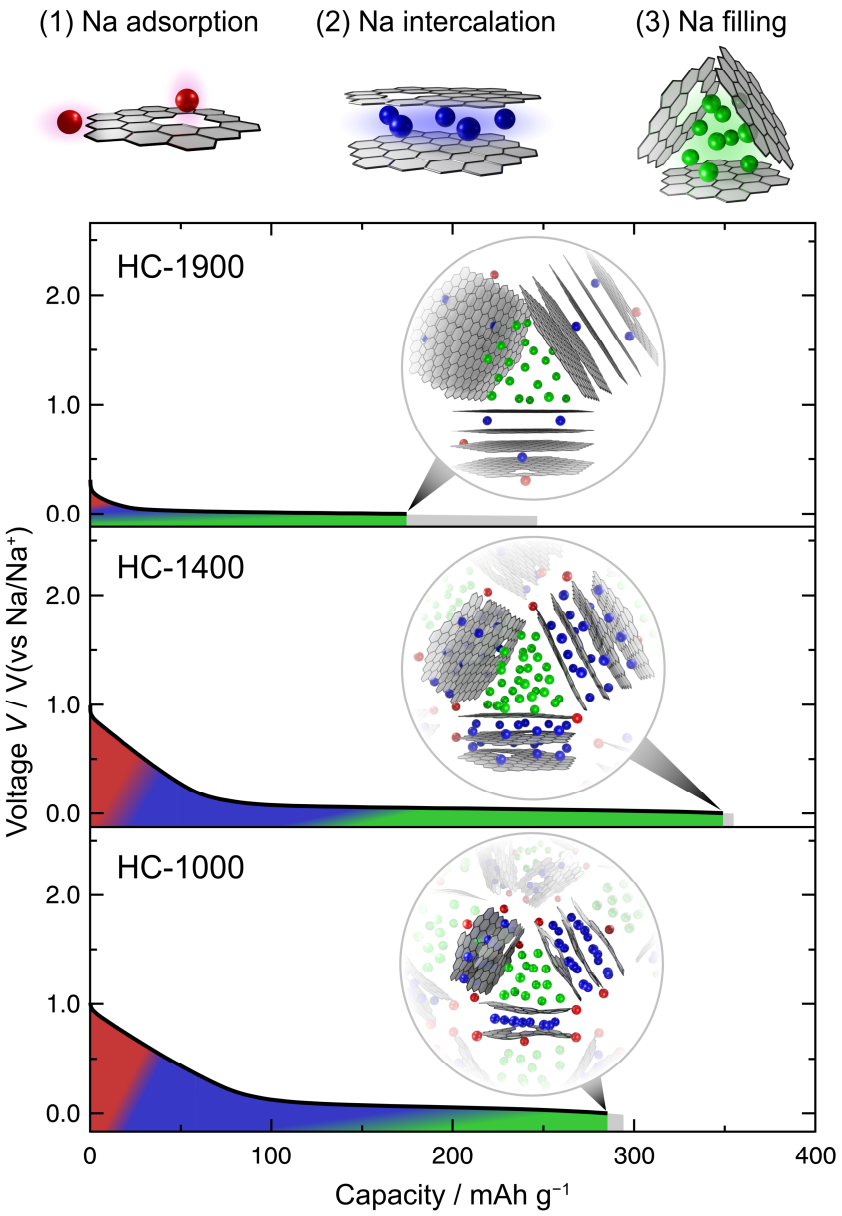

Figure 3.23 Schematic diagrams of the sodium storage mechanism in hard carbon. Gray areas indicate unused capacity because of slow kinetics.

On the basis of the effect of the heat treatment temperature observed in this study, a larger number of defects tend to remain in the graphene prepared at lower preparation temperatures, resulting in a larger capacity with a sloping profile (Q_{slope}), which is ascribed to Na adsorption at defects (mechanism 1). The sodium intercalation capacity in the graphitic domain (mechanism 2) is also larger at lower preparation temperatures because of the larger graphene–graphene interlayer

distance than the threshold separation (3.6 Å) or smaller number of defects for sodium intercalation. However, sample preparation at lower temperatures increased the surface area and, thus, the number of functional groups and defects that can cause an irreversible reaction upon the initial sodiation.

The capacity ascribed to Na filling into the nanopores (mechanism 3) does not show monotonic variation with the heat treatment temperature but has a maximum around T = 1400 °C. Although the nanopore-derived capacity may be increased by the higher temperature treatment, the practical capacity is limited by the slow kinetics that induce polarization and limit the accessible capacity in the low voltage region (**Figure 3.24**). A possible reason for the slow kinetics might be the lack of low sodium acceptability in the carbon matrix as shown by the poor sodium intercalation ability of the graphitic domain. Therefore, excessive graphitization should be avoided to utilize the closed nanopores fully.

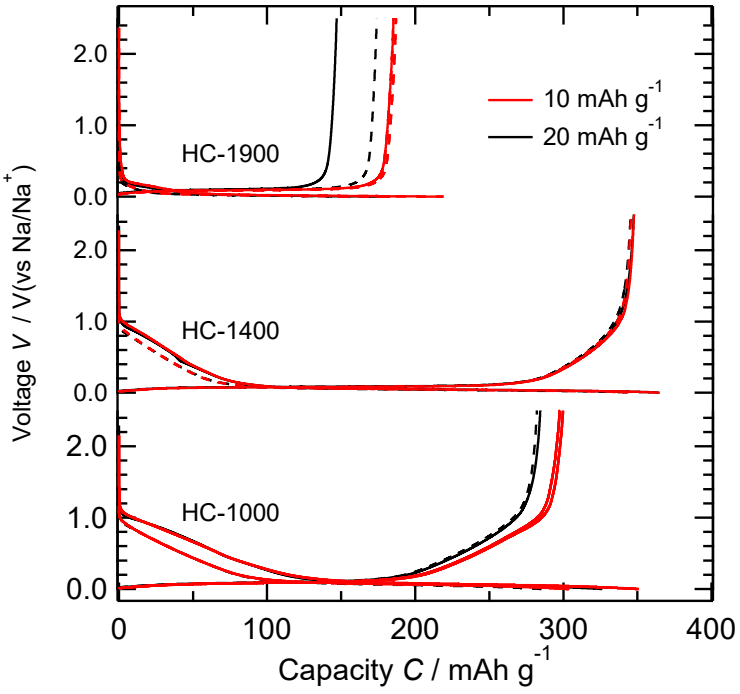

Figure 3.24 Comparison of charge-discharge curves at a current density of 10 and 20 mA g^{-1}. The solid line indicates the first cycle and the dotted line indicates the second cycle.

3.8 Conclusion

I have thoroughly investigated the correlation between micro-/atomic structures and the sodium storage properties of hard carbons prepared by various heat-treatment temperatures. The combined *ex situ* SAXS/WAXS experiments have unveiled the reversible formation of pseudo-metallic sodium in the nanopores of the hard carbon and show the dominant contribution to the large reversible capacity of the hard carbon electrode. A characteristic scattering peak in the WAXS pattern identified in this study can be utilized for the identification of the densely confined sodium in nanospaces not only in hard carbon samples but also in other nanoporous materials. The author believes the newly developed measurement method can be applied to other easily damaged materials.

References

1. Stevens, D. A. & Dahn, J. R. High Capacity Anode Materials for Rechargeable Sodium-Ion Batteries. *J. Electrochem. Soc.* **147**, 1271 (2000).
2. Komaba, S. *et al.* Electrochemical Na Insertion and Solid Electrolyte Interphase for Hard-Carbon Electrodes and Application to Na-Ion Batteries. *Adv. Funct. Mater.* **21**, 3859–3867 (2011).
3. Dahbi, M., Yabuuchi, N., Kubota, K., Tokiwa, K. & Komaba, S. Negative electrodes for Na-ion batteries. *Phys. Chem. Chem. Phys.* **16**, 15007 (2014).
4. Yamamoto, H. *et al.* Synthesizing higher-capacity hard-carbons from cellulose for Na- and K-ion batteries. *J. Mater. Chem. A* **6**, 16844–16848 (2018).
5. Dou, X. *et al.* Hard carbons for sodium-ion batteries: Structure, analysis, sustainability, and electrochemistry. *Mater. Today* **23**, 87–104 (2019).
6. Stevens, D. A. & Dahn, J. R. The Mechanisms of Lithium and Sodium Insertion in Carbon Materials. *J. Electrochem. Soc.* **148**, A803 (2001).
7. Tsai, P., Chung, S.-C., Lin, S. & Yamada, A. Ab initio study of sodium intercalation into disordered carbon. *J. Mater. Chem. A* **3**, 9763–9768 (2015).
8. Jiao, J., Xiao, R., Tian, M., Wang, Z. & Chen, L. First-principles calculations on lithium and sodium adsorption on graphene edges. *Electrochim. Acta* **282**, 205–212 (2018).
9. Yang, S. *et al.* Sodium adsorption and intercalation in bilayer graphene from density functional theory calculations. *Theor. Chem. Acc.* **135**, 164 (2016).
10. Bommier, C., Ji, X. & Greaney, P. A. Electrochemical Properties and Theoretical Capacity for Sodium Storage in Hard Carbon: Insights from First Principles Calculations. *Chem. Mater.* **31**, 658–677 (2019).
11. Olsson, E., Chai, G., Dove, M. & Cai, Q. Adsorption and migration of alkali metals (Li, Na, and K) on pristine and defective graphene surfaces. *Nanoscale* **11**, 5274–5284 (2019).
12. Qiu, S. *et al.* Manipulating Adsorption-Insertion Mechanisms in Nanostructured Carbon Materials for High-Efficiency Sodium Ion Storage. *Adv. Energy Mater.* **7**, 1700403 (2017).
13. Lu, H. *et al.* Exploring Sodium-Ion Storage Mechanism in Hard Carbons with Different Microstructure Prepared by Ball-Milling Method. *Small* **14**, 1802694 (2018).
14. Bommier, C., Surta, T. W., Dolgos, M. & Ji, X. New Mechanistic Insights on Na-Ion Storage in Nongraphitizable Carbon. *Nano Lett.* **15**, 5888–5892 (2015).
15. Zhang, B., Ghimbeu, C. M., Laberty, C., Vix-Guterl, C. & Tarascon, J.-M. Correlation Between Microstructure and Na Storage Behavior in Hard Carbon. *Adv. Energy Mater.* **6**, 1501588 (2016).

16. Saurel, D. *et al.* From Charge Storage Mechanism to Performance: A Roadmap toward High Specific Energy Sodium-Ion Batteries through Carbon Anode Optimization. *Adv. Energy Mater.* **8**, 1703268 (2018).
17. Xiao, B., Rojo, T. & Li, X. Hard Carbon as Sodium-Ion Battery Anodes: Progress and Challenges. *ChemSusChem* **12**, 133–144 (2019).
18. Kano, A. *et al.* New Carbon Materials with Large Closed Pore Volume As Anode for High Energy Na-Ion Batteries. *Electrochem. Soc.* 221 (2015).
19. Kano, A., Hojo, N. & Fujimoto, M. US 20160104889,. (2016).
20. Zhang, N. *et al.* High capacity hard carbon derived from lotus stem as anode for sodium ion batteries. *J. Power Sources* **378**, 331–337 (2018).
21. Wang, Q., Li, H., Chen, L. & Huang, X. Monodispersed hard carbon spherules with uniform nanopores. *Carbon N. Y.* **39**, 2211–2214 (2001).
22. Kresse, G. & Furthmüller, J. Efficiency of ab-initio total energy calculations for metals and semiconductors using a plane-wave basis set. *Comput. Mater. Sci.* **6**, 15–50 (1996).
23. Blöchl, P. E. Projector augmented-wave method. *Phys. Rev. B* **50**, 17953–17979 (1994).
24. Kresse, G. & Joubert, D. From ultrasoft pseudopotentials to the projector augmented-wave method. *Phys. Rev. B* **59**, 1758–1775 (1999).
25. Nosé, S. A unified formulation of the constant temperature molecular dynamics methods. *J. Chem. Phys.* **81**, 511–519 (1984).
26. Hoover, W. G. Canonical dynamics: Equilibrium phase-space distributions. *Phys. Rev. A* **31**, 1695–1697 (1985).
27. Noya, E. G., Doye, J. P. K., Wales, D. J. & Aguado, A. Geometric magic numbers of sodium clusters: Interpretation of the melting behaviour. in *European Physical Journal D* vol. 43 57–60 (EDP Sciences, 2007).
28. Debye, P. Zerstreuung von Röntgenstrahlen. *Ann. Phys.* **351**, 809–823 (1915).
29. Wojdyr, M. Debyer. https://github.com/wojdyr/debyer (2011).
30. Franklin, R. E. The structure of graphitic carbons. *Acta Crystallogr.* **4**, 253–261 (1951).
31. Franklin, R. E. The interpretation of diffuse X-ray diagrams of carbon. *Acta Crystallogr.* **3**, 107–121 (1950).
32. Franklin, R. E. Crystallite growth in graphitizing and non-graphitizing carbons. *Proc. R. Soc. London. Ser. A. Math. Phys. Sci.* **209**, 196–218 (1951).
33. Xing, W., Xue, J. S., Zheng, T., Gibaud, A. & Dahn, J. R. Correlation Between Lithium Intercalation Capacity and Microstructure in Hard Carbons. *J. Electrochem. Soc.* **143**, 3482 (1996).
34. Dahbi, M. *et al.* Synthesis of hard carbon from argan shells for Na-ion batteries. *J.*

Mater. Chem. A **5**, 9917–9928 (2017).

35. Guinier, A. & Fournet, G. *Small-angle Scattering of X-rays*. (John Wiley & Sons, Inc., 1955).
36. Shibayama, M., Nomura, S., Hashimoto, T. & Thomas, E. L. Asymptotic behavior and Lorentz factor for small-angle elastic scattering profiles from preferentially oriented asymmetric bodies. *J. Appl. Phys.* **66**, 4188–4197 (1989).
37. Bose, S. & Bragg, R. H. Small-angle x-ray scattering from oriented ellipsoidal voids in pyrolytic graphite. *J. Appl. Phys.* **49**, 2916–2918 (1978).
38. Dahn, J. R., Xing, W. & Gao, Y. The "falling cards model" for the structure of microporous carbons. *Carbon N. Y.* **35**, 825–830 (1997).
39. Dahbi, M. *et al.* Effect of Hexafluorophosphate and Fluoroethylene Carbonate on Electrochemical Performance and the Surface Layer of Hard Carbon for Sodium-Ion Batteries. *ChemElectroChem* **3**, 1856–1867 (2016).
40. Izanzar, I. *et al.* Hard carbons issued from date palm as efficient anode materials for sodium-ion batteries. *Carbon N. Y.* **137**, 165–173 (2018).
41. Simone, V. *et al.* Hard carbon derived from cellulose as anode for sodium ion batteries: Dependence of electrochemical properties on structure. *J. Energy Chem.* **25**, 761–768 (2016).
42. Ferrari, A. C. & Robertson, J. Interpretation of Raman spectra of disordered and amorphous carbon. *Phys. Rev. B* **61**, 14095–14107 (2000).
43. Ferrari, A. C. Raman spectroscopy of graphene and graphite: Disorder, electron–phonon coupling, doping and nonadiabatic effects. *Solid State Commun.* **143**, 47–57 (2007).
44. Sadezky, A., Muckenhuber, H., Grothe, H., Niessner, R. & Pöschl, U. Raman microspectroscopy of soot and related carbonaceous materials: Spectral analysis and structural information. *Carbon N. Y.* **43**, 1731–1742 (2005).
45. Sun, N. *et al.* Extended "Adsorption–Insertion" Model: A New Insight into the Sodium Storage Mechanism of Hard Carbons. *Adv. Energy Mater.* **9**, 1901351 (2019).
46. Hasegawa, G. *et al.* Hard Carbon Anodes for Na-Ion Batteries: Toward a Practical Use. *ChemElectroChem* **2**, 1917–1920 (2015).
47. Hasegawa, G. *et al.* Studies on electrochemical sodium storage into hard carbons with binder-free monolithic electrodes. *J. Power Sources* **318**, 41–48 (2016).
48. Zheng, Y., Wang, Y., Lu, Y., Hu, Y.-S. & Li, J. A high-performance sodium-ion battery enhanced by macadamia shell derived hard carbon anode. *Nano Energy* **39**, 489–498 (2017).
49. Zheng, Y. *et al.* Superior electrochemical performance of sodium-ion full-cell using poplar wood derived hard carbon anode. *Energy Storage Mater.* **18**, 269–279

(2019).
50. Ding, J. *et al.* Carbon Nanosheet Frameworks Derived from Peat Moss as High Performance Sodium Ion Battery Anodes. *ACS Nano* **7**, 11004–11015 (2013).
51. Newville, M., Ingargiola, A., Stensitzki, T. & Allen, D. B. LMFIT: Non-Linear Least-Square Minimization and Curve-Fitting for Python. *Zenodo* (2014) doi:10.5281/ZENODO.11813.
52. Alvin, S. *et al.* Revealing sodium ion storage mechanism in hard carbon. *Carbon N. Y.* **145**, 67–81 (2019).
53. Zhong, X. *et al.* High-Performance Sodium-Ion Batteries Based on Nitrogen-Doped Mesoporous Carbon Spheres with Ultrathin Nanosheets. *ACS Appl. Mater. Interfaces* **11**, 2970–2977 (2019).
54. Anji Reddy, M., Helen, M., Groß, A., Fichtner, M. & Euchner, H. Insight into Sodium Insertion and the Storage Mechanism in Hard Carbon. *ACS Energy Lett.* **3**, 2851–2857 (2018).
55. Yun, Y. S. *et al.* Sodium-Ion Storage in Pyroprotein-Based Carbon Nanoplates. *Adv. Mater.* **27**, 6914–6921 (2015).
56. Cao, Y. *et al.* Sodium ion insertion in hollow carbon nanowires for battery applications. *Nano Lett.* **12**, 3783–3787 (2012).
57. Li, Q. *et al.* Commercial activated carbon as a novel precursor of the amorphous carbon for high-performance sodium-ion batteries anode. *Carbon N. Y.* **129**, 85–94 (2018).
58. Wang, Y. *et al.* High capacity and high efficiency maple tree-biomass-derived hard carbon as an anode material for sodium-ion batteries. *Materials (Basel).* **11**, 1294 (2018).
59. Bai, P. *et al.* Elucidation of the Sodium-Storage Mechanism in Hard Carbons. *Adv. Energy Mater.* **8**, 1703217 (2018).
60. Luo, X. F., Yang, C. H. & Chang, J. K. Correlations between electrochemical Na+ storage properties and physiochemical characteristics of holey graphene nanosheets. *J. Mater. Chem. A* **3**, 17282–17289 (2015).
61. Stratford, J. M., Allan, P. K., Pecher, O., Chater, P. A. & Grey, C. P. Mechanistic insights into sodium storage in hard carbon anodes using local structure probes. *Chem. Commun.* **52**, 12430–12433 (2016).
62. Deringer, V. L. *et al.* Towards an atomistic understanding of disordered carbon electrode materials. *Chem. Commun.* **54**, 5988–5991 (2018).
63. Huang, J.-X., Csányi, G., Zhao, J.-B., Cheng, J. & Deringer, V. L. First-principles study of alkali-metal intercalation in disordered carbon anode materials. *J. Mater. Chem. A* **7**, 19070–19080 (2019).
64. Morita, R. *et al.* Correlation of carbonization condition with metallic property of

sodium clusters formed in hard carbon studied using 23 Na nuclear magnetic resonance. *Carbon N. Y.* **145**, 712–715 (2019).

65. Wang, J. *et al.* Facile hydrothermal treatment route of reed straw-derived hard carbon for high performance sodium ion battery. *Electrochim. Acta* **291**, 188–196 (2018).
66. Li, Y., Hu, Y.-S., Titirici, M.-M., Chen, L. & Huang, X. Hard Carbon Microtubes Made from Renewable Cotton as High-Performance Anode Material for Sodium-Ion Batteries. *Adv. Energy Mater.* **6**, 1600659 (2016).
67. Wang, Q. *et al.* Rice husk-derived hard carbons as high-performance anode materials for sodium-ion batteries. *Carbon N. Y.* **127**, 658–666 (2018).
68. Weppner, W. & Huggins, R. A. Determination of the Kinetic Parameters of Mixed-Conducting Electrodes and Application to the System Li3Sb. *J. Electrochem. Soc.* **124**, 1569–1578 (1977).
69. Openov, L. A. & Podlivaev, A. I. Interaction of the stone–wales defects in graphene. *Phys. Solid State* **57**, 1477–1481 (2015).
70. Ma, J., Alfè, D., Michaelides, A. & Wang, E. Stone-Wales defects in graphene and other planar s p2 -bonded materials. *Phys. Rev. B - Condens. Matter Mater. Phys.* **80**, 1–4 (2009).

4 Reversible and high-rate hard carbon negative electrodes in a fluorine-free sodium-salt electrolyte

4.1 Introduction

With growing concern about the supply risk of lithium resources, sodium-ion batteries (NIBs) using abundant and low-cost sodium resources have been actively researched for large-scale energy storage.[1–3] Hard carbon is a promising anode material for practical NIBs owing to its large capacity (>250 mAh g^{-1}) and low reaction potential (~0.1 V versus Na/Na^+).[4–9] The potential profile of hard carbon upon sodiation is composed of a sloping region (0.1–2.5 V) and a plateau region (0–0.1 V), and the latter constitutes more than half of the overall capacity. The large capacity of hard carbon in the plateau region can be regarded as both advantages and disadvantages. In order to increase the energy density of the battery, it is desirable to react at a low potential. Whereas, since the cut-off potential is very close to the reaction potential, it is easily affected by polarization, which results in poor rate performances. The main reason for the polarization of hard carbon is thought to be the resistance at electrode/electrolyte interface, and the disadvantage may be solved by forming a low-resistance SEI.

Because of the low reaction potential of hard carbon, at which most organic compounds are reduced, selecting appropriate electrolyte components (i.e., salts, solvents, and additives) or functional binders is essential to achieve the reversible cycling of hard carbon electrodes.[5,10–14] Regarding electrolyte design, a solid electrolyte interphase (SEI),[15,16] which is formed on a negative electrode by sacrificial reductive decomposition of electrolyte components, dominates the reversibility and kinetics of sodium insertion into hard carbon electrodes. Recent studies showed that a stable SEI could be formed by using fluorinated electrolytes containing, for example, sodium hexafluorophosphate ($NaPF_6$),[11,17] sodium bis(fluorosulfonyl)amide (NaFSA),[18–20] and fluoroethylene carbonate (FEC).[21–23] These fluorinated compounds are decomposed on the electrode surface to produce NaF, which has low solubility in an aprotic solvent, thus being considered to function as an essential component of the SEI to effectively suppress electrolyte decompositions.

However, from the viewpoint of green chemistry, the use of these fluorinated compounds is unfavorable due to their high toxicity and high environmental load. Because of this, fluorine-free electrolytes are being studied extensively.[24,25]

From the viewpoint of cycle characteristics toward practical application, it is necessary to develop a new electrolyte. Currently, 1 M $NaPF_6$/EC:DEC is widely used as a standard electrolyte. However, hard carbon electrodes exhibit a low initial coulombic efficiency in the standard electrolyte, which results in lower capacity and energy density in full cells. Moreover, to maintain 50% capacity after 1000 cycles, degradation per cycle must be suppressed to 0.07% or less ($0.9993^{1000} = 0.496$), but commercial electrolytes have not achieved this.

Recently, our group reported a fluorine-free electrolyte composed of sodium tetraphenylborate ($NaBPh_4$, **Figure 4.1**) and 1,2-dimethoxyethane (DME) that enables highly reversible plating/stripping of sodium metal negative electrodes.[26] This electrolyte does not contain fluorine, phosphorus, or sulfur elements, thus, there is no risk of generating a toxic gas (*e.g.*, hydrogen fluoride (HF), phosphoryl fluoride (POF_3), phosphorus pentafluoride (PF_5), or sulfur dioxide (SO_2)).[27–30] More importantly, this work suggests that fluorine is not indispensable in stabilizing such low-potential negative electrodes, although the detailed mechanism of the interface stabilization is still unclear.

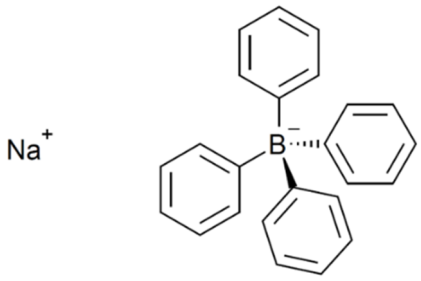

Figure 4.1 Chemical structure of $NaBPh_4$.

In this chapter, I aim to maximize the performance of hard carbon through electrode/electrolyte interface analysis and promote the practical application of NIBs. I studied the electrochemical reaction of hard carbon negative electrodes in a fluorine-free $NaBPh_4$/DME electrolyte because this system is fluorine-free and can be expected to have high efficiency and high rate performances. To understand the mechanism of stabilizing the interface, we scrutinized the effects of both counter anions and solvents using various salt/solvent combinations. I found highly reversible and high-rate cycling of hard carbon negative electrodes in $NaBPh_4$/DME electrolyte, suggesting that fluorine species are not indispensable in stabilizing the hard carbon/electrolyte interface. The mechanism of stabilizing the interface in this electrolyte was discussed based on the analysis of the hard carbon electrode surface.

4.2 Experimental methods

4.2.1 Preparation of electrolytes

$NaBPh_4$ (99.5%) was purchased from Wako Pure Chemical Industries. Sodium bis(trifluoromethanesulfonyl)amide ($NaN(SO_2CF_3)_2$, NaTFSA), $NaPF_6$, ethylene carbonate (EC):diethyl carbonate (DEC) (1:1 by volume), sulfolane (SL), DME, dimethyl carbonate (DMC), and a conventional electrolyte of 1 mol dm^{-3} (M) $NaPF_6$ in EC:DEC (1:1 by volume) were provided by Kishida Chemical and were of battery grade. High-purity NaFSA was supplied by Nippon Shokubai. $NaBPh_4$ was dried under vacuum at 120 °C for 12 h and the other battery-grade materials were used without any pretreatment. To prepare electrolyte solutions, Na salts were dissolved in solvents under Ar atmosphere in a glove box (Miwa Inc., Japan).

4.2.2 Electrochemical measurements

Hard carbon (Carbotron P(J)) provided by Kureha was used as a negative electrode without any

further purification. The hard carbon was mixed with carboxymethyl cellulose (CMC2200, Daicel) as a binder at a weight ratio of 9:1 in deionized water. The slurry was pasted onto copper current collector (thickness: 10 μm, Fuchikawa Material) with a doctor blade and then dried at 60 °C. $Na_2V_3O_7$ was choosed as a positive electrode material considering the potential window of the electrolyte and the reaction potential of the material. $Na_2V_3O_7$ was synthesized as reported in previous works.[31,32] The $Na_2V_3O_7$ electrode sheet was prepared by pasting a slurry made of $Na_2V_3O_7$ (80 wt%) mixed with Ketjen black (10 wt%, KB, Lion Corp.) and polyvinylidene fluoride (10 wt%, PVdF, Kureha) in N-methylpyrrolidone (NMP, Wako) onto Al foil using a 100 μm doctor blade and then dried at 60 ºC. The dried electrode sheets were punched into 12 mm diameter pieces and further dried overnight at 150 °C (for hard carbon) or 120 °C (for $Na_2V_3O_7$) in a vacuum. The mass loading of the negative electrode was ca. 1.6 mg cm^{-2}.

For battery tests, coin cells (2032-type) were assembled under Ar atmosphere in a glovebox. A Na metal (Wako) counter electrode and glass fiber separator (GB-50, Advantec) were used. The assembled hard carbon|Na metal and $Na_2V_3O_7$|Na metal coin cells weresubjected to charge-discharge tests at 25 °C with HJ1001SD8 (Hokuto Denko) at a current density of 20–6000 mA g^{-1}. Cutoff voltage was set at 0–2.5 V.

Linear sweep voltammetry (LSV) and cyclic voltammetry (CV) were performed by VMP-3 (BioLogic) using three-electrode cells. The working electrode was Pt or Cu, and the counter and reference electrodes were Na metal.

The ionic conductivity was evaluated with a two-electrode glass cell employing Pt electrodes via AC impedance spectroscopy (Solartron 147055BEC). The cell constant was evaluated in advance with a standard 1.0 M KCl aqueous solution.

The interfacial resistance of hard carbon electrodes was studied by AC impedance spectroscopy (Solartron 147055BEC) on a hard carbon|hard carbon symmetric cell with various electrolytes. The hard carbon electrodes were charged in advance to 0.01 V after one cycle in half cells, then

recovered under Ar atmosphere, and reused to assemble the symmetric cell with the same electrolytes. AC impedance spectroscopy was performed at the open circuit voltage over a frequency range of 1 MHz–10 mHz with an applied AC voltage of 10 mV.

4.2.3 Characterization of electrolytes and SEI

The X-ray photoelectron spectroscopy (XPS) was applied to analyze the surface of hard carbon electrodes. A PHI 5000 VersaProbe II spectrometer (ULVAC-PHI, Inc.) with Al Kα radiation was used. Before the XPS measurement, the hard half cells were subjected to three-cycles charge-discharge measurement at 20 mA g^{-1}. Then, the hard carbon electrodes were recovered from the cells under Ar atmosphere, washed with DMC, and dried in a vacuum. A transfer vessel was used to transfer the electrodes into the XPS chamber without any contamination from air

4.3 Physicochemical properties

Figure 4.2 shows the ionic conductivities of $NaBPh_4$/DME and $NaPF_6$/DME. At a low concentration of <0.4 M, the ionic conductivity of $NaBPh_4$/DME was higher than that of $NaPF_6$/DME, suggesting the inherent high degree of dissociation for $NaBPh_4$ salt. With increasing concentration to above 0.4 M, the ionic conductivity of $NaBPh_4$/DME became lower than that of $NaPF_6$/DME because of the bulky BPh_4^- anion that leads to a short cation-anion mean distance, promoting ionic association.[26] The $NaBPh_4$/DME exhibited a maximum ionic conductivity of 6.3 mS cm^{-1} at 0.5 M, which is comparable to those of 0.5 M $NaPF_6$/DME (8.1 mS cm^{-1}) and 1 M $NaPF_6$/EC:DEC (9.0 mS cm^{-1}). On this basis, we chose the concentration of 0.5 M for $NaBPh_4$/DME in the following experiments.

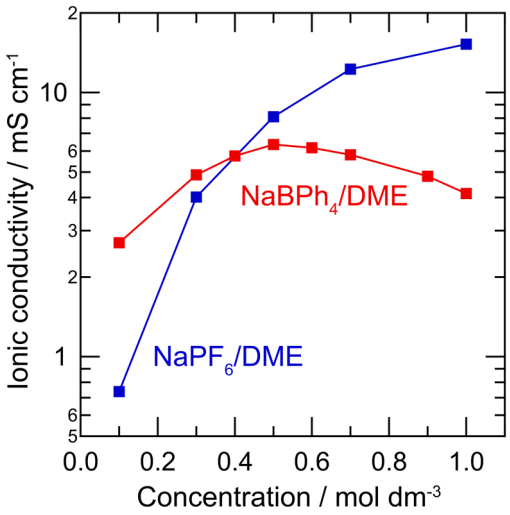

Figure 4.2 Concentration dependence of the ionic conductivities for $NaBPh_4$/DME and $NaPF_6$/DME at 25 °C.

4.4 Electrochemical stability

To study the cathodic and anodic stability of 0.5 M $NaBPh_4$/DME, CV and LSV tests were conducted on Cu and Pt electrodes, respectively (**Figure 4.3**). For the cathodic side, this electrolyte enabled reversible plating/stripping of sodium metal. The seemingly low reversibility as compared with a previous report[26] was caused by the separator-less three-electrode cell configuration, in which the plated sodium metal is not subjected to external pressure. Small reduction current was observed below 0.8 V (vs. Na/Na^+) only in the first cycle, which might have resulted from the formation of SEI or the decomposition of contaminants in the electrolyte or on the electrode. On the other hand, the anodic limit of 0.5 M $NaBPh_4$/DME was ca. 3.4 V (vs. Na/Na^+). Although this anodic limit is not high compared with conventional electrolytes (~ 4 V), the electrolyte also enabled the highly reversible charge-discharge reaction of a positive electrode ($Na_2V_3O_7$) with higher rate capability than 1 M $NaPF_6$/EC:DEC (1:1 by volume) (**Figure 4.4**).

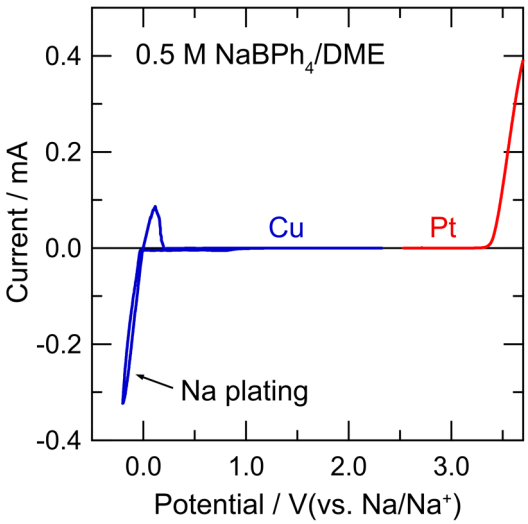

Figure 4.3 Electrochemical stability of 0.5 M $NaBPh_4$/DME as evaluated by LSV (red, scan rate: 0.1 mV s^{-1}) and CV (blue, scan rate: 0.1 mV s^{-1}) using Pt and Cu electrodes, respectively.

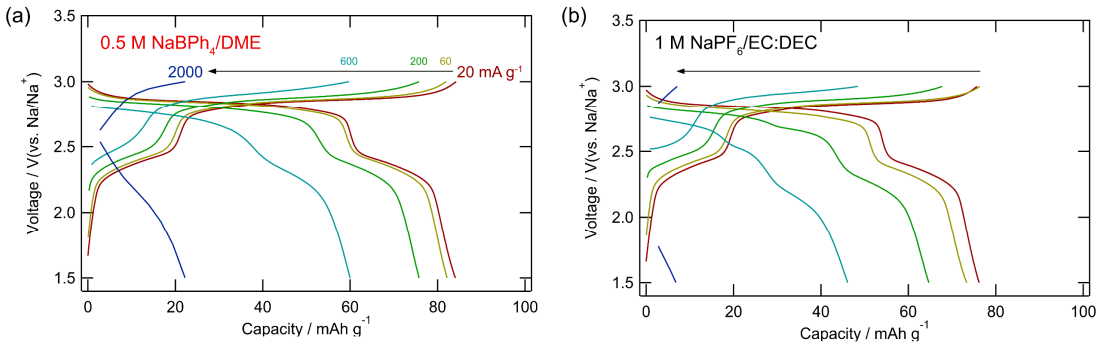

Figure 4.4 Charge–discharge profiles of $Na_2V_3O_7$ electrodes at current densities of 20–2000 mA g^{-1} with (a) 0.5 M $NaBPh_4$/DME and (b) 1 M $NaPF_6$/EC:DEC electrolytes. The theoretical capacity of $Na_2V_3O_7$ is ~173 mAh g^{-1} assuming two-electron transfers, but the practical capacity of the electrode is about 90 mAh g^{-1} in the voltage range of 1.5–3.5 V (vs. Na/Na^+).

4.5 Effect of Na salt on the cycling stability of hard carbon

First, I studied the charge-discharge cycling performance of hard carbon half cells using various Na salts in combination with a reduction-tolerant DME solvent (**Figure 4.6**). The results are summarized in **Table 4.1**. Notably, the 0.5 M $NaBPh_4$/DME electrolyte exhibited the highest initial Coulombic efficiency of 95.0% with high capacity retention of 95.6% over 100 cycles, suggesting the minimized reductive decomposition of the electrolyte components for forming a stable SEI.

Besides, the capacity of the plateau region close to 0 V was even larger than with 1 M $NaPF_6$/EC:DEC owing to the decreased polarization, hence, the formed interface has lower resistance. As for other salts, 0.5 M $NaPF_6$/DME exhibited high capacity retention of 95.7% during 100 cycles, but the average Coulombic efficiency during cycles was low (ca. 98.5%, Figure 4.6(c)), indicating that the SEI is less stable than that with $NaBPh_4$/DME. When 0.5 M NaFSA/DME and 0.5 M NaTFSA/DME were used, the charge-discharge reactions were unstable and less reversible, suggesting that these electrolytes could not form a stable interface. In NaFSA/DME, reversible sodiation/desodiation basically proceeded, but sometimes its voltage abruptly dropped during desodiation and did not reach the upper cut-off; this behavior is characteristic of some shuttling reactions between the electrodes arising from the unstable interfaces (**Figure 4.5**). In NaTFSA/DME, the reversible capacity was rapidly decreased during initial several cycles. In the cycled cell, the color of the Na metal and the separator was changed to yellow, suggesting extensive electrolyte decompositions at the Na metal as well as the hard carbon. On this basis, the counter anions of sodium salts dominate the interfacial stability of low-potential electrodes; importantly, the presence of fluorine species is not a sufficient condition for stabilizing the interface.

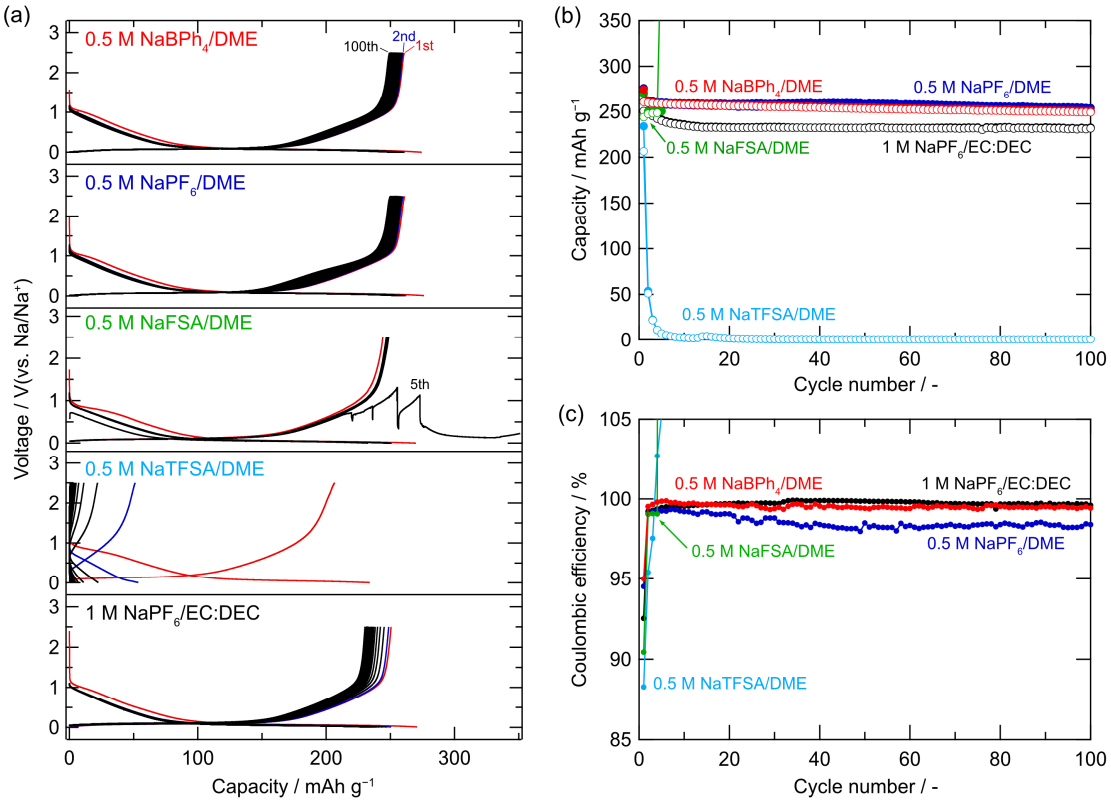

Figure 4.6 (a) Charge-discharge voltage profiles of hard carbon|Na metal half cells with various 0.5 M Na salt/DME electrolytes compared with a standard 1 M $NaPF_6$/EC:DEC (1:1 by volume) at a current density of 20 mA g^{-1}. (b) Capacity retention and (d) Coulombic efficiency of the half cells over 100 cycles.

Table 4.1 Electrochemical performance of the hard carbon electrodes with various electrolytes at a current density of 20 mA g^{-1}.

Electrolyte	1st discharge capacity / mAh g^{-1}	Initial Coulombic efficiency / %	Average Coulombic efficiency (100 cycles) / %	Capacity retention (100 cycles) / %
0.5 M $NaBPh_4$/DME	260.8	95.0	99.5	95.6
0.5 M $NaPF_6$/DME	261.0	94.5	98.5	95.7
0.5 M NaFSA/DME	244.1	90.4	-	-
0.5 M NaTFSA/DME	206.6	88.3	-	0.2
1 M $NaPF_6$/EC:DEC	250.5	92.5	99.6	92.5

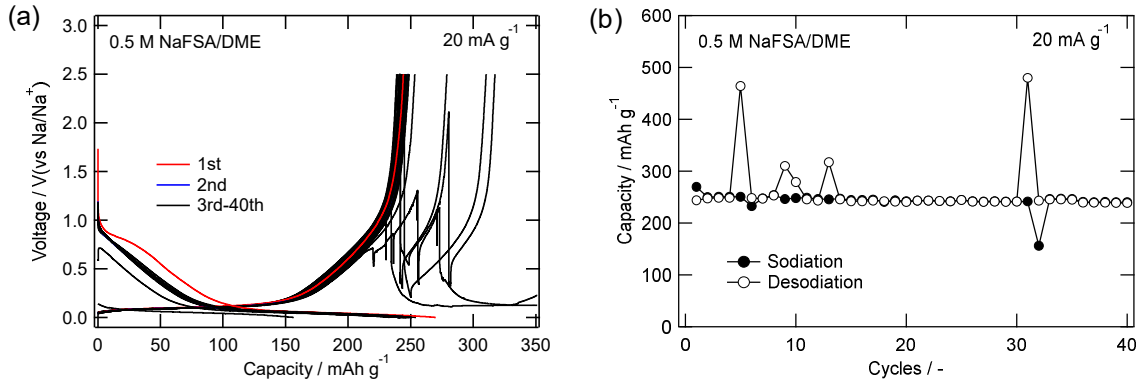

Figure 4.7 (a) Charge-discharge profiles and (b) capacity retention of a hard carbon|Na metal half cell with 0.5 M NaFSA/DME electrolyte over 40 cycles.

4.6 Effect of solvent on the reaction kinetics of hard carbon

Having found the high stability of $NaBPh_4$ salt, I next tested hard half cells using various electrolyte solvents with a focus on the reaction kinetics (**Figure 4.8**). Notably, 0.5 M $NaBPh_4$/DME could retain a high reversible capacity of over 200 mAh g^{-1} even at 6000 mA g^{-1} owing to low polarization (Figure 4.8(a)(b)), which is distinct from the almost zero capacity in conventional 1 M $NaPF_6$/EC:DEC. Besides, high capacity retention of over 82 % was observed after 1500 cycles at a current density of 1000 mA g^{-1} (Figure 4.8(c)). As for other solvents, a similar high-rate character was also observed in 0.5 M $NaBPh_4$/THF, whereas much poorer kinetics were observed for 0.5 M $NaBPh_4$/EC:DEC and SL, suggesting that the selection of ether solvents is effective for achieving high-rate performance.

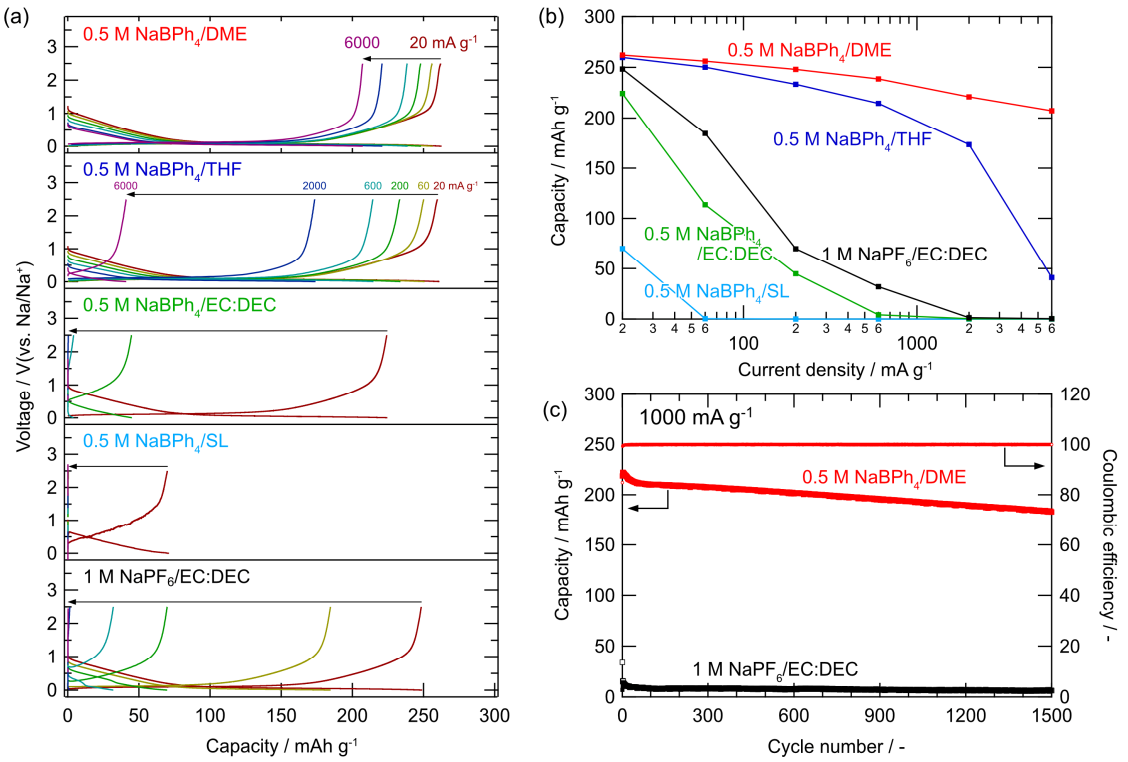

Figure 4.8 (a) Charge-discharge voltage profiles of hard carbon|Na metal half cells with various 0.5 M $NaBPh_4$ electrolytes as compared with a standard 1 M $NaPF_6$/EC:DEC (1:1 by volume) at increasing current densities from 20 mA g^{-1} to 6000 mA g^{-1}. (b) Reversible capacities of the half cells at various current densities. (c) Cycling performances of the half cells at a current density of 1000 mA g^{-1}.

To confirm that the high rate performance resulted from the hard carbon electrodes, we conducted an AC impedance measurement for hard carbon|hard carbon symmetric cells with various electrolytes. The hard carbon electrodes were charged in advance to 0.01 V in a half cell. As shown in **Figure 4.9**, the symmetric cells exhibit a small *Z*' intercept and two semicircles at high and middle-to-low frequency regions. An equivalent circuit corresponding to this system is shown in the inset. The *Z*' intercept is ascribed to the sum of the solution resistance of the electrolyte (R_{sol}) and the electronic resistance of the electrodes (R_e). The semicircles at high and middle-to-low frequency regions correspond to the resistance in SEI (R_{SEI}) and the charge-transfer resistance (R_{ct}), respectively. Notably, 0.5 M $NaBPh_4$/DME electrolyte resulted in smaller R_{ct} than 0.5 M $NaBPh_4$/EC:DEC. Hence, the observed high rate performance of the hard carbon half cell with 0.5

M $NaBPh_4$/DME did arise from low R_{ct} at the hard carbon/electrolyte interface. Based on the result, the combination of $NaBPh_4$ with ether solvents such as DME is essential for forming a stable and low-resistance interface.

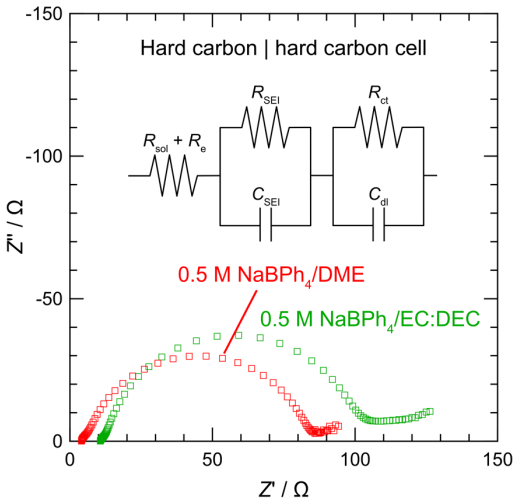

Figure 4.9 Nyquist plots of hard carbon|hard carbon symmetric cells with 0.5 M $NaBPh_4$/DME and 0.5 M $NaBPh_4$/EC:DEC (1:1 by volume). The hard carbon electrodes were in the charged state at 0.01 V. The inset shows an equivalent circuit for this system. The symbols C_{SEI} and C_{dl} denote capacitive elements in the SEI and the electric double layer, respectively.

4.7 Interphasial chemistry

For further insights into the stable and low-resistance interface, the interphasial chemistry on the cycled hard carbon was investigated via XPS (**Figure 4.10**). On the hard carbon cycled in 1 M $NaPF_6$/EC:DEC or 0.5 M NaTFSA/DME electrolytes, NaF was detected as an SEI component. Moreover, sulfides were formed as an SEI component in 0.5 M NaTFSA/DME. These results suggest that $NaPF_6$ and NaTFSA are decomposed during the cycle to provide some SEI components. However, considering the poor cycling performance in NaTFSA/DME electrolyte, the presence of NaF or sulfides is not a sufficient condition for stabilizing the interface, unless they are formed densely, for example, using concentrated electrolytes.[26,33] On the other hand, in $NaBPh_4$/DME

electrolyte, only negligible amounts of B compound, as well as F and S compounds, were detected as SEI components. Hence, $NaBPh_4$ is not decomposed on hard carbon negative electrodes during cycling. Instead, the C1s spectrum changed significantly compared with other electrolytes, suggesting the contribution of DME solvent to forming the SEI, although its detailed composition is not clear at present. This DME-derived SEI, though containing negligible amounts of F component, can stabilize the interface in $NaBPh_4$/DME electrolyte, thus leading to the stable cycling of hard carbon electrodes.

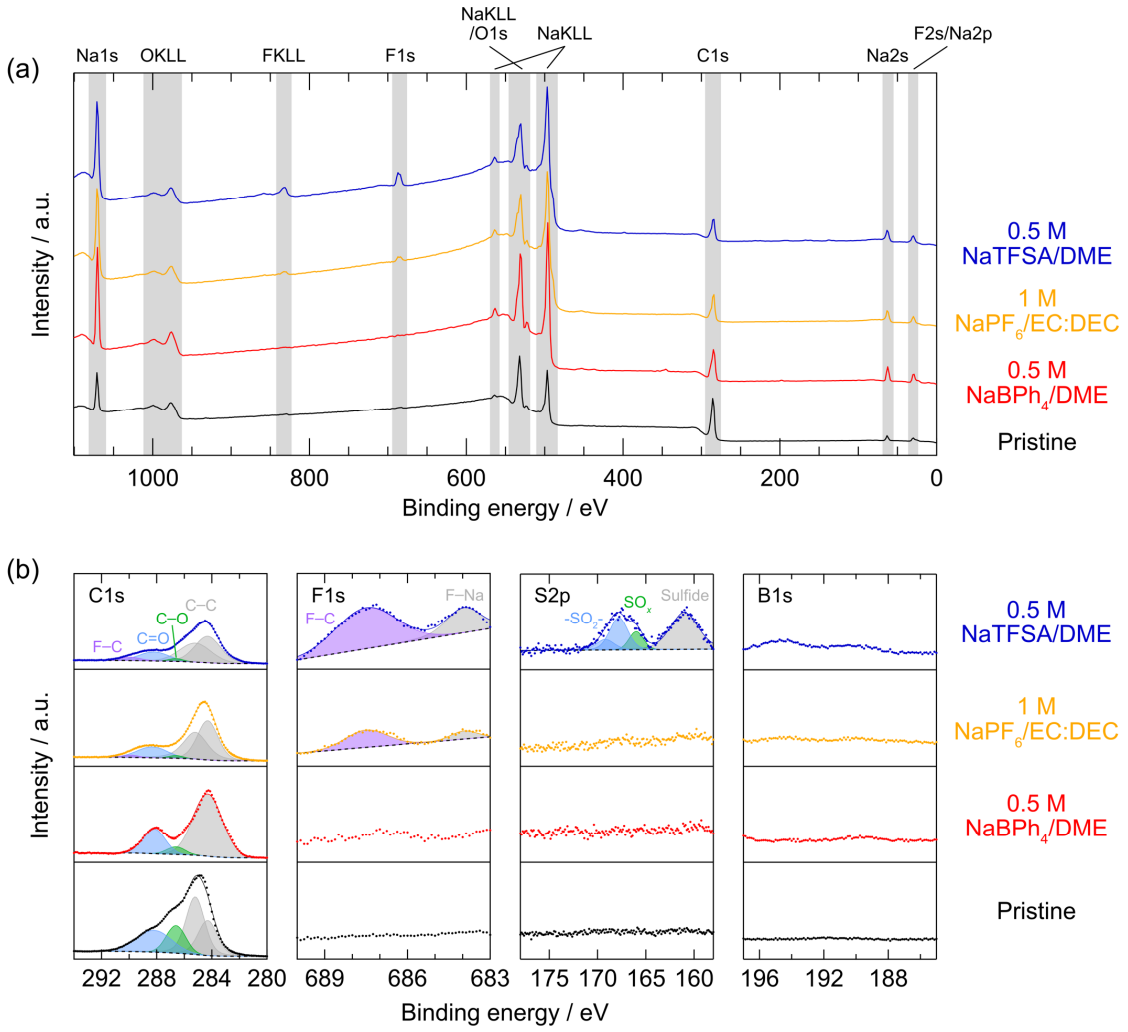

Figure 4.10 (a) Wide-scan and (b) C1s, F1s, S2p, and B1s XPS spectra of the hard carbon electrodes after three cycles at a current density of 20 mA g^{-1} in 1 M $NaPF_6$/EC:DEC, 0.5 M $NaBPh_4$/DME, and 0.5 M NaTFSA/DME electrolytes. The XPS spectra of hard carbon electrode without charge–discharge cycles ("pristine") are also shown as a reference. A small amount of fluorine-derived peak

may be detected in the F1s spectrum of 0.5 M $NaBPh_4$/DME. We could not rule out the possibility of fluorine contamination from sodium metal (purity 98%) at the counter electrode.

To obtain further knowledge about SEI, cycled electrodes were investigated via infrared spectroscopy (IR). The results were shown in **Figure 4.11**. C-H stretching mode and C=O stretching mode were observed, indicating that SEI contains organic components. Further, it can be seen that the composition differs depending on the electrolyte.

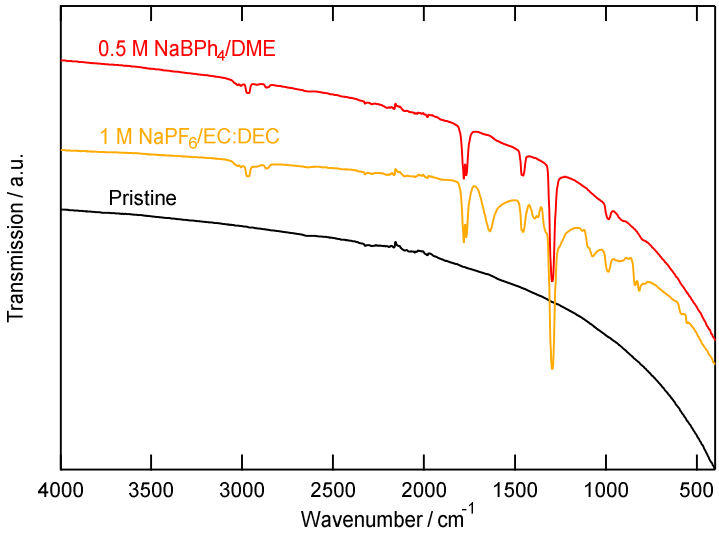

Figure 4.11 IR spectra of the hard carbon electrodes after 115 cycles.

Figure 4.12 shows the XPS depth profiles of the cycled hard carbon electrodes in 1 M $NaPF_6$/EC:DEC, 0.5 M $NaBPh_4$/DME. In both electrolytes, the intensity of C=O peak on the C1s spectra and that of Na1s peak increased with the etching time. In 1 M $NaPF_6$/EC:DEC, the peak of F-C bond on the F1s spectra disappeared by etching, but F-Na peak was maintained at the longer etching time. Since the pristine hard carbon electrode does not contain F (Figure 4.8(b)), it is considered that the SEI formed in 1 M $NaPF_6$/EC:DEC was not completely removed by etching for 90 minutes. In 0.5 M $NaBPh_4$/DME, no B1s peak was detected even if the analysis proceeded in the depth direction, and it was reconfirmed that $NaBPh_4$ was not decomposed during cycling. In

Figure 4.12(b), the XPS spectrum shape changed for the first several tens of minutes, but the shape hardly changed after that. Although the composition is thought to be constant after a certain depth, it was different from that of pristine even after 90 minutes of etching. The composition at the deep position had a particularly high Na content compared to pristine. There are two possibilities: (i) 90 minutes of etching is not enough to reach the surface of the hard carbon electrode, or (ii) there are sodium atoms left in the hard carbon even after discharge (desodiated state), or (iii) SEI on the side surface continues to be detected even after sputtering because hard carbon is spherical.

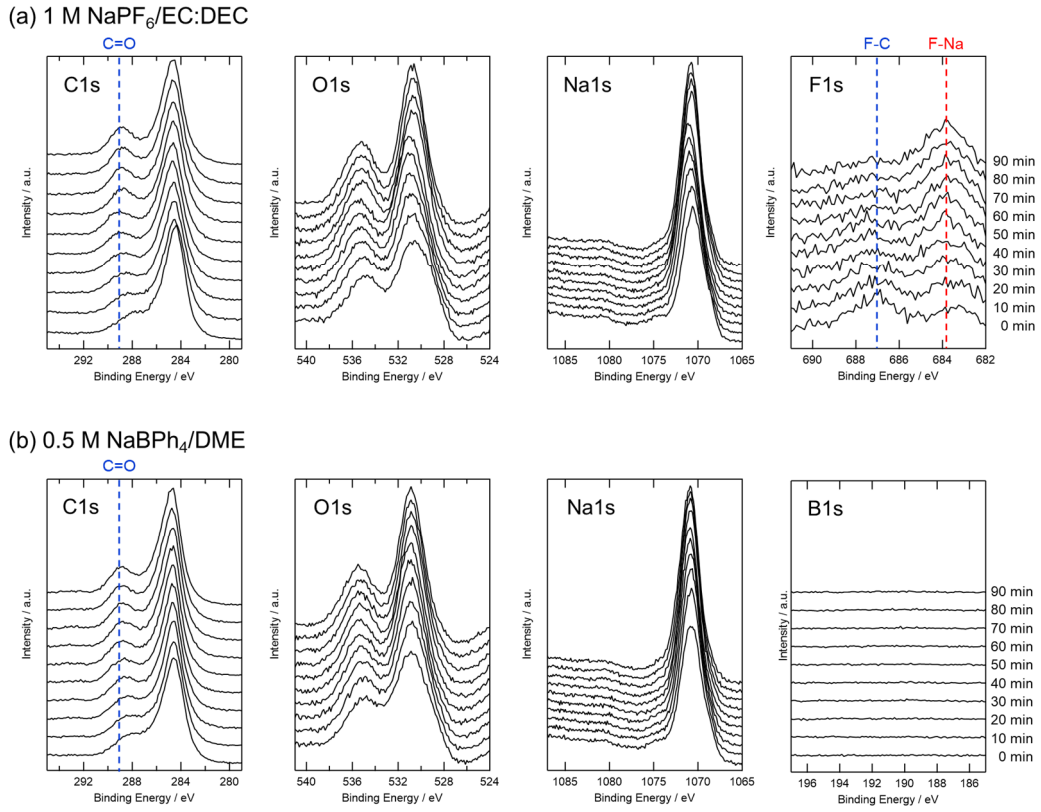

Figure 4.12 XPS spectra of the hard carbon electrodes after three cycles at a current density of 20 mA g^{-1} in (a) 1 M $NaPF_6$/EC:DEC, (b) 0.5 M $NaBPh_4$/DME. The depth profiles were obtained via Ar^+ sputtering at 1 kV for 10−90 min.

In order to analyze only SEI, the copper foil was swept for 5 cycles in the range of 0.01 to 2.5 V in two kinds of electrolytes to form SEI on the copper foil. **Figure 4.13** shows the XPS depth profiles of polarized Cu foils in 1 M $NaPF_6$/EC:DEC, 0.5 M $NaBPh_4$/DME. In $NaPF_6$/EC:DEC, O

and Na components still remained after 6 minutes of sputtering, but almost no SEI component was detected in $NaBPh_4$/DME. It is suggested that the SEI formed in $NaBPh_4$/DME is thinner or softer. For a more detailed analysis, another analytical method such as transmission electron microscope (TEM) observation should be employed.

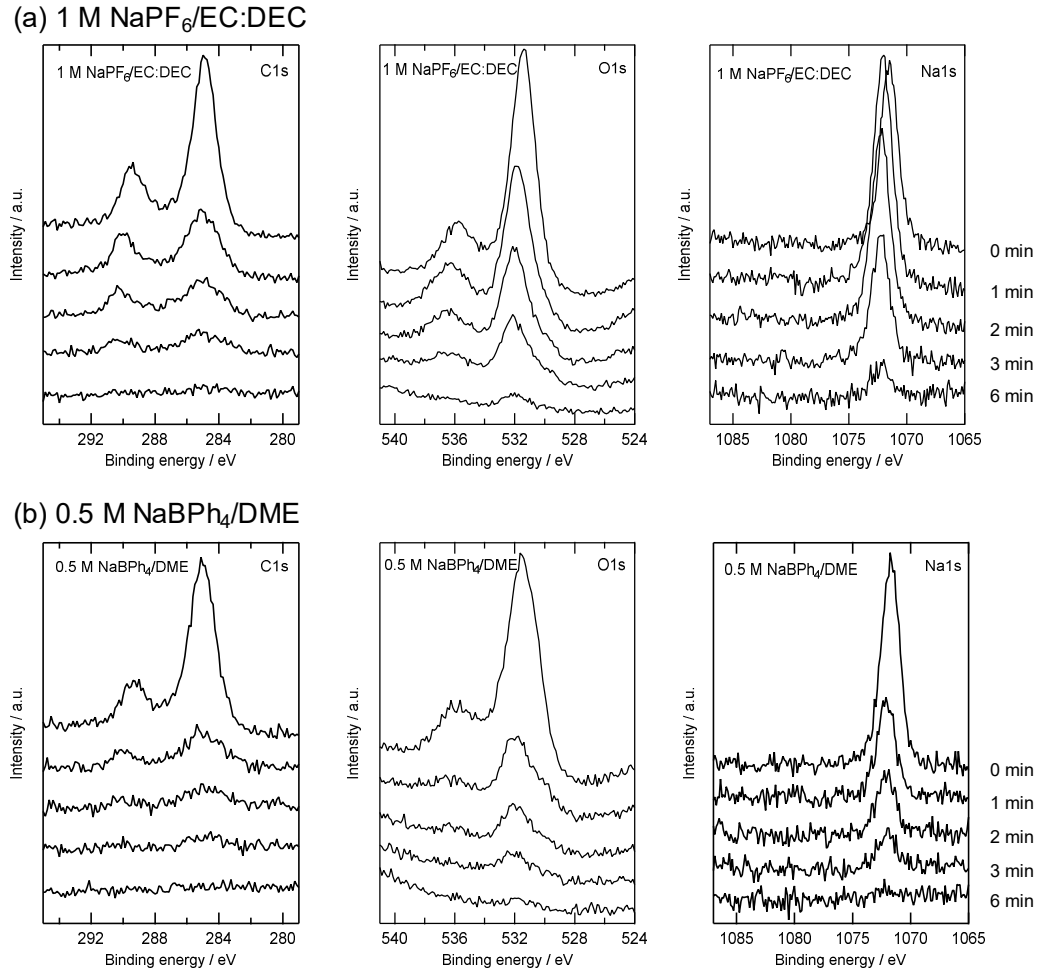

Figure 4.13 XPS spectra of reductively polarized Cu foils in (a) 1 M NaPF6/EC:DEC, (b) 0.5 M NaBPh4/DME. The depth profiles were obtained via Ar^+ sputtering at 1 kV for 1−6 min.

Figure 4.14 shows the SEM images of the pristine and cycled hard carbon electrodes. Only hard carbon particles were observed on the pristine electrode, but deposits other than hard carbon were observed on the electrode surface 1 M $NaPF_6$/EC:DEC (Figure 4.14(d), (e)). The deposit is presumed to be a decomposition product of the electrolyte. On the other hand, no such deposit was

not observed on the electrode surface cycled in 0.5 M $NaBPh_4$/DME. It is suggested that SEI is uniformly formed on the hard carbon surface in $NaBPh_4$/DME electrolyte.

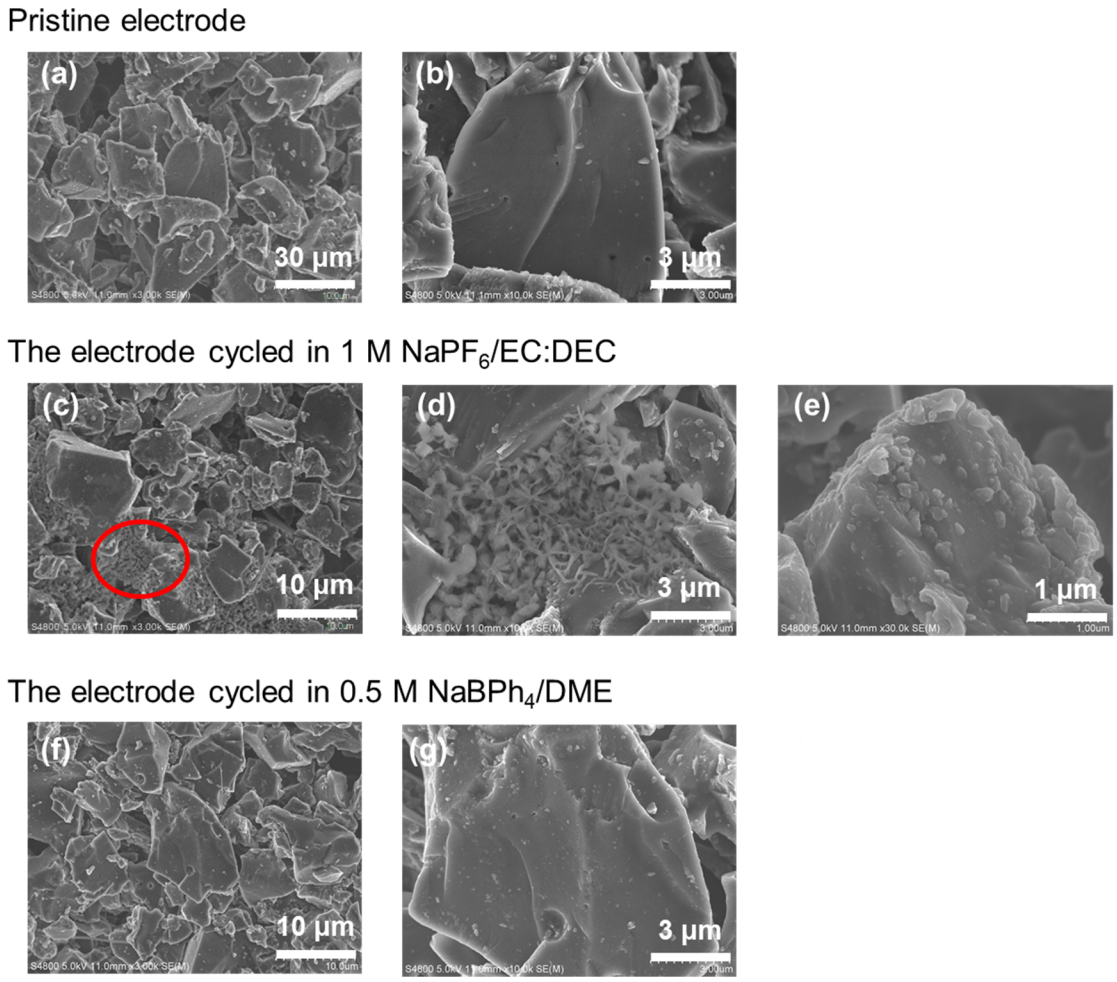

Figure 4.14 SEM images of the hard carbon electrodes. (a), (b) Pristine electrode, (c)–(e) the electrode charge and discharged in 1 M $NaPF_6$/EC:DEC for three cycle, and (f), (g) the electrode cycled in 0.5 M $NaBPh_4$/DME. The red circle mark the decomposed products of electrolyte on the electrode surface.

Figure 4.15 shows SEM images of the hard carbon electrodes after 115 cycles. For the electrode cycled in 1 M $NaPF_6$/EC:DEC, almost all of the electrode surface is covered with decomposed products. On the other hand, for the electrode cycled in 0.5 M $NaBPh_4$/DME, hard carbon particles can be seen. It is suggested that excessive decomposition is suppressed by the decomposition product being uniformly deposited on the electrode surface.

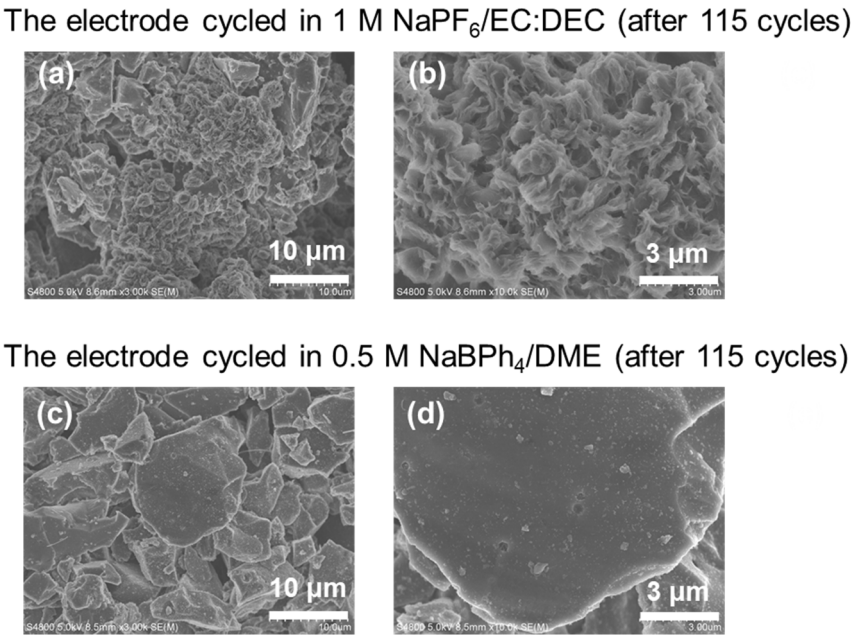

Figure 4.15 Surface morphology of hard carbon electrodes after 115 cycles at a current density of 20 mA g^{-1} in (a), (b) 1 M $NaPF_6$/EC:DEC and (c), (d) 0.5 M $NaBPh_4$/DME.

As shown previously,[26] the DME-derived SEI, composed of carbon, oxygen, and sodium elements, is stable and highly Na^+-conductive. Hence, it does not need any other component from counter anions for stabilizing the interface. More preferably, the counter anions should be highly tolerant of reductive decomposition possibly even at the low reaction potential (~0 V vs. Na/Na^+) of hard carbon electrodes to minimize the loss of Coulombic efficiency. From this perspective, BPh_4^- anion has a remarkably lower electron affinity than other anions,[26] and is thus more tolerant to reduction. Hence, among the several sodium salts studied, $NaBPh_4$ is the most favorable for use in combination with DME that enables the highly stable and high-rate cycling of such low-potential negative electrodes.

4.8 Conclusion

The highly reversible and high-rate charge-discharge cycling of hard carbon negative electrodes

was demonstrated in a fluorine-free electrolyte of 0.5 M $NaBPh_4$/DME electrolyte. Based on the comparative study of various salts in DME, the $NaBPh_4$ electrolyte can stabilize the hard carbon/electrolyte interface better than other fluorinated salts, such as $NaPF_6$, NaFSA, and NaTFSA, suggesting that fluorine components are not indispensable in SEI to stabilize the interface. On the other hand, the selection of solvent is important to fully exert the potential of $NaBPh_4$. Ether solvents (*i.e.*, DME and THF) enable remarkably better reaction kinetics than carbonate or sulfone, suggesting low interfacial resistance in $NaBPh_4$/ether electrolytes. The surface analysis of the cycled hard carbon electrodes shows that $NaBPh_4$ is not subjected to reductive decomposition during cycling and that the SEI is derived from ether solvent. With all things considered, the ether-derived SEI, though containing no fluorine component, is inherently stable and has low resistivity, thus, the combination of ether solvent with reduction-tolerant $NaBPh_4$ salt is the most effective one to achieve highly reversible and high-rate cycling of hard carbon negative electrodes. This work elucidated the role of salt and solvent in forming a stable SEI on hard carbon, providing a guideline for designing an electrolyte for sodium-ion batteries.

References

1. Berthelot, R., Carlier, D. & Delmas, C. Electrochemical investigation of the P2-NaxCoO2 phase diagram. *Nat. Mater.* **10**, 74–80 (2011).
2. Yabuuchi, N. *et al.* P2-type Nax[Fe1/2Mn1/2]O2 made from earth-abundant elements for rechargeable Na batteries. *Nat. Mater.* **11**, 512–517 (2012).
3. Barpanda, P. *et al.* Sodium iron pyrophosphate: A novel 3.0 v iron-based cathode for sodium-ion batteries. *Electrochem. commun.* **24**, 116–119 (2012).
4. Stevens, D. A. & Dahn, J. R. High Capacity Anode Materials for Rechargeable Sodium-Ion Batteries. *J. Electrochem. Soc.* **147**, 1271 (2000).
5. Komaba, S. *et al.* Electrochemical Na Insertion and Solid Electrolyte Interphase for Hard-Carbon Electrodes and Application to Na-Ion Batteries. *Adv. Funct. Mater.* **21**, 3859–3867 (2011).
6. Yamamoto, H. *et al.* Synthesizing higher-capacity hard-carbons from cellulose for Na- and K-ion batteries. *J. Mater. Chem. A* **6**, 16844–16848 (2018).
7. Dahbi, M. *et al.* Synthesis of hard carbon from argan shells for Na-ion batteries. *J. Mater. Chem. A* **5**, 9917–9928 (2017).
8. Hasegawa, G. *et al.* Hard Carbon Anodes for Na-Ion Batteries: Toward a Practical Use. *ChemElectroChem* **2**, 1917–1920 (2015).
9. Hasegawa, G. *et al.* Studies on electrochemical sodium storage into hard carbons with binder-free monolithic electrodes. *J. Power Sources* **318**, 41–48 (2016).
10. Takada, K. *et al.* Unusual Passivation Ability of Superconcentrated Electrolytes toward Hard Carbon Negative Electrodes in Sodium-Ion Batteries. *ACS Appl. Mater. Interfaces* **9**, 33802–33809 (2017).
11. Dahbi, M. *et al.* Effect of Hexafluorophosphate and Fluoroethylene Carbonate on Electrochemical Performance and the Surface Layer of Hard Carbon for Sodium-Ion Batteries. *ChemElectroChem* **3**, 1856–1867 (2016).
12. Fuentes, I., Andrio, A., Teixidor, F., Viñas, C. & Compañ, V. Enhanced conductivity of sodium versus lithium salts measured by impedance spectroscopy. Sodium cobaltacarboranes as electrolytes of choice. *Phys. Chem. Chem. Phys.* **19**, 15177–15186 (2017).
13. Zhu, Y.-E. *et al.* Boosting the rate capability of hard carbon with an ether-based electrolyte for sodium ion batteries. *J. Mater. Chem. A* **5**, 9528–9532 (2017).
14. Zhang, J. *et al.* Achieving superb sodium storage performance on carbon anodes through an ether-derived solid electrolyte interphase. *Energy Environ. Sci.* **10**, 370–376 (2017).
15. Peled, E. The Electrochemical Behavior of Alkali and Alkaline Earth Metals in Nonaqueous Battery Systems—The Solid Electrolyte Interphase Model. *J. Electrochem. Soc.* **126**, 2047–2051 (1979).
16. Peled, E., Golodnitsky, D. & Ardel, G. Advanced model for solid electrolyte interphase

electrodes in liquid and polymer electrolytes. *J. Electrochem. Soc.* **144**, (1997).

17. Seh, Z. W., Sun, J., Sun, Y. & Cui, Y. A Highly Reversible Room-Temperature Sodium Metal Anode. *ACS Cent. Sci.* **1**, 449–455 (2015).
18. Zheng, J. *et al.* Extremely Stable Sodium Metal Batteries Enabled by Localized High-Concentration Electrolytes. *ACS Energy Lett.* **3**, 315–321 (2018).
19. Cao, R. *et al.* Enabling room temperature sodium metal batteries. *Nano Energy* **30**, 825–830 (2016).
20. Lee, J. *et al.* Ultraconcentrated sodium bis(fluorosulfonyl)imide-based electrolytes for high-performance sodium metal batteries. *ACS Appl. Mater. Interfaces* **9**, 3723–3732 (2017).
21. Komaba, S. *et al.* Fluorinated ethylene carbonate as electrolyte additive for rechargeable Na batteries. *ACS Appl. Mater. Interfaces* **3**, 4165–4168 (2011).
22. de la Llave, E. *et al.* Study of the Most Relevant Aspects Related to Hard Carbons as Anode Materials for Na-ion Batteries, Compared with Li-ion Systems. *Isr. J. Chem.* **55**, 1260–1274 (2015).
23. Vogt, L. O. *et al.* Understanding the interaction of the carbonates and binder in Na-ion batteries: A combined bulk and surface study. *Chem. Mater.* **27**, 1210–1216 (2015).
24. Scheers, J. *et al.* All fluorine-free lithium battery electrolytes. *J. Power Sources* **251**, 451–458 (2014).
25. Han, J., Zhang, H., Varzi, A. & Passerini, S. Fluorine-Free Water-in-Salt Electrolyte for Green and Low-Cost Aqueous Sodium-Ion Batteries. *ChemSusChem* **11**, 3704–3707 (2018).
26. Doi, K. *et al.* Reversible Sodium Metal Electrodes: Is Fluorine an Essential Interphasial Component? *Angew. Chemie Int. Ed.* **58**, 8024–8028 (2019).
27. Andersson, P., Blomqvist, P., Lorén, A. & Larsson, F. Using Fourier transform infrared spectroscopy to determine toxic gases in fires with lithium-ion batteries. *Fire Mater.* **40**, 999–1015 (2016).
28. Bertilsson, S., Larsson, F., Furlani, M., Albinsson, I. & Mellander, B. E. Lithium-ion battery electrolyte emissions analyzed by coupled thermogravimetric/Fourier-transform infrared spectroscopy. *J. Power Sources* **365**, 446–455 (2017).
29. Eshetu, G. G. *et al.* Fire behavior of carbonates-based electrolytes used in Li-ion rechargeable batteries with a focus on the role of the LiPF6 and LiFSI salts. *J. Power Sources* **269**, 804–811 (2014).
30. Wilken, S., Johansson, P. & Jacobsson, P. Infrared spectroscopy of instantaneous decomposition products of LiPF 6-based lithium battery electrolytes. in *Solid State Ionics* vol. 225 608–610 (2012).
31. Niitaka, S., Yoshimura, K., Ikawa, A. & Kosuge, K. Magnetism of Na2V3O7 with Nano-Tube Structure. *J. Phys. Soc. Japan* **71**, 208–210 (2002).

32. Tanibata, N. *et al.* Nanotube-structured Na2V3O7 as a Cathode Material for Sodium-Ion Batteries with High-rate and Stable Cycle Performances. *Sci. Rep.* **8**, (2018).
33. Schafzahl, L., Hanzu, I., Wilkening, M. & Freunberger, S. A. An Electrolyte for Reversible Cycling of Sodium Metal and Intercalation Compounds. *ChemSusChem* **10**, 401–408 (2017).

5 General conclusion and future perspectives

5.1 Conclusions of this thesis

This thesis focuses on hard carbon as anode material for sodium-ion batteries (NIBs) because hard carbon is regarded as one of the most promising sodium-ion host due to its large capacity, relatively low redox potential and good cycling stability. Looking at the practical application of NIBs, it is essential to analyze the sodium storage mechanism of hard carbon and improve the performance as an anode material (*e.g.*, high capacity, high rate capability, high safety, low redox potential, high initial coulombic efficiency).

In Chapter 2, hard carbon suitable for reaction mechanism analysis was synthesized. There were three requirements for the hard carbon: high initial coulomb efficiency (ICE, > 90%), large capacity (> 300 mAh g^{-1}), and large-scale synthesis. Since a relatively small surface area and a high yield can be expected, saccharides were used as raw materials, and hydrothermal treatment followed by carbonization treatment at a high temperature was used as a synthesis method. The author discovered that the number of nanopores in hard carbon can be dramatically increased by synthesizing from a mixture of two types of monosaccharides at an appropriate ratio. By optimizing the raw material and synthesis conditions, high ICE (95.2%) and large reversible capacity (348 mAh g^{-1}) were achieved.

Subsequently, to investigate the correlation between microstructures and the sodium storage properties of hard carbon, a series of nanostructured hard carbon samples were synthesized using the method presented in Chapter 2 and were analyzed by combined *ex situ* SAXS/WAXS experiments. An *ex situ* analytical method that maintains a highly inert atmosphere during measurement was developed and applied. As a result, the author revealed the following three things: the threshold distance between layers allowing sodium insertion (3.6 Å), the high density of sodium atoms stored in the nanopores (comparable to bcc sodium metal), and a reason for reducing the plateau capacity by heat treatment at too high temperature. Importantly, for the first time, I have

succeeded in detecting a broad peak in the WAXS pattern as a signature of sodium insertion into the nanopores, and its origin was analyzed to be the atomic correlation of sodium in the nanopores using DFT-MD simulations.

To improve a poor rate performance of hard carbon, an electrolyte that elicits the performance of hard carbon was investigated in Chapter 4. The authors discovered that 0.5 M $NaBPh_4$/DME electrolyte enables high initial coulombic efficiency, highly stable charging and discharging, and outstanding rate capability of hard carbon electrodes without any special additives or binders. As a result of analyzing the electrode surface after cycling, it was found that $NaBPh_4$ was not decomposed during the cycling, and that solid electrolyte interphase was composed only of components derived from DME. It is considered that the reduction stability of salt and solvent is the key to the stable operation of anode materials.

5.2 Future directions

In the present thesis, the authors developed an *ex situ* analysis method that enabled detailed analysis of highly reactive materials, and applied it to hard carbon with various structures. As a result, the correlation between microstructures and the sodium storage properties is comprehensively understood. In addition, it was demonstrated that hard carbon can be operated stably even with a fluorine-free electrolyte, and a new design guideline for the electrolyte was obtained. Therefore, the author will describe future research directions in the following sections.

5.2.1 Application of the developed analytical method to other materials

The author believes this method can be applied to other easily damaged materials. In fact, this method has already been applied to reaction mechanism analysis of a material called MXene (Nb_2CT_x, T_x is the functional termination group) in our laboratory. In *ex situ* measurement of sodiated MXene, which is easily damaged by moisture in air, high-quality data with good S/N ratio

without damage was obtained. Furthermore, the characteristic scattering peak in the WAXS pattern identified in this study can be utilized for the identification of the densely confined sodium in nanospaces, not only in hard carbon samples but also in other nanoporous materials.

5.2.2 Optimal structure of hard carbon and its synthesis method

The optimal structure of hard carbon should have the following:

(i) Many defects

(ii) Many nanopores with a diameter of about 20 Å (large porosity)

(iii) An average interlayer distance larger than 3.6 Å

(iv) A small active surface (where electrolyte can contact or penetrate and SEI can be formed) area and few functional groups on surface

Defects, interlayer distance, nanopore size, surface area, and functional groups can all be changed by heat treatment, so it is difficult to obtain an optimal structure only by heat treatment. Furthermore, (i) and (iii) are related to each other, and it is considered that a wide interlayer is formed due to the presence of a defect. Therefore, it is not easy to form an ideal microstructure. One solution is carbonizing plants to use their original microstructure. When waste (*e.g.*, banana peels, rice husks, nut shells) is used as raw materials, it would also solve environmental problems. However, as Edison tried 1200 kinds of bamboo as the bulb filament and found that the best one was Japanese bamboo, this strategy is powerful but has the drawbacks of requiring a huge number of trials and poor reproducibility. Another solution is to chemically create the microstructure. For example, it has been reported that (i) can be realized by chemical oxidation and subsequent chemical reduction, and (iv) can be realized by performing reduction treatment with hydrogen. (ii) can be accomplished by making nanopores using metal nanoparticles as a template, or by using mixed sugar as a raw material as in this thesis. In a normal electrode material, the void does not contribute to the capacity, so that a large porosity causes a reduction in the capacity per volume. However, in

the case of hard carbon, sodium can be stored in the nanopore at almost the same density as metallic sodium, so that even if the porosity is large, the energy density does not decrease. Combining these methods to create an optimal structure followed by tuning by heat treatment is considered the best synthesis method.

This is the first report that the performance of hard carbon can be improved by mixing multiple types of sugars. Since there are many types of saccharide other than the three types used in this thesis, the number of potentials is enormous, and there is a possibility that higher-performance hard carbon can be synthesized.

5.2.3 New electrolyte design

Evidence that a hard carbon can be stably operated even with a fluorine-free electrolyte by appropriately combining a salt and solvent having a high reduction stability was obtained. Moreover, ether solvents are known to have high reduction tolerance and to form thin and stable SEI on the negative electrode surface. Therefore, a new functional fluorine-free electrolyte can be developed by combining a salt such as sodium tetrafluoroborate ($NaBF_4$), which is expected to have high reduction stability, with an ether solvent such as DME, diglyme, triglyme or THF. These super-concentrated electrolytes and systems obtained by diluting them with another solvent are also targets for research.

Appendix A: The procedure of deconvolution analyses and background subtraction

Figures A1a–c show the raw data of Figures 3.13a–c that backgrounds are not subtracted. Since the peak intensity of hard carbon is weak, the raw data contains a lot of scattering derived from capillary (Figure A1d). Detail procedures of background subtraction and deconvolution analyses are described below.

1. The WAXS pattern of an empty capillary was measured as a background (Figure A1d).
2. The sample filling rate was calculated from the X-ray transmittance of the capillary of each sample.
3. Based on the filling rate, a coefficient k ($0 < k < 1$) to be multiplied with the background data was calculated.
4. As can be seen from Figure A1a–d, the broad peak of the capillary overlaps with the peak of the interlayer correlation of hard carbon. Since the degree of subtracting the background greatly affects the shape and position of the peak, three levels of background subtraction were performed using coefficients ($k - 0.03$, k, $k + 0.03$). The main cause of error bars in Figures. 3.13d and 3.16b was that fitting was performed using three background levels.
5. The background subtracted data was normalized based on the intensity of the (100) and (101) diffraction peaks.
6. Fitting was performed on the normalized data using 1–3 pseudo-Voigt functions and 1 linear model by lmfit. The examples of fitting results are shown in the Figures A1ef.
7. Based on the fitting result, the integrated intensity of each peak was computed to calculate I_{WAXS}. The interlayer distance was also calculated based on the fitting result.

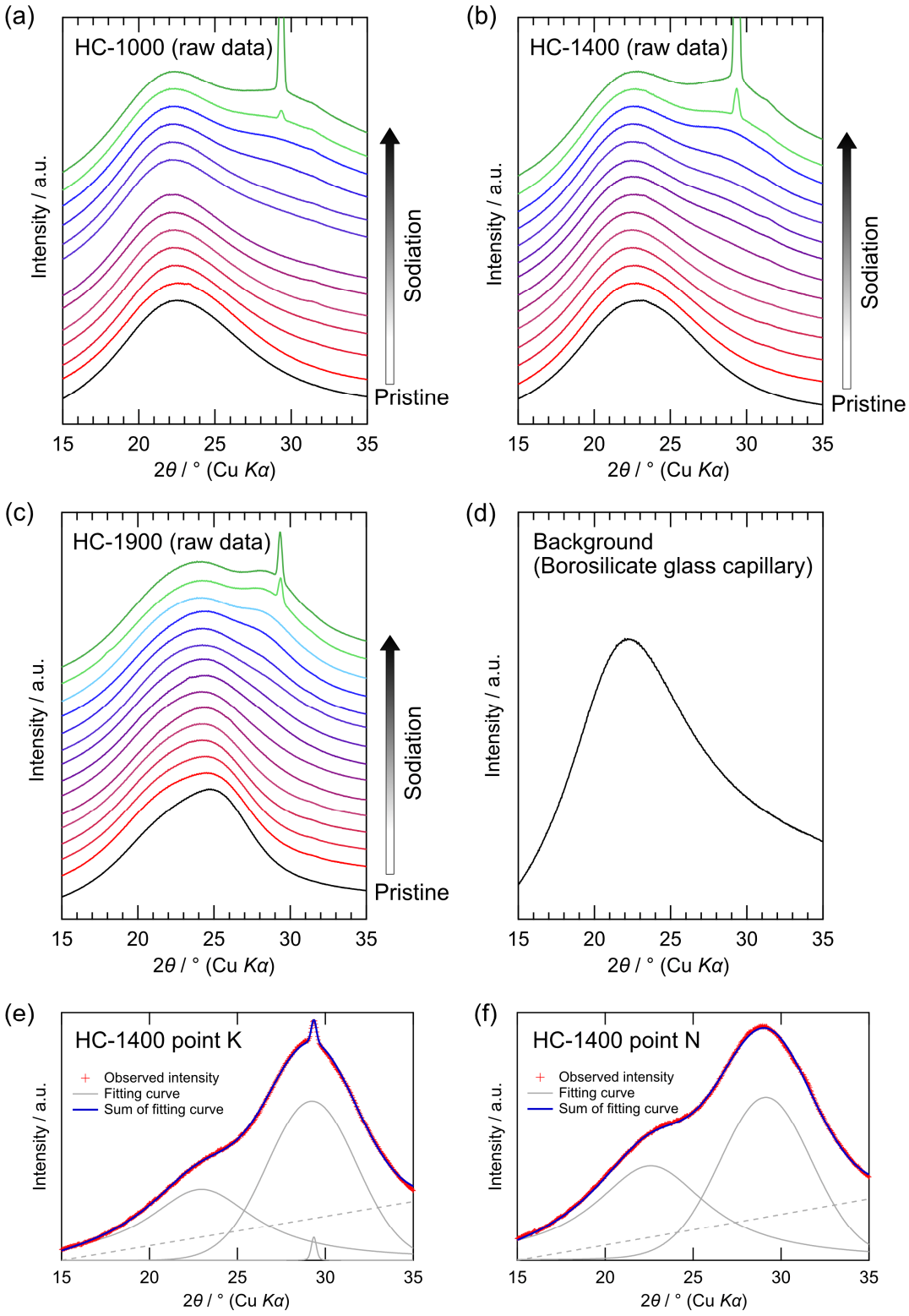

Figure A1 (a)–(c) Raw WAXS patterns of HC-1000, HC-1400 and HC-1900. (b) WAXS pattern of borosilicate glass capillary (background). (b)(c) The fitting results of HC-1400 electrodes (point K&N).

Appendix B: Li adsorption potential on graphene defects

Similar to section 3.6, the adsorption potential on the graphene defects was calculated for Li. The adsorption potential of lithium at each site was calculated based on following formula:

$$V = -(E_{\text{Lithium-surf}} - E_{\text{Surf}} - E_{\text{Lithium}})$$

Here, $E_{\text{Lithium-surf}}$ is the total energy when lithium is adsorbed on defective graphene, E_{Surf} is the total energy of defective graphene, and E_{Lithium} is the total energy of lithium. As is the case with sodium, the adsorption potentials of lithium on defect-free graphene were calculated to be −0.25 V (vs. Li/Li^+).

Figure B1 shows the calculation result of adsorption potential. Lithium showed almost the same result as sodium. In MV graphene the adsorption potential at O_1 and O_2 are the same because the lithium atom arranged on O_2 move to O_1 during structural relaxation. The results indicates that defects in graphene cause adsorption reactions to high potentials in LIBs.

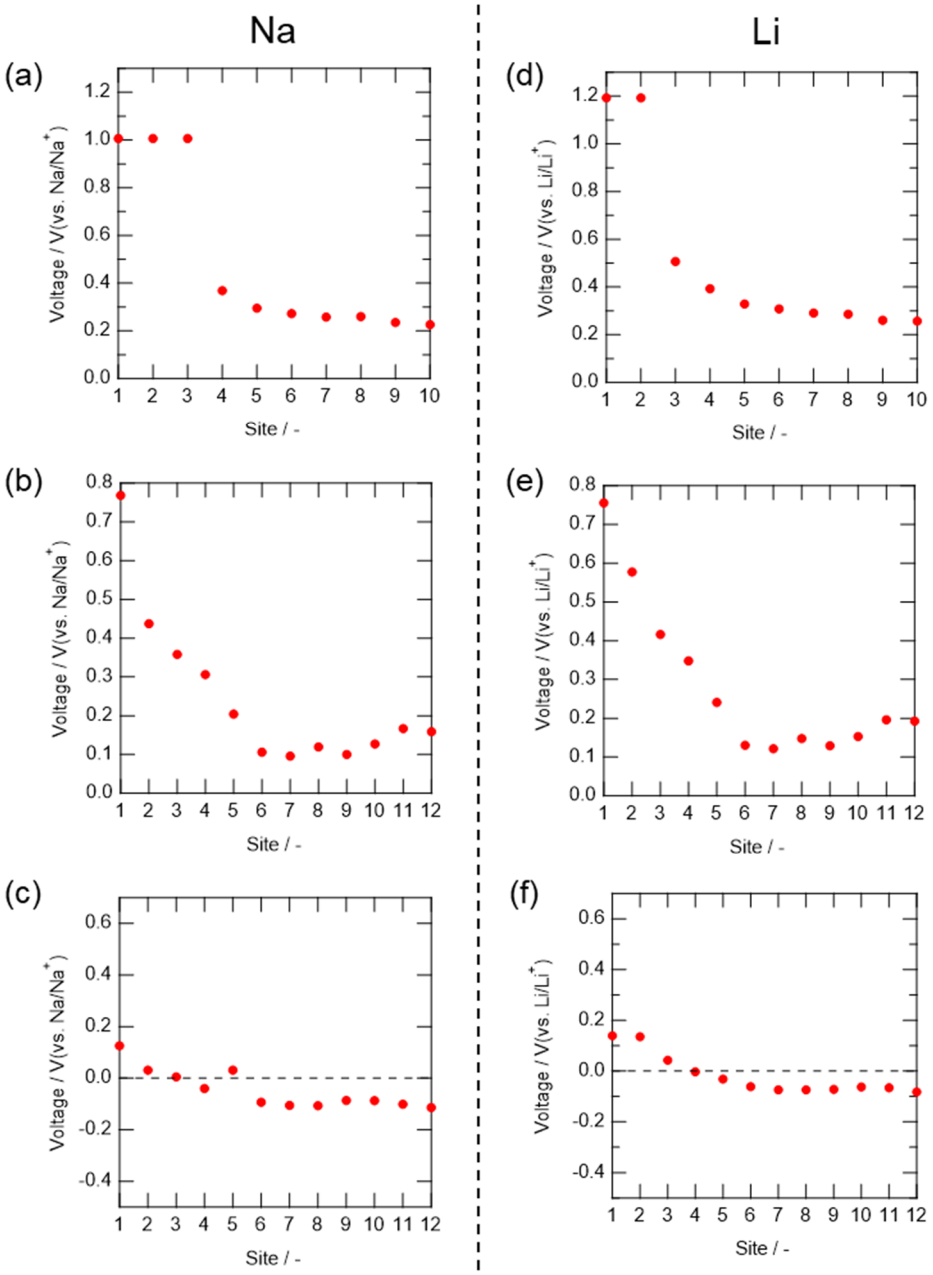

Figure B1 The adsorption potential of (a), (d) MV, (b), (e) DV, (c), (f) SW graphene. (a)–(c) and (d)–(f) are the results of Na adsorption and Li adsorption, respectively. (a)–(c) reprints Figure 3.22(a)–(c).

Acknowledgements

I would like to express my sincere gratitude to my supervisor, Professor Atsuo Yamada, for his fruitful suggestions and support throughout my master's and doctoral course. Despite my slow progress, he kept watch over me patiently and warmly until I achieved results. In particular, since the research presented in Chapters 2 and 3 has taken almost four years, the thesis would not have been completed without his patience. He taught me not only about research, but also how to create effective presentation materials and write high-quality papers. He took the time to revise my text thoroughly. Thank you from the bottom of my heart.

I am genuinely grateful to Dr. Shinichi Nishimura. He supported me in many ways, including setting themes, guiding me on how to proceed my research and how to use the equipment. Also, during the overnight measurement at the synchrotron radiation facility, he taught me the principle of the measurement method, how to use the devices, and analytical methods. I am grateful to him for correcting my incomplete applications, presentations and papers many times and for giving me a lot of valuable advice.

I would like to thank Associate Professor Masashi Okubo, who supported me in research on hydrous ruthenium oxide and in reading society. Because of his guidance during the early stage of my master's course, all the following studies proceeded more efficiently.

I would like to express my thanks to Lecturer Yuki Yamada, who supported me in the work presented in Chapter 4. In addition, he advised me on a lot of things concerning electrolytes in seminars and discussions.

I am sincerely grateful to research collaborators and all Yamada-Okubo laboratory members for kind help and supports. Moreover I acknowledges financial support from "Materials Education Program for the Future Leaders in Research, Industry, and Technology" (MERIT) project and thank Professor Masashi Kawasaki, who is my assistant supervisor in the program. He had a discussion with me about the research once every three months and provided useful suggestions from a physics perspective.

Finally, I am deeply thankful to the seven committee members (Professor Atsuo Yamada, Professor Suguru Noda, Professor Akira Nakayama, Associate Professor Masashi Okubo, Associate Professor Ryuji Kikuchi, Associate Professor Toru Wakihara, Lecturer Yuki Yamada) for this thesis. Their helpful and valuable comments on my research and defense, greatly improved the research results.